universität wien

# DISSERTATION

Titel der Dissertation

"Investigation of Deformation Induced Changes of the Microstructure of Semicrystalline Polymers and their Impact on Mechanical Properties"

angestrebter akademischer Grad

Doktor der Naturwissenschaften (Dr.rer.nat)


| | |
|---|---|
| Verfasser: | Mag. Florian Spieckermann |
| Matrikelnummer: | 9926828 |
| Dissertationsgebiet (lt. Studienblatt): | Physik |
| Betreuer: | Ao. Univ.-Prof. Dr. Michael Zehetbauer |


Wien, am 28. November 2010

# Abstract

*The present project comprises results of the investigation of the influence of mechanical deformation on the macroscopic physical properties in semicrystalline polymers. One focus is the investigation of the micromechanical processes responsible for the yielding behaviour of semicrystalline polymers. In this context it is of special interest whether the presence of dislocations and their interactions govern the part of the strengthening which arises from the crystalline phase. A direct proof of dislocations in the bulk material is now possible with a recent improvement of Multi Reflection X-ray Bragg Profile analysis (MXPA). By application of this method new results on the kinetics and multiplication of dislocations in the investigated materials are presented. The second focus of the work is concerned with the adaptation of the MXPA method for polymeric materials. In particular, this concerns the numerical calculation of the dislocation contrast for the alpha-phase of isotactic polypropylene and the resulting possibility to identify specific dislocation types using MXPA.*

# Kurzfassung

*Die vorliegende Arbeit präsentiert Ergebnisse der Untersuchung des Einflusses der mechanischen Verformung auf makroskopische physikalische Eigenschaften in teilkristallinen Polymeren. Einen Schwerpunkt bildet die Untersuchung der mikromechanischen Prozesse, die für das Fließverhalten von teilkristallinen Polymeren verantwortlich sind. Von besonderem Interesse ist, ob die Existenz von Versetzungen und ihre Wechselwirkungen den kristallinen Beitrag zur Festigkeit und zur Verfestigung beeinflusst. Ein direkter Nachweis von Versetzungen im Massivmaterial ist jetzt mittels Multi Reflection X-ray-Bragg-Profil-Analyse (MXPA) möglich. Durch die Anwendung dieser Methode werden neue Erkenntnisse über die Kinetik und Vervielfachung von Versetzungen in teilkristallinen Polymeren gewonnen. Ein weiterer Schwerpunkt der Arbeit sind die Untersuchungen bezüglich der Adaptierung der MXPA Methode für Polymere. Insbesondere betrifft dies die numerische Berechnung des Versetzungskontrasts für die alpha-Phase von isotaktischem Polypropylen und die damit mögliche Identifikation spezifischer Versetzungstypen mittels MXPA.*

# Contents

# Preamble

*This preamble reproduces a general audience (but peer-reviewed) article [S1] to be published at* Atomium Culture*, describing the main motivation for this thesis in comprehensive manner. Atomium Culture is a newly installed platform of the European Union for the selection, exchange and dissemination of the most innovative European research, to increase the movement of knowledge across borders, across sectors and to the public at large [1].*

## "Nano"-effects in Your Coffee Maker [S1]

You may have noticed that over a number of years, plastics have been replacing metals in objects of everyday life. It could be your coffee machine, electric kettle, or the wireless. Indeed, the volume of plastics processed worldwide surpassed that of metals about ten years ago. The large proportion of metals in automotive and aircraft engineering that have been replaced by polymers has led to considerable savings in fuel consumption simply by making cars and planes lighter. This development is the fruit of enormous advances in polymer science. Many materials were made resistant to ultraviolet (UV) radiation or environmental chemicals. Introduction of carbon or glass fibres made the polymers mechanically stronger.

Despite these undoubtedly major advances in the last 20–30 years, the deformation of plastics at the microscopic level in one class of plastics, the semicrystalline polymers, is yet to be fully understood. Semicrystalline polymers consist of a crystalline part and an amorphous or glassy part. The most important plastics in terms of application, such as polyethylene (PE), polypropylene (PP), and nylon (PA), fall into this category. Since the crystalline phase is usually much harder than the amorphous one, it greatly influences the strength of the material. Interestingly, however, it is not so much the relative volumes of the two different phases as the thickness of the crystalline area that is crucial. During crystallisation from the melt, the so-called lamellae, extremely thin platelets with only a few nanometres (a few billionth of a metre) thickness, are formed. A plausible explanation for this behaviour may lie in the existence of small irregularities in the structure of the crystalline lattice of the lamellae and in their ability to move. Among such lattice defects, linear defects, the dislocations, are the main carriers of plastic deformation in many crystalline materials and thus play a crucial role in their strength: in semicrystalline polymers, however, their role is controversial so far.

It was the research group on nanostructured materials of the physics faculty at the Univer-

sity of Vienna that, for the first time, proved the existence of dislocations in melt crystallised polypropylene, which is the state in which the material is usually shipped by the manufacturer. The group used X-ray diffraction, to measure the characteristic lattice distortion, a sort of fingerprint of a particular dislocation. Subsequently, the group could not only count the number of dislocations but also correlate that number with the mechanical properties. It appears that in metals with grain sizes, i.e. crystal sizes, in the nanometer range, as well as in semicrystalline polymers, the smaller the crystals, the weaker the material. There are some indications that similar deformation mechanisms are active despite large differences in the structure and the bonding. In the case of both, metals and polymers, the scientific community is divided about the precise role of dislocations in the properties of these smallest crystallites, and fundamental understanding of the nanostructure of metals and of polymers will prove mutually supportive.

Even basic research needs to consider possible applications although they may not be obvious at first sight. In the present case, however, this question can be easily answered: if it is possible to manipulate the number, arrangement and mobility of dislocations in semicrystalline polymers – and some promising approaches have been reported in international literature – they can be made far stronger and ductile (that is, they could be drawn into extremely fine strands), thereby opening completely new fields of application of plastics just as resistance to UV did several decades ago.

# 1. Aim of this Work

The complexity of the microstructure of semicrystalline polymers causes the controversial views on the role of dislocations in the crystalline phase of semicrystalline polymers. In 1978 the Nobel laureate Paul Flory had reservations with respect to the ability of dislocations to move in the existing molecular arrangements and concluded in *Nature* [2] that the only possibility for plastic deformation in semicrystalline polymers had to occur by adiabatic melting i.e. the destruction of the crystalline areas. This work highly influenced the work of a large number of following polymer physicists and chemists. Research concerned with dislocations in polymers was not carried out for almost a decade based on these considerations but also because of lacking experimental tools to prove their existence and to study their kinetics. The dislocation based concepts were reactivated in the early nineteen nineties with the application of crystal plasticity models and their experimental validation by texture analysis.

In the pioneering work of Wilhelm and Paris et al. [3, 4] it was demonstrated that the quantification of dislocations is possible in bulk semicrystalline polypropylene by means of a method evaluating, i.e. the X-ray line broadening the so called Multireflection X-ray Line Profile Analysis (MXPA). Most importantly it was shown that a strong change in the number of dislocations was induced by plastic deformation.

The present work is motivated by this first approach and presents further developments in the quantitative analysis of dislocation analysis in semicrystalline polymers in experimental and theoretical terms. The MXPA results are correlated with experimental data gained from mechanical, thermal analysis and microscopy experiments in order to investigate the micromechanical processes responsible for the yielding behaviour of semicrystalline polymers in general.

To reach this goal the present thesis is divided into five parts. Part I gives a brief introduction to the mechanics of semicrystalline polymers and to X-ray line profile analysis. In Part II the central results of this thesis are presented in the form of three papers published in international peer reviewed journals. The following part extends the presented results by the unpublished experimental data and a chapter concerned with numerical calculations of the characteristic contrast of dislocations in isotactic polypropylene. In Part IV the results are recapitulated and the consequences for the future research are discussed. At last the Appendix (part V) is added which comprises the programme-code used for the numerical calculations of Part III.

# Part I.

# Theoretical Background

In the first chapter of this theoretical overview a brief introduction into the state of the art of the mechanics and the microstructural aspects of semicrystalline polymers is given including a focus on the role of dislocations. The second chapter will present an introduction into X-ray line profile analysis (XPA) as the tool of choice to characterise the dislocation densities and dynamics.

# 2. Semicrystalline Polymers

In most cases crystalline polymers can be found in the form of lamellar crystallites separated by amorphous layers, although under special conditions small single crystals can be produced [5, 6]. This specific structural arrangement is caused by the low probability of disentanglement of the intertwined macromolecular chains when it is crystallising from the melt.

Thicknesses of the crystalline lamellae in the range of 5 to 100 nm have been observed using different experimental techniques. These include electron microscopy but also diffraction methods such as small and wide angle X-ray scattering (SAXS, WAXS) and differential scanning calorimetry (DSC).

The most common picture of the crystalline lamellae suggests that they consist of folded chains of the constituting macromolecules. Depending on the supercooling regimes of the crystallisation a certain extent of disorder occurs in the crystallites. The lamellae usually grow radially from a nucleation site forming so called spherulites. New lamellae have to grow to fill the volume when the distance from the spherulite centre gets bigger. The lamellae in the spherulites are arranged in stacks of three to four lamellae with similar orientation. Therefore the new lamellae are either incorporated in existing stacks or start to form new stacks while amorphous material is filling the remaining misfits [6, 7]. The growth of the lamellae is usually only stopped when a spherulite is touching the nearest neighbouring one which leads to the formation of straight interfaces and the polygonal shape of the spherulites (Figure 2.1).

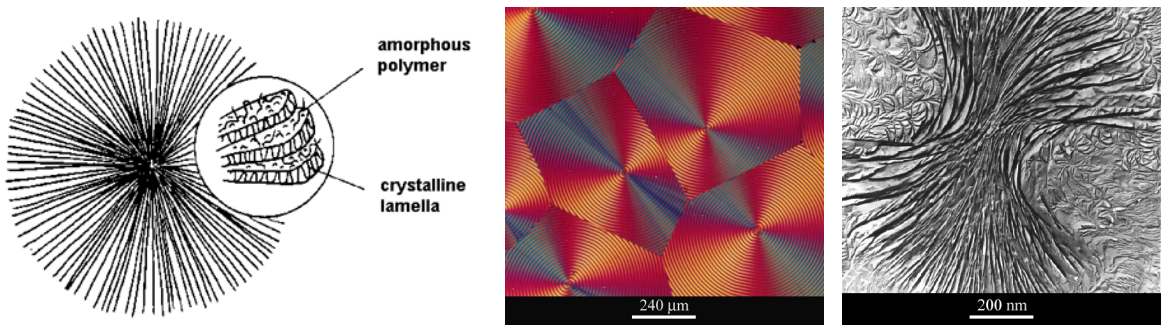


**Figure 2.1.:** (a) Schematic representation of the arrangement of the crystalline lamellae in the spherulitic superstructure, (b) optical polarisation micrograph of polyhydroxybutyrate and (c) sheaf-like arrangement of lamellae representative of the initial stages in spherulite formation (transmission electron micrograph of polyethylene) [8].

## 2.1. Elasticity and Plasticity

As the mechanical properties of the crystalline and the amorphous phase differ considerably, a complete understanding of the mechanical properties can only be gained when the phase specific mechanisms are as well conceived as the mechanisms caused by their interaction. This implies the effect of the size of the structures which differ considerably for the different phases.

Both the mechanical behaviour of amorphous and semicrystalline polymers were subject of a number of investigations in the last decades [9]. The studies resulted in elaborate models to describe the elasticity, the yielding, and the hardening or softening of the polymer.

### 2.1.1. The Stress-Strain Characteristics of Semicrystalline Polymers

The mechanical behaviour of a physical material is best described by the stress-strain curve as obtained from mechanical uniaxial deformation experiments. Hiss et al. [10] found that the typical stress strain curve of polyethylene can be separated into four characteristic regions by the use of cyclic loading unloading experiments related to the four transition points A, B, C and D as illustrated in Figure 2.2. The cyclic loading and unloading permits to identify the recoverable and the residual parts of the deformations thus allowing to relate these observations to the influence of the macromolecular network (see Chapter 5 for a detailed description). Combining such experiments with microstructural observations the transition points could be related to the following microstructural processes [10, 11]:

**Point A** End of purely elastic deformation – plastic slip starts. This point is characteristic for polyethylene where two distinct yield points occur while in most other polymers the transition from point A to B is smooth. The deformation before this point is mainly governed by the amorphous phase. Crystallographic slip occurs after a reorientation of the lamellae, which causes the activation of few slip systems lying in favourable orientations.

**Point B** Begin of massive slip, this corresponds to the yield point. Almost ideal plastic flow or even softening is observed.

**Point C** Backstresses from the entangled network cause a limited destruction of lamellae and thus a small reduction in crystallinity. A strong strain hardening accompanies the following part of the stress strain curve.

**Point D** is characterised by the formation of micro-fibrils at very high strains and disentanglement of the chains leading to unrecoverable deformation.

Each of the sections of the deformation curve (stress-strain curve) is related to microstructural processes in the amorphous and the crystalline phase of the semicrystalline material. The following sections give a review of the crystallographic and molecular processes involved in the elastic and plastic deformation as well as in the strain hardening, and of their mathematical modelling.

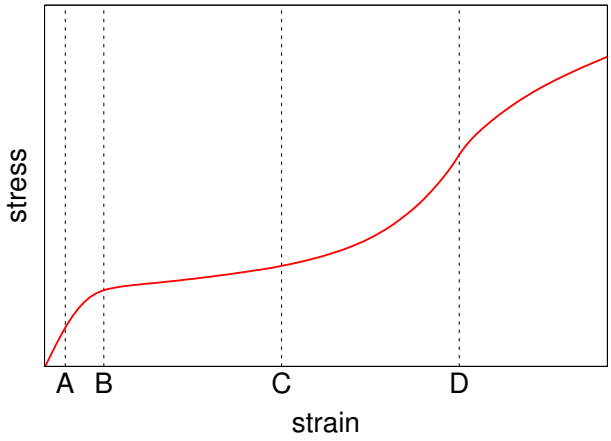


**Figure 2.2.:** Transition points of the stress strain curve of a semicrystalline polymer

### 2.1.2. Some Considerations on Elasticity and Rubber Elasticity

When a prismatic piece of matter with length $l$ is deformed by the length $\Delta l$ under isothermal conditions one can write the force $f$ necessary for the deformation as the derivative of the Helmholtz free energy $F$ which is a function of the extension ratio $\lambda = (l + \Delta l)/l$

$$f = \frac{1}{l}\left(\frac{\partial F}{\partial \lambda}\right)_{V,T}. \tag{2.1}$$

Substituting $F$ in equation 2.1 by $F = U - TS$ one obtains two terms for the force, an energetic and an entropic contribution [7]

$$f = \frac{1}{l}\left(\frac{\partial U}{\partial \lambda}\right)_{V,T} - \frac{T}{l}\left(\frac{\partial S}{\partial \lambda}\right)_{V,T} \tag{2.2}$$

$$= f_U + f_S. \tag{2.3}$$

The concept of the ideal rubber is a material where the energetic part is set

$$f_U = 0 \tag{2.4}$$

as opposed to the ideal crystal where the entropic part is set $f_S = 0$.

The structure of rubbery or elastomeric materials consists of a macromolecular network structure with sparse cross linking by chemical bonds. But also macromolecular entanglements can result in a rubbery behaviour. The nature of the stress strain behaviour is governed, as equation 2.3 suggests, by changes in the configurational entropy and can therefore be modelled using statistical mechanics or invariant based continuum mechanics theories. A review of several approaches was given by Boyce and Arruda [12]. A detailed development of the approaches from

statistical mechanics can be found in the books of Treloar [13] and Strobl [7] and in the diploma thesis of the author [14]. At this point we will therefore only discuss some principles based on Gaussian and inverse Langevin statistics and a relatively new model proposed by Gent [15] that allows considerable simplification of the numerical treatment of the problem and at the same time provides physically significant model parameters especially for the case of entangled networks.

As a good starting point one can assume a randomly oriented long-molecular chain structure with $n$ links per chain and a segment length of $l_0$ between the links. Using Gaussian statistics [12, 7, 13] the probability distribution function $P(r)$ end-to-end distance $r$ is given by

$$P(r) = 4\pi \left(\frac{3}{2\pi n l_0^2}\right)^{\frac{2}{3}} r^2 \exp\left(-\frac{3r^2}{2nl_0^2}\right). \tag{2.5}$$

Hence the average length of a chain in equilibrium $L_0$, i.e. before deformation, is given by the root mean square of $r$

$$L_0 = \sqrt{\langle r^2 \rangle} = \sqrt{nl_0^2} = \sqrt{n} l_0. \tag{2.6}$$

The energy related to a 3 dimensional stretch $(\lambda_1, \lambda_2, \lambda_3)$ is related to a change in the configurational entropy. It is determined as [12]

$$W_{Gauss} = F_{Gauss} = \frac{1}{2} NkT \left(\lambda_1^2 + \lambda_2^2 + \lambda_3^2 - 3\right) \tag{2.7}$$

with $k$ being Boltzmann's constant and $N$ the number of involved chains[1]. In terms of the first strain invariant

$$I_1 = \lambda_1^2 + \lambda_2^2 + \lambda_3^2 \tag{2.8}$$

this can be rewritten as

$$W_{Gauss} = F_{Gauss} = \frac{1}{2} NkT \left(I_1 - 3\right). \tag{2.9}$$

The *true* stress ($\sigma_{33}$) – stretch ($\lambda$) relationship for the Gaussian model in uniaxial deformation ($\lambda = \lambda_3$, $\lambda_1 = \lambda_2$) under assumption of a constant volume V (thus the third invariant $I_3 = \lambda_1\lambda_2\lambda_3 = 1$) can now be determined from the strain energy with equation 2.1 and is found as

$$\sigma_{Gauss} = \frac{NkT}{V} \left(\lambda^2 - \frac{1}{\lambda}\right). \tag{2.10}$$

This formula relies on the assumption that the applied stretch is significantly smaller than the

[1] This is the entropic contribution to $F = U - TS$ as U is considered to be 0.

length of the stretched chains. When this assumption is not met the Gaussian treatment has to be replaced by a formula based on inverse Langevin statistics [12, 9, 16]. The relative stretch of the chains $r/nl_0$ is then given by a Langevin function $\mathcal{L}(\beta)$

$$\frac{r}{nl_0} = \mathcal{L}(\beta) = \coth\beta - \frac{1}{\beta} \tag{2.11}$$

With the inverse Langevin function

$$\mathcal{L}^{-1}\left(\frac{r}{nl}\right) = \beta \tag{2.12}$$

the (nominal) stress stretch relationship results to [13]

$$\sigma_{Kuhn} = \frac{NkT}{3}\sqrt{n}\left\{\mathcal{L}^{-1}\left(\frac{\lambda}{\sqrt{n}}\right) - \lambda^{-\frac{3}{2}} \cdot \mathcal{L}^{-1}\left(\frac{1}{\lambda^{1/2}\sqrt{n}}\right)\right\}. \tag{2.13}$$

Since the inverse Langevin formula is rather difficult to treat numerically it is reasonable to use the Padé approximation derived by Cohen [17]

$$\mathcal{L}^{-1}(\beta) = \beta\frac{3-\beta^2}{1-\beta^2} + O(\beta^6). \tag{2.14}$$

A rather different approach was chosen in the case of the model by Gent [15]. In order to treat the limited extensibility, a maximum value $I_m$ for the first invariant of the stretch $I_1$ is introduced. In the case of the molecular chain network this means the fully stretched state. This is simulated by the equation

$$W = -\frac{E}{6}J_m \ln\left(1 - \frac{I_1 - 3}{J_m}\right) \tag{2.15}$$

for the stretch energy. The true stress in uniaxial deformation is then given by

$$\sigma_{Gent} = \frac{E}{3}\frac{(\lambda^2 - \lambda^{-1})}{[1 - (I_1 - 3)/J_m]}. \tag{2.16}$$

As $E = 3NkT/V$ is the so-called rubber modulus, this term is equivalent to equation 2.10 apart from the denominator. Although it has only two parameters this simple equation is not only able to mimic the behaviour of models involving the inverse Langevin statistics [15] but also more complex 3-dimensional approaches as the 3-, 4- or 8-chain model [12]. Horgan and Saccomandi [18] demonstrated that the parameter $J_m$, the maximum value of $(I_1 - 3)$, is related to the number of rigid links of a single chain $n$ by

$$J_m = 3\,(n-1)\,. \tag{2.17}$$

The model is therefore related to the physical parameters $E$ and $n$ known from the statistical macromolecular models and is still easy to handle numerically.

### 2.1.3. Plasticity of the Amorphous Phase

As discussed in the last section, the macromolecular character of the polymer chains and in particular their limited extensibility governs the hardening characteristics as a function of the applied strain or stretch. On the other hand, viscous deformation involving a change of the molecular centre of mass requires mobilisation of chain segments. In contrast to the deformation mechanism discussed in section 2.1.2 this deformation is not recovered unless an external force is applied and can therefore be considered plastic rather than elastic. In a real polymeric material it is difficult to distinguish between these two processes as the backstresses from the molecular network involve relaxation effects on different time scales.

Experimental observations in amorphous polymeric materials indicate that a number of thermally activated processes are responsible for the magnitude of the yield stress as a function of the temperature and the strain rate. A description of this behaviour is possible by assuming a number of Eyring processes [19, 20, 21], each of them corresponding to a molecular mechanism. In this picture each mechanism can be considered as the ability of a polymer chain segments to overcome an energy barrier at the yield point [21]. It was also found that with only two thermally activated mechanisms the experimental results could be described [20]. Some authors attempted to relate the processes to transitions observed in dynamical mechanical measurements [20, 22], as the glass transition for instance. The state of the art of the complex modelling has been discussed by Richeton [22, 23]. A complete modelling framework for the viscous flow of amorphous polymers has been proposed based on the cooperative model of Fotheringham and Cherry [24] who assume a number $n$ of cooperative chain segment jumps resulting in only one term in the constitutive equation instead of one for each assumed Eyring process.

### 2.1.4. Plastictiy of the Crystalline Phase

The mechanisms described in the last section (sec. 2.1.3) mainly deal with the plasticity of the amorphous phase. Although the deformation of the crystalline phase of semicrystalline polymers is also governed by thermally activated processes [25, 26, 27, 28] some fundamental differences exist. Due to the crystallographic character of the material several, mainly orientation dependent mechanisms of crystal plasticity have been observed.

#### Mechanisms of Crystal Plasticity

The main mechanism of plastic deformation in semicrystalline polymers has been identified to be crystallographic slip [5, 6, 29]. This mechanism allows for relatively large deformations as compared to all other mechanisms. This is related to the fact that entanglements are pushed to the amorphous regions when crystallising from the melt.

The combination of the crystallographic plane $(hkl)$ in which slip occurs, and a slip direction $[uvw]$ form the slip system. Single slip is a pure shear deformation. Therefore, in order to achieve

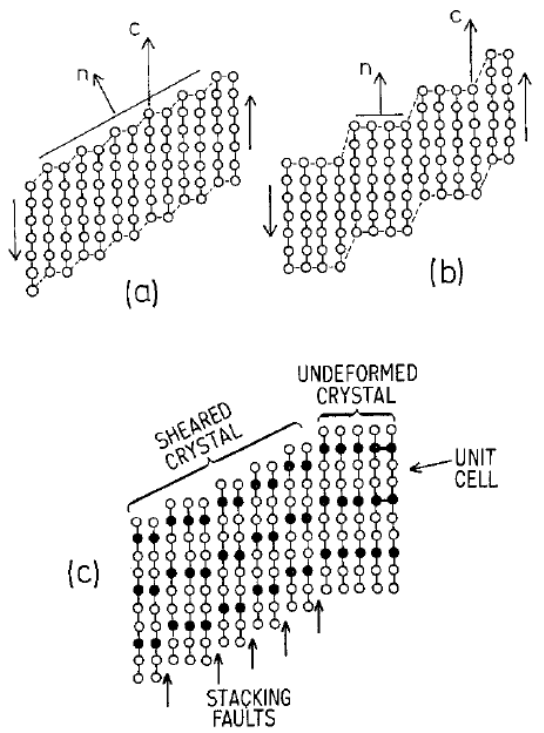


**Figure 2.3.:** Schematic representation of the fineness of slip. (a) Fine slip. The shearing by one lattice vector on every second lattice plane has caused a rotation of the lamella surface normal with respect to the crystal orientation. (b) Coarse slip. The total shear is the same as for fine slip but it is localised in a few lattice planes. The lamella normal **n** does not rotate. (c) Fine slip of partial dislocations [30].

homogeneous deformation, more slip systems are necessary, the minimum number of independent slip systems being five [31]. In polymers the number of possible independent slip systems is generally lower, four in the case of polyethylene and only three in the case of polypropylene. Still due to the soft amorphous phase the lamellae can rearrange upon deformation in a manner to compensate for the low number of slip systems and allow for a homogeneous deformation.

Two distinct mechanisms of crystallographic slip have been observed. Chain slip occurs in the direction of the polymer chains and transverse slip in the perpendicular direction [5, 6, 29]. For both of these mechanisms the slip planes lie parallel to the polymer chains. The critical resolved shear stress (CRSS), i.e. the resolved stress in the slip plane necessary to activate a slip system, is generally lower for the closely packed slip planes (Figure 2.4).

On the one hand slip can occur in a more cooperative manner, meaning that a high number of close parallel planes is activated. This fine slip causes the rotation of the crystallographic axis with respect to the lamella surface normal [5]. On the other hand localised slip confined to few slip planes, the coarse slip, does not involve a relative tilt of the crystallographic axis with respect to the lamella surface. Schemes of both mechanisms, fine and coarse slip, are sketched in Fig. 2.3. The orientation of the lamella surfaces can be well determined by SAXS experiments

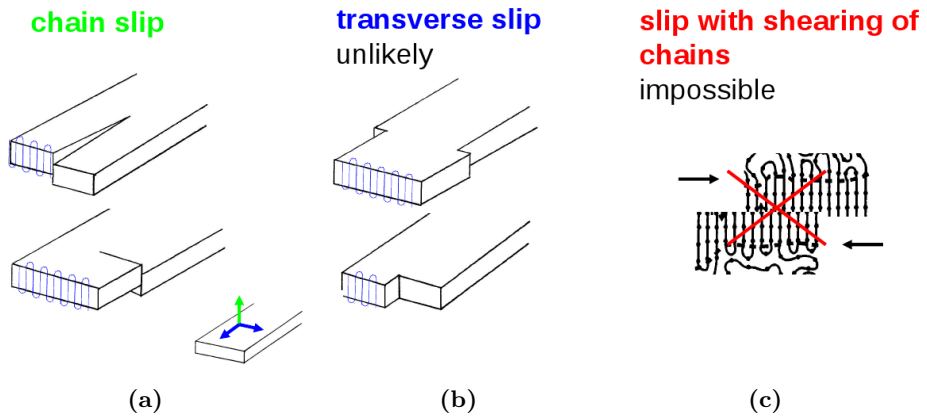


**Figure 2.4.:** Schematic representation of chain (a) and transverse slip (b). Slip in planes orthogonal to the chain direction is prevented by the strong covalent bonds in the macromolecular backbones (c).

whereas the crystallographic orientation can be measured by WAXS texture measurements. Such experiments showed that only fine slip occurs at small deformations [32, 33]. It was also revealed that earlier observations of coarse slip [34] were related to micro-necking caused by cavitation. Cavitation could be ascribed to deformation modes with positive normal stress components as tensile deformation for instance. Thus fine slip is the prevalent mechanism related to crystallographic slip [6]. Cavitation on the other hand is at the origin of crazing and localised shear primarily localised in the amorphous phase . For the better understanding it is noted that crazes differ from micro cracks in their ability to absorb fracture energy and therefore even increase ductility and fracture toughness. In addition to the predominant crystallographic slip also martensitic transformation and twinning have been observed to a very low extent [5].

## 2.2. The Role of Crystalline Defects in Semicrystalline Polymers

The yielding in the crystalline phase and therefore in the semicrystalline material as a whole is, as discussed in the last section, controlled by the initiation of crystallographic slip. The mechanisms involved have been matter of discussion in the last decades, and two distinct schools developed.

The first approach developed by Flory and Yoon [2] is founded in the tradition of macromolecular thermodynamics. It is suggested that due to the high degree of interconnection between the crystalline lamellae, the plastic deformation of semicrystalline polymers consists of a process of localised melting and recrystallisation under adiabatic conditions. Many other models follow this type of interpretation [35, 27], by assuming mobilisation of chain segments in the crystalline regions with localised melting as the inherent thermally activated process.

The second approach is based on the theory of crystal plasticity as it is often applied for metallic materials - i.e. plastic deformation of polymer crystals is governed by dislocation generation and motion [36].

Evidence for the importance of dislocations is given by several papers: (1) that of Bartczak [33]

who experimentally determined the critical resolved shear stress (crss) in HDPE single crystals and found good agreement with theoretical values for the Peierls stress [37] of dislocations in the corresponding slip systems; (2) that of Brown [38] who could uniquely associate the characteristics of strain jumps at small deformations in polyethylene to dislocations. Recently Bartczak et al. [39, 40] introduced (hydrogenated oligio(cyclopentadiene)) molecules in the crystalline phase of isotactic polypropylene (iPP) and could explain the specific raise of yield stress by impediment of dislocation motion. Already some years ago a dislocation generation model was suggested by Young [36] and developed by other authors [41, 42]. It could predict a characteristic dependence of the yield stress on the crystal thickness, which was confirmed already in 1993 by experiments of Darras et al. [43] in polyethylene (PE). The model was extended in 2005 by Argon et al. [26] by adding the influence of temperature and a Frank-Read mechanism for larger lamella (and thus crystal-) sizes where saturation of strength occurs which has been also observed experimentally by Kazmierczak et al. [32].

A somewhat different but still dislocation-based concept has been recently published by Manewich et al. [44] and Nikolov and Raabe [45] which builds on nucleation and propagation of [001] screw dislocations due to migration of soliton-like 180° chain twist defects. By taking into account a surface interaction effect it was possible to correctly describe the whole lamella thickness dependence of the yield stress.

## 2.3. Generation of Dislocations in Semicrystalline Polymers

### 2.3.1. Theory of Dislocations

When matter crystallises this leads to periodic structures with a certain degree of disorder. These deviations of the ideal crystal are often entitled as lattice *defects* or (some consider it more appropriate) lattice *imperfections*. Related to their spacial geometry they can be subdivided into point, line, surface, and volume defects [46]. All of these defects can considerably affect the physical properties of the crystalline material. Point defects include vacancies or interstitials as well as impurities, which can be of substitutional or interstitial nature. Line defects are above all dislocations but can also occur at triple junctions of planar defects. The planar defects include stacking faults, grain and twin boundaries. Volumetric defects include precipitates, voids, bubbles and others.

As explained in section 2.2 there is overwhelming evidence accumulated over several decades that the crystalline lamellae of a number of semicrystalline polymers including PE, PA , iPP deform plastically by generation and motion of dislocations.

For non polymeric materials several origins of dislocations have been identified. As stated above every freshly grown crystal will contain imperfections and thus also dislocations are observed. If the nucleation of a dislocation occurs in a dislocation free region the process is referred to as homogeneous. This only happens under extreme conditions because a relatively high stress is required. For nanometer size single-crystals these extreme conditions can be met more easily as the activation energy is small enough to be provided thermally already at low temperatures

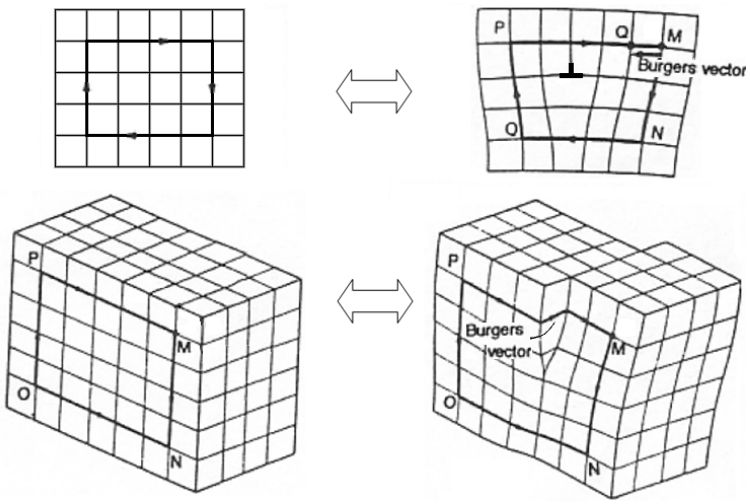


**Figure 2.5.:** Schematic representations of the formation of edge and screw dislocations and the resultant Burgers vector [46].

[26]. On the other hand the generation of dislocations by (e.g. Frank-Read) sources, multiple cross glide and climb have been observed and studied. Grain boundaries have also been found to emit dislocations.

In the simplest cases one can distinguish between two types of dislocations. If one visualises a partial cut of the crystal along a crystallographic axis, the introduction of additional atomic half layers in the crystal would form an edge dislocation ($\perp$).

For the second type, the screw dislocations ($\odot$), the two half planes of the cut are sheared with respect to each other by a multiple of the lattice vector. The path on the crystal planes around the linear defect hence formed follows a helix, while for the edge case it returns to its origin.

The Burgers vector $\mathbf{B}$ describes the amount and direction of the relative displacement of the crystal parts. For screw dislocations it is parallel to the dislocation line (characterised by the line element $\mathbf{S}$) while it is perpendicular to $\mathbf{S}$ for edge dislocations (Figure 2.5).

The elastic distortions introduced in the crystal differ for screw and edge dislocations. Screw dislocations only have a shear stress component $\tau_{\Theta z}$ in a radial plane $\Theta$ in axial direction $z$ as the only stress component. Using Hook's law for the shear stress this can be represented as

$$\tau_{\Theta z} = \mu\gamma_{\Theta z} = \frac{\mu B}{2\pi r} \tag{2.18}$$

with the shear modulus $\mu$, the shear strain $\gamma$, the radial distance from the core $r$ and the magnitude of the Burgers vector B [47]. This results in the stress tensor $\sigma^{\odot}_{r\Theta z}$for screw dislocations

in cylindrical coordinates

$$\sigma^{\odot}_{r\Theta z} = \begin{bmatrix} 0 & 0 & 0 \\ 0 & 0 & \tau_{\Theta z} \\ 0 & \tau_{\Theta z} & 0 \end{bmatrix}. \tag{2.19}$$

In Cartesian coordinates this relation would read as

$$\sigma^{\odot}_{xyz} = \begin{bmatrix} 0 & 0 & \tau_{xz} \\ 0 & 0 & \tau_{yz} \\ \tau_{xz} & \tau_{yz} & 0 \end{bmatrix}. \tag{2.20}$$

The stress field of the edge dislocations is much more complex because, in addition to the shear stress components, it also contains normal stress components. The stress tensor in Cartesian coordinates $\sigma^{\perp}_{xyz}$ has the form

$$\sigma^{\perp}_{xyz} = \begin{bmatrix} \sigma_{xx} & \tau_{xy} & 0 \\ \tau_{xy} & \sigma_{yy} & 0 \\ 0 & 0 & \sigma_{zz} \end{bmatrix}. \tag{2.21}$$

The components of this tensor have the following form

$$\sigma_{xx} = -\frac{\mu B}{2\pi(1-\nu)} \frac{y(3x^2+y^2)}{(x^2+y^2)^2} = -\frac{\mu B}{2\pi(1-\nu)} \frac{\sin\theta(2+\cos(2\theta))}{r} \tag{2.22a}$$

$$\sigma_{yy} = \frac{\mu B}{2\pi(1-\nu)} \frac{y(x^2-y^2)}{(x^2+y^2)^2} = \frac{\mu B}{2\pi(1-\nu)} \frac{\sin\theta\cos(2\theta)}{r} \tag{2.22b}$$

$$\sigma_{zz} = \nu\left(\sigma_{xx} + \sigma_{yy}\right) \tag{2.22c}$$

$$\tau_{xy} = \frac{\mu B}{2\pi(1-\nu)} \frac{x(x^2-y^2)}{(x^2+y^2)^2} = \frac{\mu B}{2\pi(1-\nu)} \frac{\cos\theta\cos(2\theta)}{r} \tag{2.22d}$$

The occurrence of the Poisson ratio $\nu$ shows that in contrast to the screw dislocation an edge dislocation causes a change in the crystalline volume.

The displacements related to the distortions can be calculated for anisotropic crystals by application of the Stroh formalism [48]. As this question is crucial for the interpretation of anisotropy related effects in X-ray diffraction patterns it will be discussed in detail in Chapter 9.1 related to the calculation of the dislocation contrast factor.

From the elastic stress state we can calculate the elastic energy associated with a dislocation. It is equal to the energy necessary to create a dislocation [46, 47]. This is done by introducing a displacement with the magnitude $\xi$. At a distance $x$ from the dislocation core the stress field on the glide plane ($\Theta = 0$) is given with equation 2.22d as

$$\tau_{xy}(x) = \frac{\mu\xi}{2\pi(1-\nu)} \frac{1}{x}. \tag{2.23}$$

From the force acting on a surface element $L \cdot \mathrm{d}x$

$$f_x(\xi) = \tau_{xy} \cdot L \cdot \mathrm{d}x \tag{2.24}$$

we can calculate the elastic energy necessary for the displacement with the magnitude of the Burgers vector $\xi = B$.

$$E_{el} = \int_{r_0}^{R_0} \left( \int_0^B f_x(\xi) \mathrm{d}\xi \right) \mathrm{d}x = L \frac{\mu B^2}{4\pi(1-\nu)} \int_{r_0}^{R_0} \frac{\mathrm{d}x}{x} = L \frac{\mu B^2}{4\pi(1-\nu)} \ln \frac{R_0}{r_0}. \tag{2.25}$$

By integrating from the dislocation core size $r_0$ to the crystal size $R_0$ we excluded the dislocation core where Hook's law is not applicable. The core energy can be calculated from the theoretical shear stress [47] and is approximately

$$E_{core} \approx L \frac{\mu B^2}{4\pi(1-\nu)}. \tag{2.26}$$

The total energy per length unit of an edge dislocation is therefore found as

$$E^{\perp} = \frac{E_{el}}{L} + \frac{E_{core}}{L} = \frac{\mu B^2}{4\pi(1-\nu)} \left( \ln \frac{R_0}{r_0} + 1 \right) \tag{2.27}$$

and correspondingly the line energy of the screw dislocation is found as

$$E^{\odot} = \frac{\mu B^2}{4\pi} \left( \ln \frac{R_0}{r_0} + 1 \right). \tag{2.28}$$

### 2.3.2. The Dislocation Generation Model of Peterson and Young

After deriving the energy to generate dislocations we can start to consider the problem of their formation in semicrystalline polymers. Based on a suggestion of Peterson [49, 37], Young [36] developed a theoretical model for polyethylene assuming the thermally activated generation of dislocations on the lamella surfaces. Due to the limited size of the crystallites a Frank-Read mechanism could be excluded. In the following other authors contributed to this model by calculating dislocation line energies and by experiments [41, 50, 51].

All of these models assumed the homogeneous nucleation of [001] screw dislocations resulting in (hk0) [00l] slip [50] as sketched in Figure 2.6. The energy necessary for the nucleation is provided by the applied mechanical shear stress on the one hand, and by thermal activation on the other hand.

Such a dislocation has a length which is equal to $\lambda$, the lamella thickness[2]. The Burgers vector is considered to have the dimension of a half of the crystallographic c-axis dimension of

[2]Please note the ambiguous nomenclature: $\lambda$ is used for the extension/compression ratio in Section 2.1.2 and in Chapter 5, while in the other sections it is used for the lamella thickness. In chapter 5 the lamella thickness is labelled $l$ for this reason.

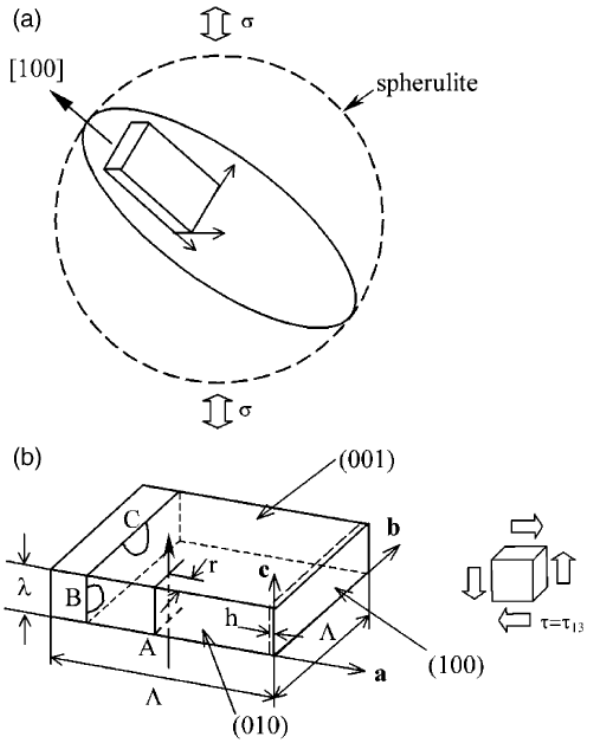


**Figure 2.6.:** Sketch of the formation of dislocations in the crystalline lamellae of polyethylene. (a) depicts a lamella with an arbitrary orientation in a spherulite, (b) principal slip systems of the lamella [26].

the orthorhombic unit cell of PE [51]. The reason for this is that the thermal activation of 180° chain twist defects is at the origin of the dislocation generation. When such a twist defect is formed it results in a c/2 compressive strain [41, 45, 51] leading to a dislocation with Burgers vector

$$B = \frac{c}{2} = 0.127 \text{ nm}. \tag{2.29}$$

The elastic energy of a screw dislocation can be calculated with the results of the last chapter multiplied with its length $\lambda$ and the distance $R_0 = r$ from the nucleation surface according to figure 2.6 (the core energy is neglected[3])

$$E_{el}^{\odot} = \lambda \frac{\mu B^2}{4\pi} \ln\left(\frac{r}{r_0}\right). \tag{2.30}$$

This energy is partly provided by the work $\Delta W$ done by the applied shear stress $\tau$ and partly by the free energy related to the thermal fluctuations $\Delta G$. The work done by the shear stress

[3] Argon et al. discuss a formulation of the problem where the core energy is included by a core cut-off parameter [26].

amounts to

$$\Delta W = \lambda \tau B r \tag{2.31}$$

Therefore $\Delta G$ can be written as

$$\Delta G = E_{el}^{\odot} - \Delta W = \lambda \frac{\mu B^2}{4\pi} \ln\left(\frac{r}{r_0}\right) - \lambda \tau B r. \tag{2.32}$$

The critical value $r_c$ for the distance $r$ is reached when $\Delta G$ has a maximum

$$\left(\frac{\partial \Delta G}{\partial r}\right)_{\tau} = 0 \tag{2.33}$$

and is therefore given by

$$r_c = \frac{\mu B}{4\pi\tau}. \tag{2.34}$$

Knowing $r_c$ we can now rewrite equation 2.32 as critical free energy to form the dislocation

$$\Delta G_c = \lambda \frac{\mu B^2}{4\pi} \ln\left[\left(\frac{r_c}{r_0}\right) - 1\right] = \lambda \frac{\mu B^2}{4\pi} \ln\left(\frac{\mu B}{4\pi\tau r_0} - 1\right). \tag{2.35}$$

We can now set $r_0 = B$ [41, 52] and use equation 2.35 to determine the yield stress

$$\tau_y = \frac{\mu}{4\pi} \exp\left(-\frac{4\pi \Delta G_c}{\lambda \mu B^2} - 1\right). \tag{2.36}$$

From this formula one can directly see that the yield stress depends strongly on the lamella

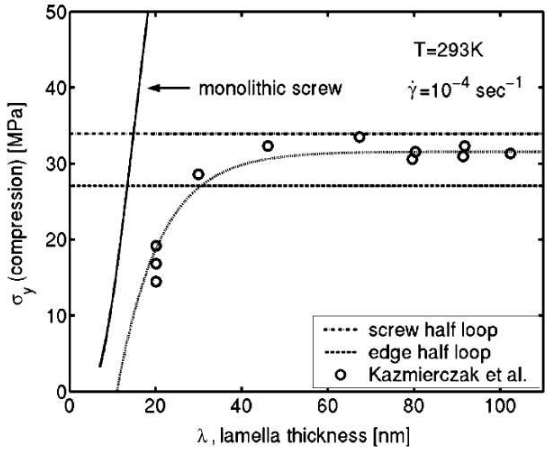


**Figure 2.7.:** Dependence of flow stress of polyethylene measured at 293 K on lamella thickness (open circles), and comparison with dislocation models (straight lines) [26].

thickness $\lambda$. The normal yield stress $\sigma_y$ can be related to the critical (resolved) shear stress $\tau_y$

by multiplication of $\tau_y$ with a Taylor factor $m \approx 3$ [26, 47, 53]. The energy provided by the thermal fluctuations $\Delta G_c$ was found to lie in the order of 40 to $80kT$ [41]. This simple model does indeed well describe the lamella thickness dependence in polyethylene [43] for thicknesses up to 40 nm. Investigations on polypropylene [42] showed very good agreement with the model and a value of $60kT$ was suggested for polypropylene. Already in 1974 Young [36] had shown that for crystals exceeding 40 nm the thermally activation becomes very unlikely and a different process should act and the occurrence of half loop sources at the edges is suggested. Based on the experimental data of Kazcmierczak [32], Argon [26] discussed such a mechanism and found good agreement, as shown in Fig. 2.7, when combining the thermally activated process for small lamellae with the half loop mechanism.

# 3. X-Ray Line Profile Analysis

An important tool for the investigations of dislocations and lamella size is the Multireflection X-ray Line Profile Analysis (MXPA). The reasons for the reliability of this method are as follows.

It is a common feature of X-ray line profiles of crystalline matter that the profiles are not Dirac-delta type but broadened if the (atomic) order is not perfect. The MXPA method considers the characteristics of profile broadening due to various imperfections of the crystalline lattice and due to the finite size, and also allows for their careful separation [54, 55]. Its most advanced versions comprise the characteristics of profile line broadening of several reflection orders and their upper harmonics, and are thus called 'MXPA ... multireflection X-ray Line Profile Analysis'. Different lattice defects with individual microstrain distributions cause a typical diffraction order dependent broadening which allows identifying the nature of these defects [56].

## 3.1. Dislocation Analysis

The physical profile of a Bragg reflection in general can be described by the convolution of the intensity profile related to the limited size of the diffracting crystal and the profile related to lattice distortions. The Fourier transform of this convolution can be written as the Warren and Averbach equation [57, 58]:

$$A(L) = A^S(L)A^D(L) \tag{3.1}$$

where L is the variable of the Fourier transform and $A^S(L)$ and $A^D(L)$ are the size and distortion coefficients respectively. Assuming the mean square strain $\langle \varepsilon_L^2 \rangle$ to be caused by dislocations, Krivoglaz [59] and Wilkens [60, 61] derived the following formulation for the Fourier transform of the profile

$$A(L) = A^S(L)A^D(L) = A^S(L) \exp\left(-2\pi^2 L^2 k^2 \langle \epsilon^2 \rangle\right) \tag{3.2}$$

with

$$\langle \varepsilon_L^2 \rangle = \left(\frac{B}{2\pi}\right)^2 \pi \varrho \; Cf\left(\frac{L}{R_e^*}\right) \tag{3.3}$$

Here $C$ represents the dislocation contrast factor which determines the influence of dislocations to the diffraction profile whereas the values of C depend on the relative orientation of the burgers vector $B$, the line vector $l$ and the diffraction vector $k$ similar to the contrast of dislocations in electron microscopy and the average dislocation density $\varrho$. The Wilkens function $f(L/R_e^*)$, describes the effects of the statistical arrangement of the dislocations on the strain field as a function of the effective outer cut-off radius of dislocations $R_e^*$ [62]. In single crystals the dislocation contrast factor can be determined by the knowledge of the elastic constants of the material, in polycrystals however only an average contrast factor $\overline{C}$ is obtained by averaging over the possible slip systems.

Using this formalism, due to their unique stress field, dislocations can be characterised with a very high reliability. MXPA not only allows for the determination of the local long range internal stresses and the absolute dislocation density but also of the dislocation arrangement [54, 56]. In nanometals, MXPA has been used with great success [63]. Most importantly, applications also include the proof of dislocation presence in arbitrary crystalline materials e.g. molecular crystals like RbC60 fullerenes [64], and above all, bulk semicrystalline polymers as has been shown recently [3, S3]. Today's state-of-the-art version of MXPA is the so called 'multiple whole profile fitting' [55, 62]. Currently it can be used for fcc, hcp and orthorhombic lattices. For $\alpha$-iPP the orthorhombic lattice was used as simplification up to now, as the effect due to the monoclinic angle can be neglected in a first approach. As a next step the monoclinic crystal lattice is to be included in the evaluation. With this improvement of the evaluation procedure not only the absolute dislocation density could be determined but also the specific dislocation types (edge and screw) in the monoclinic lattice [65, 66]. For the orthorhombic lattices found in $\gamma$-iPP, polyhydroxybuthyrate (PHB) and high density polyethylene (HDPE) the evaluation procedure can be applied without adaptations.

Another possible route is the evaluation based on single peak data which has been developed recently [67]. Not only it allows for a crosscheck of the MXPA as single peaks with no overlapping can be evaluated with respect to size and defect induced microstrains (e.g. $(13\bar{1})$ peak of $\alpha$-iPP or (117) peak of $\gamma$-iPP) but this procedure might also open a useful route towards the investigation of polymers with a low number of high intensity reflections (PE for instance). The momentum method developed by Groma [67] is based on the variance method by Wilson [68] and uses the fact that the asymptotic behaviour of the second and fourth order moments exhibit a characteristic behaviour related to the size and the dislocation density. Borbély and Groma demonstrated the applicability of the method to metallic nanomaterials.

## 3.2. Determination of Lamella Size and Size Distribution

The oldest application of XPA is the evaluation of crystallite size (also called 'coherently scattering domain size'), which means the size of a fully defect-free and undistorted crystalline area [69]. The introduction of MXPA allowed a careful separation of the size broadening from that of the strain (dislocation) broadening and thus for a more reliable determination of the lamella size

[54]. Since that time MXPA has been used for the determination of crystallite sizes and their distribution in a huge number of materials [70, 71, 63]. Concerning semicrystalline polymers, it will be shown in chapter 7 for the case of $\alpha$-iPP that the agreement of the size distributions determined by MXPA and by DSC is very good. Also here it could be shown that for the determination of the correct size distribution, dislocations have to be taken into account [S4]. Altogether, this study is a clear proof of the reliability of MXPA method in polymeric materials for both the investigation of dislocations as well as of lamella size.

# Part II.

# Results and Discussion: Publications

In this central part three articles published in international journals are included as published. Chapter 4 gives a condensed overview about the main issues of all three papers and discusses their results in a general context. For full details the reader may proceed to the full articles featured in Chapters 5 to 7. In Chapter 5 the results of cyclic loading-unloading of iPP are presented and discussed with respect to the yielding and hardening behaviour [S2]. Chapter 6 presents surprising results of X-ray line profile analysis experiments in P3HB, which is the first investigation of this kind in this biodegradable material [S3]. Finally, in chapter 7, X-ray line profile analysis was used to determine lamella thickness distributions in iPP [S4]. It is shown that good agreement exists between these measurements and the alternative determination by DSC only if the presence of dislocations is taken into account.

# 4. Overview over the Included Articles

In the present part II, three peer reviewed articles in international publications that comprise results of the work carried out in the context of this present thesis [S2, S3, S4] are reviewed and discussed, and also included in full length (Chapter 5 to 7).

The distinctive morphological features of semicrystalline polymers result in a complex mechanical response and high dependence on the testing conditions. The fact that an amorphous and a crystalline phase are coexisting in the material gives semicrystalline polymers properties similar to composite materials in other areas. The high stiffness of the crystalline phase together with the high temperature and strain-rate sensitivity of the amorphous phase and, most importantly, its network properties are the subject of the article featured in Chapter 5 dealing with *"Determination of Critical Strains in Isotactic Polypropylene by Cyclic Loading - Unloading [S2]"*.

The paper reports an analysis of the phase specific contributions on the deformation curve by means of cyclic loading-unlading experiments, DSC and WAXS. The deformation experiments allow for a separation of the total applied strain into a recoverable and a residual part. This allows for the determination of the critical strains as described in Section 2.1.1. The residual part can again be separated into a part that is recoverable on a longer time scale as suggested in the paper of Hiss et al. [10]. Spieckermann et. al [72] published similar results on $\alpha$ nucleated iPP (Borealis BE50). It was found that in this material the permanent deformation is introduced at a very early stage of the deformation. The deformation recovered by thermal relaxation near the crystallisation temperature not only involves relaxation of the molecular network but also, to a smaller degree however, relaxation processes in the crystalline phase such as annealing of crystalline defects and recrystallisation of oriented amorphous areas (Figure 4.1). The onset of irreversible deformation is highly influenced by the molecular weight and the number of rigid links in the macromolecular network. The part of the deformation recovered immediately after the experiment is mostly related to the overstretching of the amorphous phase and is only to a minor degree governed by relaxation in the crystalline phase.

The experiments carried out in [S2] reveal only small differences in the recovery properties as a function of the deformation temperature, only for the samples deformed below the glass transition temperature a very small effect could be observed. While the stresses of the transition points B and C of the deformation curve are highly affected by the deformation temperature, the critical strains are not changed. These findings underline the generality of the concept of

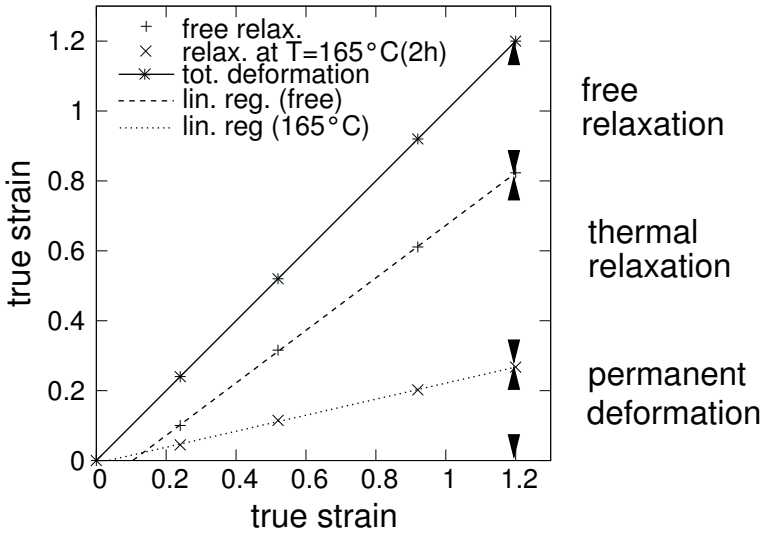


**Figure 4.1.:** Relaxation of $\alpha$ nucleated iPP after thermal treatment. Samples have been deformed at 20°C [72].

the critical strains and that they are governed by the properties of the macromolecular network, which is only to a minor degree affected by the temperature.

On the other hand the hardening behaviour shows a strong dependence of the deformation temperature. This concerns the total strength as well as the softening after the yield point and the finally the rubbery hardening at higher deformations. The paper also reports that in the Haward- Thackray ($(\lambda^2 - 1/\lambda)$ vs. true stress, see Figure 5.7) representation the transition point C also defines a transition from a deformation governed by the crystalline flow towards a hardening mechanism related to the amorphous phase. The point B is followed by a small yield drop for all deformation temperatures. The rubbery hardening after point C, described by the model of Haward and Thackray, also involves a further initiation of slip resulting in a small reduction of the crystallinity while the lamella thickness is not affected. Similar observations have been made by Bartczak et al. [11, 73] in plane strain compression.

The strain energy per cycle indicated a change in the energy consuming processes when passing from temperatures above $T_g$ to a temperature below $T_g$. While the low temperature deformation exhibits a saturating energy per cycle, those of the higher deformation temperatures increase monotonically. The higher stiffness of the glassy amorphous phase below $T_g$ might hinder the increase of energy consuming processes.

The fact that the elastic modulus decreases almost monotonically as a function of the cycle number suggests a deformation mechanism without drastic destruction of the lamellar integrity. This is in accordance with the observations concerning the evolution of the lamellar thickness and the crystallinity.

In poly(3-hydroxybuthyrate) (P3HB) a completely different picture has to be drawn. Chapter 6 with the title *"Plasticity and X-ray Line Profile Analysis of the Semicrystalline Polymer Poly(3-hydroxybutyrate) [S3]"* reports on in-situ WAXS investigations during uniaxial compres-

sion. Multi-reflection X-ray analysis (MXPA) was applied to the recorded diffraction profiles in order to evaluate the evolution of the microstructure as a function of the plastic deformation. This includes the thickness of the crystalline lamellae, and the dislocation density. By a phase separation procedure applied to the WAXS patterns was possible to follow the evolution of the crystallinity as a function of the deformation.

Because the typical lamella thickness in P3HB is rather low (in the order of 7 nm) some influence on the dislocation generation and kinetics were expected. Similar experiments with $\alpha$-iPP [3] revealed a strong increase of the dislocation density as a function of the plastic deformation with a limited reduction of the crystallinity. In the extruded P3HB samples a rather high initial dislocation density was found that did not increase with plastic deformation. The crystallinity showed a considerable decrease.

While the stress-strain curve of P3HB does not reveal any secial feature with respect to the deformation process involved, the cyclic-loading unloading reveals an increase in the opening of the cycles. This points at an increased activity of the amorphous phase. Together with a considerable amount of kinematic hardening at higher deformations and a high brittleness a deformation mechanism concentrated in the interlamellar areas leading to lamellar fragmentation is suggested. Apart from the dislocation density of $6.5 \cdot 10^{16}$ m$^{-2}$, MXPA also provides information on the size and size distribution. In P3HB the values found were very small and ranged from 6 to 11 nm.

In the third publication *"Determination of Lamella Thickness Distributions in Isotactic Polypropylene by X-ray Line Profile Analysis [S4]"* again the MXPA method was used as a tool to determine the lamella thickness distribution in $\alpha$-iPP of deformed and undeformed samples. Another possibility is the measurement of the lamella thickness by means of differential scanning calorimetry (DSC). This method implies the calculation of the thickness distribution from the melting point distribution of the lamellar crystals by a derivative formulation of the Gibbs-Thomson equation [74].

The agreement of the lamella thickness distributions of both methods is very good but it depends strongly on whether linear lattice defects, particularly dislocations are taken into account in the MXPA. Indeed in the deformed sample very high dislocation densities in the order of $10^{17}$ m$^{-2}$ are found. In the undeformed samples the dislocation density lies much lower (of the order of $10^{14}$ m$^{-2}$). Attempting the MXPA evaluation without dislocations indicates that, in the undeformed sample, the X-ray line broadening is almost fully governed by the restricted size (about 14 to 17 nm) of the crystallites.

Further DSC experiments in iPP filled with $TiO_2$ nanoparticles show a change in the crystallisation behaviour towards a multimodal distribution. Although a monomodal lognormal distribution was used for the MXPA evaluation, the agreement of both methods is still very good. The increased dislocation density indicates that the filler might hinder the growth of the crystallites as well as the annealing of crystalline defects.

An interesting future application could be the combination of MXPA with DSC. By careful

determination of the size distribution by DSC the number of free parameters in the MXPA could be considerably reduced, possibly providing more detailed information on the broadening caused by lattice strains i.e. the dislocations.

# 5. Determination of Critical Strains in Isotactic Polypropylene by Cyclic Loading - Unloading [S2]

*By analyzing the deformation of $\alpha$ - isotactic polypropylene through cyclic uniaxial compression at different temperatures, conclusions are drawn on the contribution of the crystalline phase and the amorphous phase to the hardening curve. The deformation of the crystalline phase, which deforms mainly by simple shear of the crystallites strongly depends on the properties of the amorphous phase. A separation of strain in a relaxing and a quasi-permanent part as introduced by the work of Hiss et al. [10] is undertaken. By this experimental procedure it is possible to characterize the deformation dependence of several physical quantities such as the Young's modulus or the stored energy associated to each loading - unloading cycle. Furthermore specific transition strains A,B,C and D can be determined where the recovery properties change. It is demonstrated that beyond the point C the strain hardening can be described by the simple rubber hardening model of Haward and Thackray [75].*

## 5.1. Introduction

The study of the mechanical and micromechanical properties of semicrystalline polymers has seen a considerable rise in the last years due to an overall increased use of polymer materials in technological applications. Numerous investigations concentrated on different types of polyethylene being relatively simple in its crystal structure as well as in its molecular structure. Studies in iPP, sPP, nylon or PET followed. The interactions of the amorphous and the crystalline phase as well as the phase specific structural changes as induced by plastic deformation still give reason to a number of questions. A prominent one among those is the question concerning the role of dislocations for the yielding of the crystalline phase [26, 3].

The underlying processes of the plastic deformation of semicrystalline polymers have been reviewed by Lin and Argon [5] and by Galeski [29]. Hiss et al. [10] carried out comparative studies of polyethylene and several copolymers with different crystallinities by means of uniaxial step cycle tensile tests. It was demonstrated that the stress-strain curve can be separated by

4 characteristic transition strains A,B,C,D where the recovery properties and the differential compliance change. Point A is related to the onset of isolated slip processes, point B occurs when a collective slip activity is induced. In the tension test C is determined by the beginning of fibrillation after fragmentation of the lamellar crystals. Bartczak [11] carried out step cycle tests on polyethylene in plane strain compression. In the highly constrained conditions of the plane strain compression tool he did not observe a widespread destruction of the lamellae and formation of microfibrils but rather a locking of the interlamellar shear. This leads to a localization of crystallographic slip and consequently to some destruction of the lamellae by cooperative kinking of stacked lamellae. Point D is related with the destruction of entanglements leading to non-recoverable deformation [76, 10].

In the present work, cyclic uniaxial compression tests have been carried out on isotactic polypropylene in order to determine the characteristic strains and to study the evolution of the elastic modulus with each cycle, as well as the development of the absorbed energy with each cycle.

## 5.2. Experimental

### 5.2.1. Material and sample preparation

The samples were produced from an extruded plate of isotactic polypropylene BE50 provided by Borealis company. Bars with the dimensions 10×10×200 mm were cut from the plate. In order to remove preferential orientations arising from the production process and to ensure a uniform spherulithic size distribution the samples were heat treated consisting of melting the samples and subsequently recrystallizing them at temperatures near the crystallization temperature $T_c = 165°C$ for two hours. Then cylindrical samples (diameter: 6 mm, height: 10 mm) were cut from the recrystallized bars.

### 5.2.2. Cyclic compression tests

Uniaxial compression step cycle tests were carried out at $T = -20\,°C$, $T = 20\,°C$ and $T = 50\,°C$ on a Shimadzu AG50 deformation machine in combination with a Shimadzu TCL N220 thermostatic chamber. Geometric stress-strain correction of the compressed samples was ensured by framing the maximum bulging diameter in reference tests with a digital camera [14]. Each sample was subjected to a set of 30 deformation cycles in constant steps of the true strain of $\Delta\epsilon_t = 0.05$ at a constant true strain rate of $\dot{\epsilon_t} = 4 \cdot 10^{-4}\,s^{-1}$. After each unloading the sample was allowed to relax for 10 minutes. The curves resulting from deformation at the three deformation temperatures are shown in Fig. 5.1.

### 5.2.3. Differential scanning calorimetry

Thermal analysis was performed on a Netzsch DSC 204 apparatus. The crystalline volume fraction was determined from the ratio of the heat of fusion of the sample $\Delta H$ and the heat of fusion of an ideally crystalline sample $\Delta H^0$. For the latter the widely accepted value $\Delta H^0 = 207\,J/g$ was assumed [77]. The lamella thickness was evaluated using the formula of Hoffman

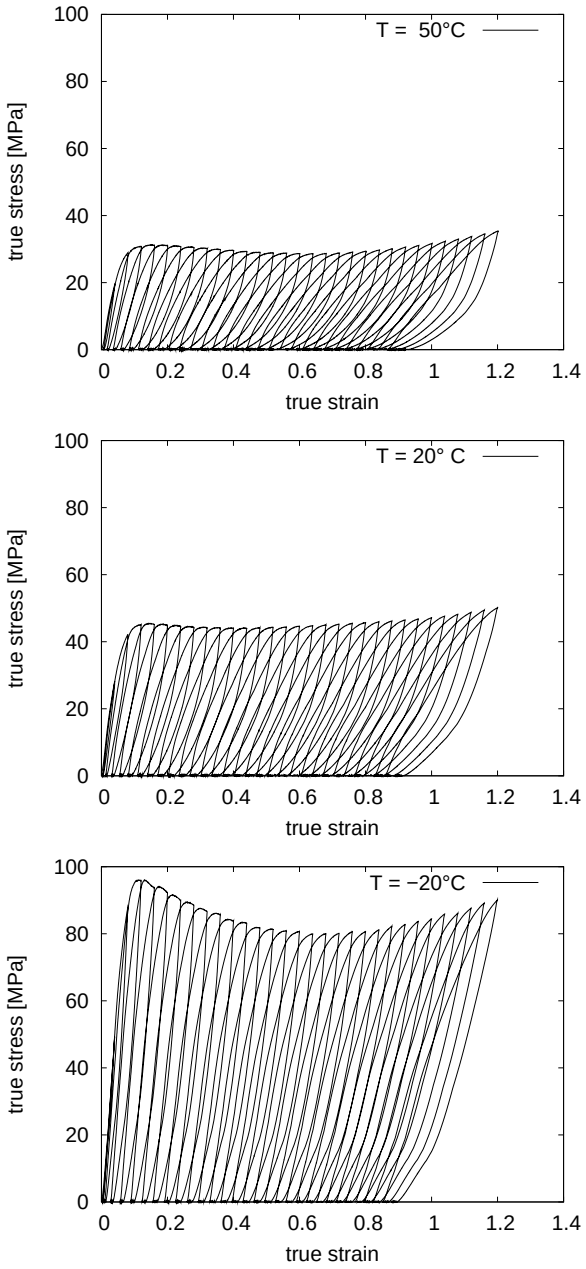


**Figure 5.1.:** Cyclic compression tests of isotactic polypropylene at a constant true strain rate $\dot{\epsilon}_t = 4 \cdot 10^{-4}\, s^{-1}$. Deformation temperatures were $-20\,°C$, $20\,°C$ and $50\,°C$

[78] predicting the influence of the lamella thickness $l$ on the equilibrium melting point $T_m$

$$l = \frac{2\sigma_e}{\Delta h_f \left(1 - \frac{T_m}{T_m^0}\right)}. \tag{5.1}$$

The free fold surface energy is assumed as $\sigma_e = 0.7\, J/m^2$ [79], the equilibrium melting point of the 100% crystalline material as $T_m^0 = 187.5\,°C (= 460.65\, K)$ [79]. The heat of fusion per unit volume

$\Delta h_f$ is calculated on the base of the density of perfectly crystalline $\alpha$-iPP $\rho_c = 0.936\,kg/m^3$ [79], and $T_0$ is the melting temperature as derived from the DSC experiments.

### 5.2.4. Wide angle x-ray scattering

As an additional method for the determination of the degree of crystallinity WAXS (wide angle x-ray scattering) was chosen. X-ray profiles were recorded by a Bruker AXS D8 Discover diffraction equipment with GADDS area detector operated at 40 kV and 40 mA with a filtered Cu $K_\alpha$ source after deformations $\epsilon_t = 0,\ 0,24,\ 0,52$ and $0,92$. For the purpose of a simplified texture correction, the signals of three orthogonal spatial directions were added and evaluated as a representative profile. The amorphous phase gives an diffuse signal which can be separated from the crystalline contribution by the application of a peak separation procedure. For this purpose the profile fitting software *Fityk* was used. The crystallinity can then be estimated from the relative total intensities resulting from this separation.

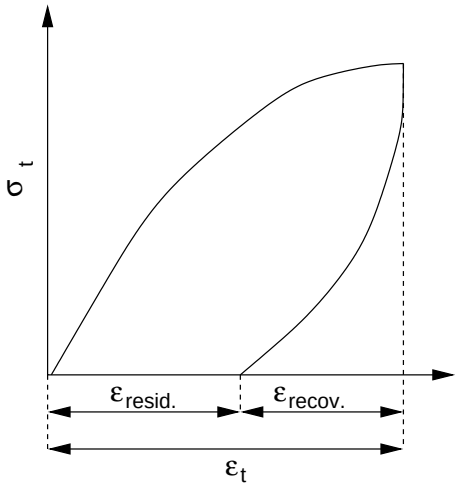


**Figure 5.2.:** Schematic representation of the division of the strain $\epsilon_t$ in a residual and a recoverable part.

## 5.3. Results and Discussion

Recovery effects were studied by means of cyclic loading-unloading experiments. The total strain achieved before unloading $\epsilon_t$ can be divided into two parts, a recoverable part $\epsilon_{recov}$ and a residual part $\epsilon_{resid}$ (Fig. 5.2),

$$\epsilon_t = \epsilon_{recov} + \epsilon_{resid}. \tag{5.2}$$

The change of the differential compliance of the recoverable strain $d\epsilon_{recov}/d\sigma_t$ occurs at characteristic points A, B, C and D corresponding to characteristic strains (Fig. 5.3).

The evolution of $\epsilon_{recov}$ and $\epsilon_{resid}$ as a function of the total strain is shown in Fig. 5.4 for the three deformation temperatures. The curves differ very little, only for the sample which was deformed at $-20°C$ the recoverable part is slightly lower than for the other two temperatures

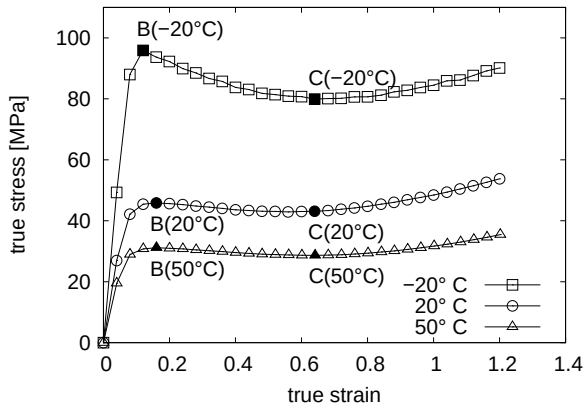


**Figure 5.3.:** Envelopes of the stress-strain curves of the cyclic compression tests for deformation temperatures $-20\,°C$, $20\,°C$ and $50\,°C$.

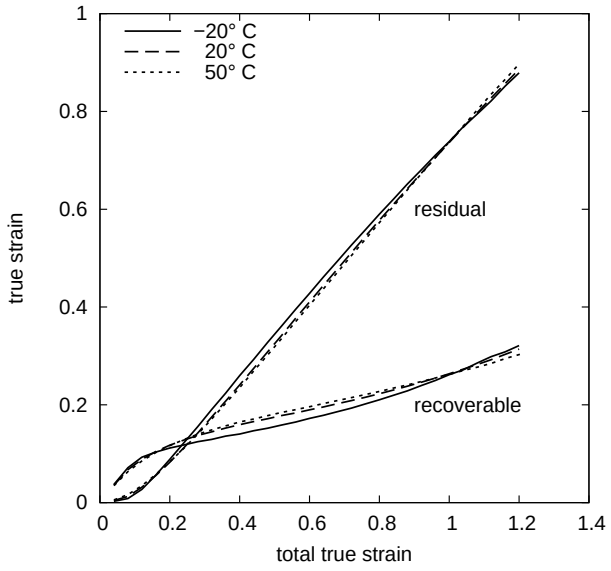


**Figure 5.4.:** Residual and recoverable strains for each cycle as a function of the total true strain, for the deformation temperatures $-20\,°C$, $20\,°C$ and $50\,°C$. The data points were omitted to increase clarity in this representation.

until a total true strain of about $\epsilon_t = 0.9$. This could be an effect of the glassy state of the amorphous phase at $-20°C$ hindering the relaxation process. But this effect is very small indicating that the recovery properties of the strain are not much affected by the temperature, a feature that is also reflected in the temperature dependence of the critical recoverable strains B and C as derived from the changes of slope of the recoverable strain (Figs. 5.5 and 5.6).

On the other hand, there is a strong influence of the temperature on the hardening characteristics after the point B. After this point softening occurs for all three deformation temperatures but this effect is much stronger for the samples deformed at $-20°C$.

The rubbery hardening related to the entanglement of the amorphous network depends only weakly on the deformation temperature. Haward and Thackray [75, 80] derived a simple model

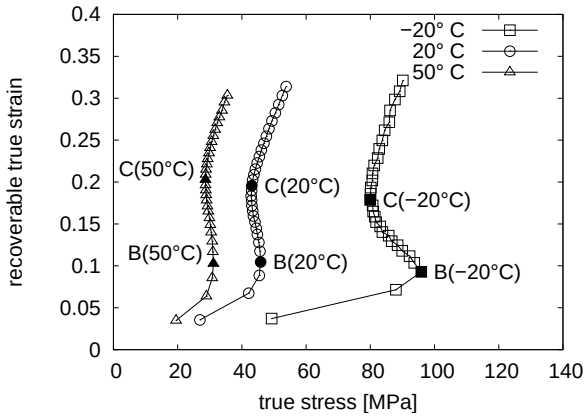


**Figure 5.5.:** Recoverable strains for each cycle as a function of the total true stress for the deformation temperatures $-20°C$, $20°C$ and $50°C$. The changes of the slope of this curve correspond to the critical strains.

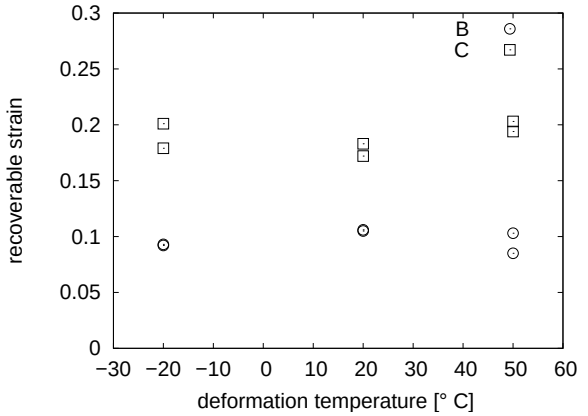


**Figure 5.6.:** Recoverable strains related to the critical strains B and C as a function of the deformation temperature.

for the description of the strain hardening of amorphous polymers based on gaussian chain statistics. Following this model, the amorphous network stress $\sigma_{nw}$ can be described as

$$\sigma_{nw} = G(\lambda^2 - 1/\lambda) \tag{5.3}$$

with $\lambda$ being the extension ratio and G the so called rubber modulus. Consequently, one can illustrate the influence of the amorphous phase by plotting the true stress against $(\lambda^2 - 1/\lambda)$. Fig. 5.7 shows such a representation of the stress strain data often referred to as Haward-Thackray plot [19, 10]. The point C as derived from the relaxation properties is also indicated in the graph. The linear behavior of the stress as a function of $(\lambda^2 - 1/\lambda)$ beyond point C as observed in the present experiments is characteristic for rubbery hardening. Thus point C can be considered as a transition point between a stage where the the hardening (softening) is determined by the crystalline flow towards a stage where hardening mechanisms related to the amorphous phase

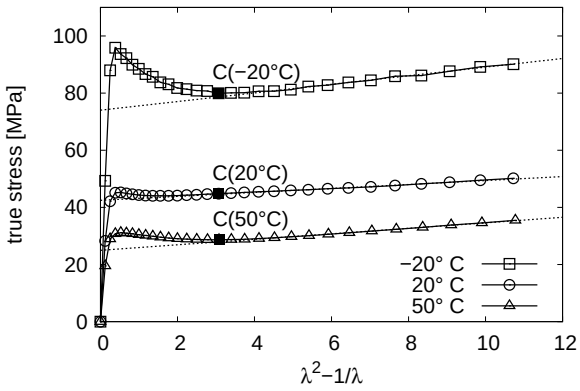


**Figure 5.7.:** Haward-Thackray plot for deformation temperatures $-20\,°C$, $20\,°C$ and $50\,°C$. After the critical point C the hardening can be described by the Haward-Thackray model.

dominate. The slope of the lines in Fig. 5.7 can be interpreted as a rubber hardening modulus. The rubber hardening moduli derived for the different temperatures amount to $G \approx 1\,MPa$ for $50\,°C$, $G \approx 0.8\,MPa$ for the room temperature experiment and $G \approx 1.5\,MPa$ for deformation at $-20\,°C$. Men et al. [81] considered the entanglement density to be the main microstructural parameters affecting the rubbery hardening in semicrystalline polymers, while tie molecules play a less important role in this process. Nonetheless they play a critical role for the interaction of the crystalline and the amorphous phase. The tie molecules allow for a reorientation of the crystalline lamellae favorable for crystalline slip in the regime between point A and B. At point B, massive crystalline slip occurs possibly also leading to a slight yield drop after this critical point. The slip leads to crystallographic rotation and a further stretching of the amorphous regions. As the rubber hardening modulus is relatively low the entanglement density should also be low. The entanglements are mainly responsible for the back-stresses allowing for a recovery of the strain. In the present material a high amount of unrecoverable deformation can be expected compared to PE [10] which is indeed confirmed by a previous investigation by Spieckermann et al. [72].

Fig. 5.8 illustrates the evolution of the crystallinity as a function of the true strain as derived from DSC and WAXS experiments. According to Hiss et al. [10] the point C is related to the onset of the destruction of the crystalline lamellae. The measured crystallinity is relatively stable until a true strain of about $\epsilon_t \approx 0.5$ and thus supports this interpretation. The lamella thickness was also evaluated from the measured DSC curves and a lamella thickness of about 20 nm was found for all samples (Fig. 5.9).

The energy absorbed by the sample during each loading unloading step can be evaluated by calculating the area under the curve during such a step. This energy increases monotonously for the temperatures for temperatures $20\,°C$ and $50\,°C$ but it saturates for the sample deformed at $-20\,°C$ which is below $T_g$. It is very probable that the increase of energy-consuming processes active above the glass transition is hindered by the glassy amorphous phase below the glass

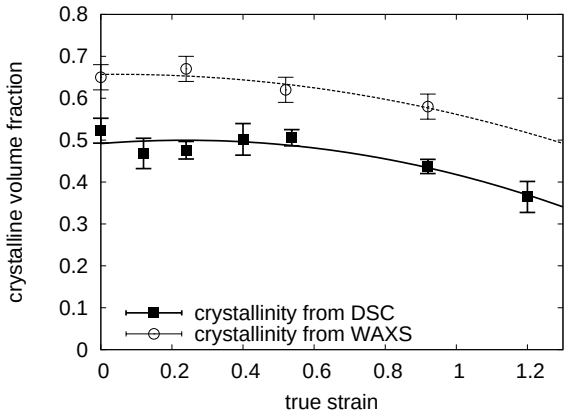


**Figure 5.8.:** Crystalline volume fractions for samples deformed up to different strains at $T = 20\,°C$ as determined by DSC and WAXS. The lines are for guiding the eye.

transition. Whether these processes are located in the crystalline phase as e.g. dislocation generation, or in the amorphous phase can only be speculated.

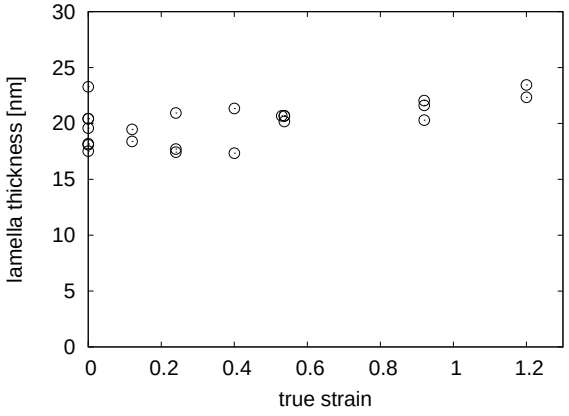


**Figure 5.9.:** Lamella thickness of samples deformed up to different true strains at $T = 20\,°C$ measured by DSC.

The elastic properties of the crystal lattice of iPP were measured by Sakurada et al. [82] showing a high anisotropy i.e. a high modulus parallel to the molecular chain direction and low moduli normal to the chain direction. Considering the slope at the start of each cycle in the stress-strain curve of the cyclic loading unloading experiments, the elastic secant modulus has been determined (Fig. 5.11). As the crystallinity is only reduced after a certain strain, the reduction of the elastic modulus with increasing total strain is probably related to orientational effects due to lamellar rotation.

## 5.4. Conclusions

In the present work, uniaxial loading-unloading experiments have been carried out on isotactic polypropylene in order to characterize the critical strains B and C related to the characteristic properties of the deformation of semicrystalline polymers. Similar experiments carried out in

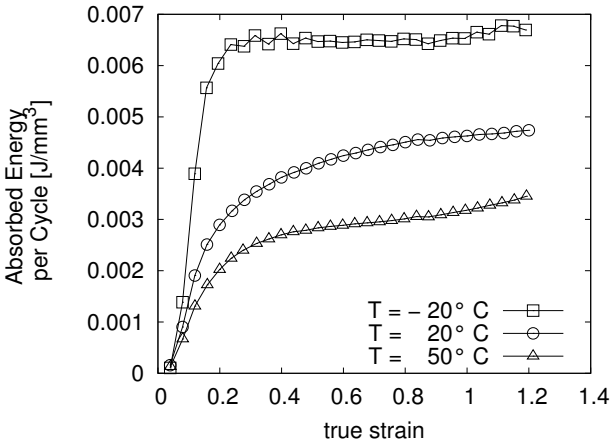


**Figure 5.10.:** Absorbed energy per cycle and unit volume as determined from cyclic loading unloading experiments for deformation temperatures $-20\,°C$, $20\,°C$ and $50\,°C$

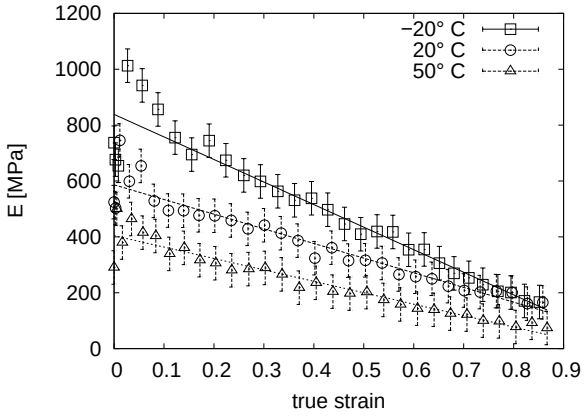


**Figure 5.11.:** Evolution of the elastic secant modulus for each cycle as determined from cyclic loading-unloading experiments for deformation temperatures $-20\,°C$, $20\,°C$ and $50\,°C$.

tensile deformation mode on PE and PE copolymers [10], PA [83], and sPP [84] related point B to the onset of massive crystallographic slip whereas point C was related to the onset of lamellar fragmentation. This study confirms these observations and demonstrates their applicability for isotactic polypropylene in compressive deformation. It is demonstrated that the transition point C is closely related to the locking of the flow in the entangled amorphous phase leading to a rubbery hardening that can be described by a Haward-Thackray Model.

## 5.5. Acknowledgments

The European Union project 'RTN-DEFINO' HPRN-CT-2002-00198 is gratefully acknowledged for financial support. Thanks are given to the University of Vienna for providing support within the PhD Program 'Experimental Materials Science - Nanostructured Materials' and the Focus Project 'Bulk Nanostructured Materials'.

# 6. Plasticity and X-ray Line Profile Analysis of the Semicrystalline Polymer Poly(3-hydroxybutyrate) [S3]

*The evolution of the microstructure during compressive deformation of the biodegradable polymer poly(3-hydroxybutyrate) (P3HB) was investigated in-situ via X-ray diffraction using synchrotron radiation. Flow curves were measured in-situ together with X-ray profiles for several degrees of deformation. The profiles were analysed using Multi-Reflection X-ray Line Profile Analysis (MXPA) adapted by the authors for semicrystalline polymers providing lamella thickness, crystallinity, and the presence and density of dislocations as a function of the deformation. In contrast to previous investigations in $\alpha$ crystallised isotactic polypropylene ($\alpha$-iPP), P3HB does not exhibit a deformation induced increase of the dislocation density which suggests mechanisms other than dislocations to be involved in plastic deformation of P3HB.*

## 6.1. Introduction

In a previous paper on $\alpha$ crystallised isotactic polypropylene ($\alpha$-iPP) [3] it has been demonstrated that the use of Multi-Reflection X-ray Profile Analysis (MXPA) as developed by Ungár and coworkers [56, 85] allows for the proof of the existence of dislocations in semicrystalline polymers. It was also possible for the first time to measure the density of dislocations quantitatively, which in the case of $\alpha$-iPP was found to increase with increasing plastic deformation.

In general, the mechanical properties and particularly the yield stress of semicrystalline polymers seem to be governed by the size of the crystalline lamellae rather than by the crystallinity [29]. For the mechanism related, Flory and Yoon [2] and Balta-Calleja and Cruz [35] suggested that plastic deformation in semicrystalline polymers is driven by localised melting and recrystallisation under adiabatic conditions. However, this concept is not able to account for the specific change in yielding behaviour for larger lamella thicknesses as it was observed experimentally in semicrystalline polyethylene [29]. Contrary to this concept, Argon et al. [26] suggested that the mechanisms in question involve dislocations i.e. by the thermally activated generation of dislocations on the surfaces of nano-sized lamellae, and by a dislocation half-loop mechanism

for larger lamellae. One strategy to shed more light on this problem is to investigate other types of semicrystalline polymers especially by means of MXPA which is capable of analysing the presence and density of dislocations on the one hand, and the lamella thickness on the other.

Recently the polyester poly(3-hydroxybutyrate) (P3HB) produced by microorganisms experienced some attention of the industrial community due to its high biodegradability. As the mechanical properties and the processibility are comparable to those of polypropylene (PP) this material qualifies for a number of future applications especially for medical and agricultural purposes.

From a scientific point of view, P3HB is particularly interesting for MXPA measurements because unlike many other semicrystalline polymers (a) its crystal system is simple orthorhombic and (b) its wide angle X-ray scattering (WAXS) pattern shows a large number of high intensity peaks [86], which is important for the efficiency of the MXPA. Moreover, the lamella thickness of P3HB is as small as 7 nm which should strongly affect the mechanical properties, and/or the generation dynamics of dislocations in case of their existence. Furthermore, there is only little data in the literature on the evolution of the microstructure of P3HB during deformation. Therefore the experiments presented in this paper aim at the presence of dislocations and potentially related deformation mechanisms in P3HB.

## 6.2. Experiments

### 6.2.1. Sample Preparation

P3HB rods were purchased from Goodfellow Cambridge Limited. For compression tests cylindrical samples with a height of 10 mm and a diameter of 6 mm were machined.

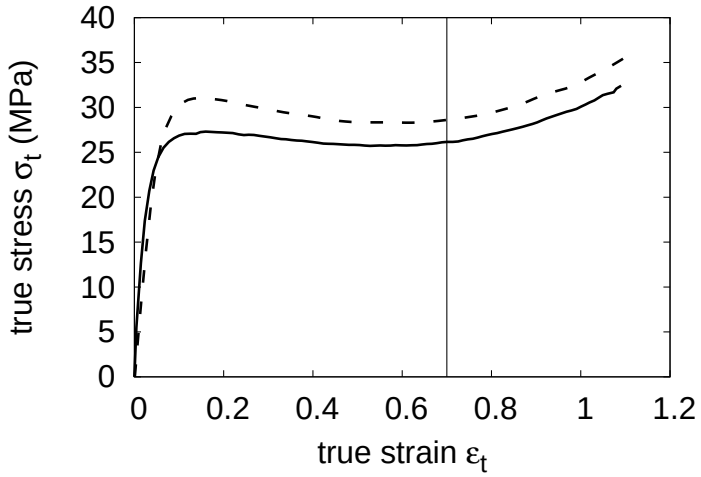


**Figure 6.1.:** Compression true stress-true strain curve of P3HB for strain rates of $\dot{\epsilon_t} = 4 \cdot 10^{-3}$ $s^{-1}$(dashed line) and $\dot{\epsilon_t} = 4 \cdot 10^{-4}$ $s^{-1}$(full line). After yielding a small softening is followed by a strong hardening beyond $\epsilon_t \approx 0.7$ (vertical line).

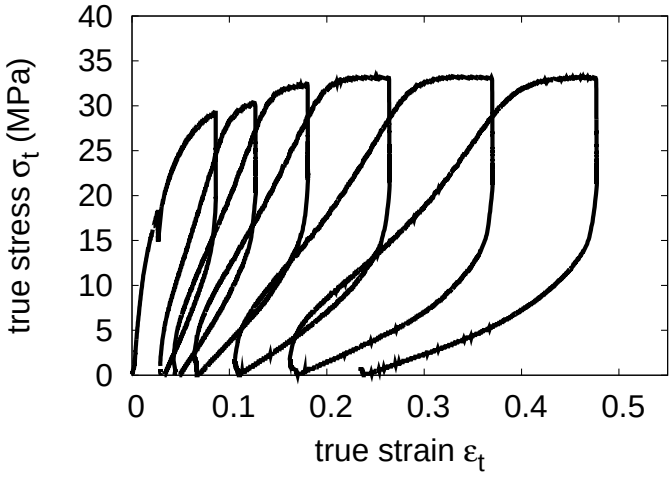


**Figure 6.2.:** Compression true stress-true strain curve of P3HB for cyclic loading-unloading of an in-situ MXPA-measured sample. The large opening of the cycles is an indication for strong activity of the amorphous phase.

### 6.2.2. Mechanical Experiments and In-situ Diffraction Experiments

Uniaxial compression tests were carried out at room temperature on a Shimadzu AG50 deformation machine. Geometric stress-strain correction of the compressed samples was ensured by a video extensometer capturing the maximum bulging diameter with a digital camera. The curves resulting from deformation at two different strain rates are shown in figure 6.1.

In-situ WAXS measurements during plastic deformation were performed in transmission setup at the SAXS-Beamline 5.2L of Sincrotrone ELETTRA Trieste. For this purpose a specially designed miniature compression machine was used. The stress-strain curve of a cyclic loading unloading experiment is depicted in figure 6.2. The photon energy used was 8 keV which corresponds to a wave length of $CuK_\alpha$ radiation of 0.154 nm. The incident beam had a spot size of 200 µm × 500 µm on the sample.

The photon flux amounted to $5 \cdot 10^{11}$ photons $\mathrm{mm}^{-2}\mathrm{s}^{-1}$. The WAXS spectra were recorded with a linear position-sensitive detector (1024 channels, type PSD 50 of Braun, Munich, Germany) at a distance of 370 mm between the detector and the specimen. To ensure sufficient statistics for a reliable evaluation of the WAXS profiles, at least $10^4$ counts were collected in the maxima of the diffraction peaks.

The recorded profiles were evaluated by means of the Multi-Reflection X-ray Line Profile Analysis (MXPA) [56, 85]. The evaluation procedure followed three steps, starting with the background determination and peak separation. After this a pre-fit of the components of the average dislocation contrast factor was done by evaluation of the modified Williamson-Hall plots. These values were then used as starting values for the evaluation with the program CMWP-fit [62, 87]. Details of this procedure are given in the papers by Wilhelm et al. [3] and Kerber et al. [88].

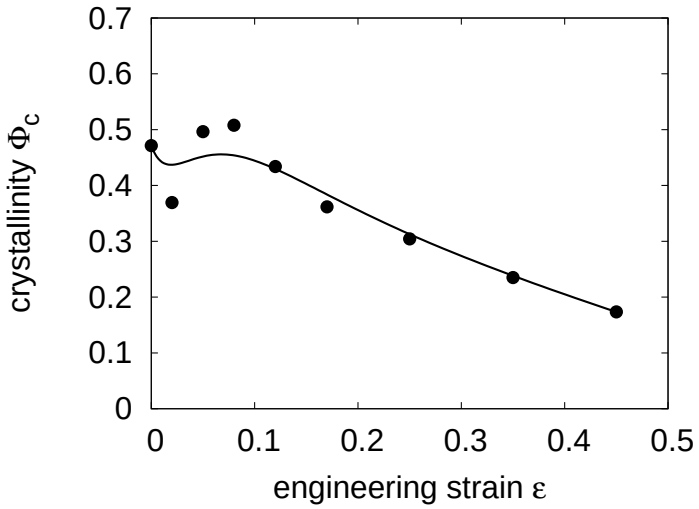


**Figure 6.3.:** The evolution of crystallinity (•) as a function of the engineering strain as derived from the deconvolution of the amorphous and the crystalline WAXS signals under compressive load. The line is added to guide the eye.

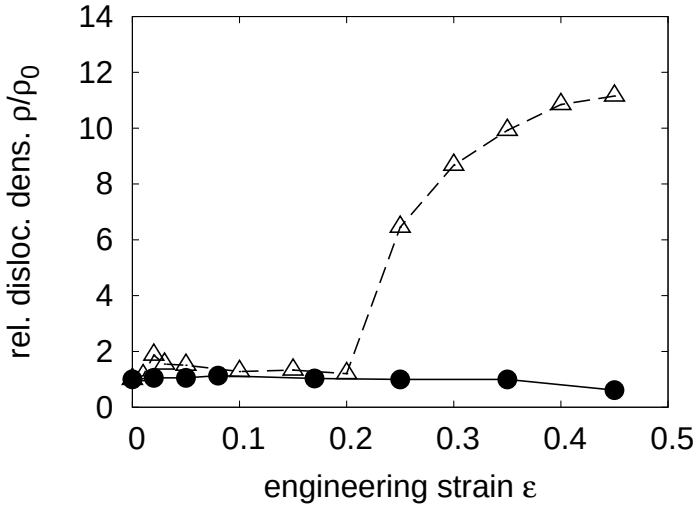


**Figure 6.4.:** Strain characteristics of the relative dislocation density in uniaxial compression for P3HB (•) and $\alpha$-iPP (△) as a function of the engineering strain. In-situ diffraction patterns were recorded under load.

## 6.3. Results and Discussion

Surprisingly the change of the profile broadening induced by plastic deformation found in P3HB seems to be very small. Earlier investigations of X-ray line broadening in $\alpha$-iPP [3] revealed a strong deformation induced increase of the broadening. This could be related to the formation of dislocations while the coherently scattering domain size (CSD) (which is also responsible for an important part of the broadening) remained nearly constant. Nevertheless the CSD was found to correspond very well to the lamella size of $\alpha$-iPP as determined by DSC or SAXS [S2][89]. In

the present investigation of P3HB, a stronger scattering for the CSD in comparison with $\alpha$-iPP is found which results in a CSD between 6-11 nm. The broadening related to dislocations, however, does not seem to be affected by deformation (figure 6.4). Although in absolute terms the initial dislocation density turns out to be even higher in P3HB ($6.5 \cdot 10^{16}$ m$^{-2}$) than in $\alpha$-iPP ($3.8 \cdot 10^{16}$ m$^{-2}$[3]) it does hardly change as a function of the compressive strain applied (figure 6.4). This contrast to the observations in $\alpha$-iPP indicates that in P3HB a different deformation mechanism is active. Different explanations may account for the unexpected behaviour of P3HB:

1. The dislocation density is high enough to accommodate the crystallographic slip, and generation and annihilation of dislocations may be in balance.

2. Intralamellar slip occurs with a mechanism other than dislocation motion, e.g. localised adiabatic melting [2] without mobilisation of dislocations.

3. Interlamellar processes are responsible for the main part of the deformation due to a high stiffness of the crystallites. In this case the lamellar crystallites would fragment before crystallographic slip occurs. Like mechanism (2), also this mechanism would not involve dislocation motion.

As the interaction between dislocations in polymers is expected to be low [29] the hardening curve in figure 6.1 cannot be used to decide between the three processes. The opening of the cycles shown in figure 6.2 increases with deformation. According to Hiss et al. [10] this can be attributed to the viscoelastic properties of the amorphous phase. The strong reduction of the crystalline volume fraction plotted in figure 6.3 is in accordance with this observation, since it suggests a stronger influence of the amorphous phase on the relaxation and deformation behaviour of the material. Both observations support the occurrence of mechanisms (2) and (3). In particular, the considerable amount of kinematic hardening which can be seen in figure 6.2, and the marked brittleness of the bulk material hint at the formation of cracks as suggested by mechanism (3).

Nevertheless, the real reasons for the occurrence of a deformation mechanism in P3HB, which is different to that operating in $\alpha$-iPP remain unclear. Future measurements of the deformation induced texture might prove useful in order to identify possibly activated slip systems. Transmission and/or scanning electron microscopy should give insight in how far fragmentation of the crystallites occurs with deformation.

## 6.4. Summary and Conclusions

With the present experiments, using the method of Multiple X-ray Profile Analysis, for the first time the existence of dislocations in melt-crystallised P3HB was shown. A considerable initial dislocation density of $6.5 \cdot 10^{16}$m$^{-2}$ was found. However, a deformation-induced change in the dislocation density has not been observed in P3HB which suggests one of the following microstructural deformation mechanisms to occur: (1) a balance of dislocation annihilation

and generation, (2) deformation-induced adiabatic melting, and (3) brittle fragmentation of the lamellae.

### 6.4.1. Acknowledgements

Support by the EU contract RII3-CT-2004-506008(IA-SFS) is gratefully acknowledged. Thanks are given to the University of Vienna for providing support within the PhD Program 'Experimental Materials Science – Nanostructured Materials' and the Focus Project 'Bulk Nanostructured Materials'.

# 7. Determination of Lamella Thickness Distributions in Isotactic Polypropylene by X-ray Line Profile Analysis [S4]

*X-ray line profile analysis was used to determine the size distribution of the crystalline lamellae in isotactic polypropylene (iPP) assuming a log-normal size distribution. A comparison with the size distribution as determined by differential scanning calorimetry (DSC) yields an excellent agreement of both methods. It is noted that the agreement depends strongly on whether linear lattice defects, particularly dislocations are taken into account in the X-ray analysis. This is especially true for deformed iPP with a high number of deformation induced dislocations. It was also found that for a multimodal distribution of lamella thickness in the DSC experiment as induced by the introduction of titanium dioxide nano particles as filler material the lamella thickness distribution from X-ray profile analysis is still in good agreement with DSC although the model used was only monomodal.*

## 7.1. Introduction

The deformation mechanisms and thus the mechanical properties of semicrystalline polymers depend strongly on the microstructure. Particularly the thickness of the crystalline lamellae seems to be a crucial parameter with respect to the mechanical strength [32].

For the determination of the lamella thickness in semicrystalline polymers several experimental methods exist, including differential scanning calorimetry (DSC), small angle X-ray scattering (SAXS), electron microscopy and optical methods. Attempts were also made to determine the crystallite size by evaluation of wide angle X-ray scattering (WAXS) profiles using the width of the Bragg-peaks through a separation of size broadening and broadening caused by statistical lattice defects, the latter commonly described by models of paracrystallinity [90, 91, 92].

In the present paper the crystallite size distribution in $\alpha$ nucleated isotactic polypropylene is determined using a Bragg-peak-profile analysis method that has so far not found extensive application in polymeric materials. In contrast to the earlier investigations the present work uses multi reflection X-ray line profile analysis (MXPA), which takes into account several Bragg

reflections (optimally also the upper harmonics of a reflection). From investigations in metals and ceramics [55, 71, 85] it is known that the procedure allows to determine the size distribution and the shape of the crystallites with a high reliability from a single WAXS pattern. To check the validity of the method in the semicrystalline polymer iPP the resultant size distributions are compared to distributions obtained from DSC.

## 7.2. Theory

### 7.2.1. Multi Reflection X-ray Line Profile Analysis (MXPA)

In the kinematic theory of X-ray diffraction the physical profile of a Bragg reflection is given by the convolution of the intensity profiles caused by finite size and by lattice distortions. The logarithm of the Fourier transform yields the well known Warren-Averbach formula [57]

$$\ln A(L) = \ln A^S(L) + \ln A^D(L) \tag{7.1}$$

where $A(L)$ are the Fourier coefficients of the Bragg profile ($L$ is the Fourier length), $A^S(L)$ and a $A^D(L)$ are the coefficients related to the size and the strain broadening respectively. The strain broadening is modelled by assuming that it is caused by the mean square strain $\langle\epsilon^2\rangle$ leading to a Fourier coefficient $A^D(L)$ of the form

$$A^D(L) = \exp\left(-2\pi^2 L^2 k^2 \langle\epsilon^2\rangle\right) \tag{7.2}$$

with $k$ the diffraction vector.

For the evaluation of crystalline defects the characteristic anisotropy of $\langle\epsilon^2\rangle$ can be related to the defects in question thus allowing for a separation of the broadening related to the size and to crystalline defects of linear (dislocations) and planar nature (twins, stacking faults) [56, 64]. In the present case only dislocations were considered.

As nucleation controlled crystallisation processes often lead to a log-normal size distribution [93], the peak broadening caused by the finite size is taken into account by such a distribution. The corresponding density distribution function of the size $\lambda$ has the form

$$f(\lambda) = \frac{1}{\lambda\sigma\sqrt{2\pi}} \exp - \frac{(\ln\lambda - \ln m)^2}{2\sigma^2} \tag{7.3}$$

with the parameters $m$ and $\sigma$ where $\mu = \ln m$ is the median and $\sigma$ is the variance of the distribution.

For the evaluation of the X-ray line broadening the program *CMWP-fit* (Convolutional Multiple Whole Profile fitting), developed by G. Ribarik et al. [62, 87], was used as it provides a very sophisticated and flexible evaluation procedure. In the software, the size broadening is taken into account by assuming a log-normal distribution (Eq. 7.3) with the fitting parameters $b = \ln m$ and $c = \sqrt{2}\sigma$.

The shape of the crystallites is modelled as rotation ellipsoids with an ellipticity parameter

$\epsilon$ also possible to be fitted by *CMWP-fit*. The model parameters related to the dislocation broadening are $a_1, \ldots, a_5$ (for the average dislocation contrast factor $\bar{C}$ of an orthorhombic[1] lattice) , $d$ (related to the dislocation density $\rho = 2/(\pi B^2 d^2)$, $B = 0.22$ nm [51] being the Burgers vector) and $e$ (related to the dislocation cut-off radius $R_e^* = exp(-1/4)/(2e)$). Furthermore the intensity and position of each Bragg peak can be fit parameters in *CMWP-fit*. All fit parameters in *CMWP-fit* can be fixed to a certain value. This is essential to restrict the number of parameters to be determined from fitting to the unknown quantities. The peak positions and intensities as well as the contrast parameters $a_1, \ldots, a_5$ are typical examples of parameters that can be determined independently, thus allowing to hold them fixed in the evaluation with *CMWP-fit*.

The effect of defect induced broadening can be directly inspected using the Williamson and Hall method [94] and its modified version [56, 69]. Plotting the full width at half maximum $k_{FWHM}$ of the peaks as a function of their diffraction vector $k$ allows for a first simple separation of the effects of size and strain broadening. Any deviation of the data from a monotonous behaviour is an indication of anisotropic strains. Assuming that the anisotropic strains are caused by dislocations, the modified Williamson-Hall plot accounts for the defect-specific broadening using the average contrast factor for dislocations $\bar{C}$. Plotting the peak width as a function of $k\sqrt{\bar{C}}$ should result in a monotonic behaviour if the anisotropy is correctly described by the model used for the distortions [56, 3, 69].

### 7.2.2. Lamella Thickness Distributions from DSC

DSC experiments can be used as a tool for the determination of crystal thickness distributions in semicrystalline homopolymers [95, 96, 74]. This procedure has the advantage to be a fast method with simple sample preparation resulting in an integral information over the whole sample volume. Yet several aspects have to be considered in order to obtain correct size distributions most notably the effects of the melting kinetics of the investigated polymer as well as effects due to the calorimeter used. The determination of size distributions from DSC builds on the fact that the melting temperature $T_m$ is related to the thickness $\lambda$ of the plate-like crystallites by the Gibbs-Thomson equation

$$T_m = T_m^0 \left(1 - \frac{2\sigma_e}{\Delta h_c \lambda}\right). \tag{7.4}$$

For $\alpha$-iPP the free fold surface energy is assumed as $\sigma_e = 0.07$ J/m$^2$, the equilibrium melting point of the 100% crystalline material as $T_m^0 = 187.5$°C(= 460.65 K) [79, 97]. The heat of fusion per unit volume $\Delta h_c$ is calculated from the heat of fusion of an ideally crystalline sample ($\Delta H^0 = 207$ J/g) on the basis of the density of perfectly crystalline $\alpha$-iPP $\rho_c = 936$ kg/m$^3$ and $T_m$ is the melting temperature as derived from the DSC experiments [79, 97].

[1] It is reasonable to assume an orthorhombic lattice for the contrast calculation as the effect of the monoclinic angle is negligible in first approximation [3].

In order to derive the lamella thickness distribution from the DSC experiment (measuring $P(T)$, the power absorbed at temperature $T$), Alberola et al. [98] and later Crist and Mirrabella [74] showed that a derivative formulation has to be considered. This is necessary because the DSC signal $P(T)$ is proportional to the melting distribution and cannot be used directly as a size distribution function as it was done by some authors. The resulting size distribution function for a constant heating rate $\beta = dT/dt$ was found as

$$g(\lambda) = \frac{P(T)}{\alpha_m \Delta H^0 M(dT/dt)} \frac{dT}{d\lambda} \tag{7.5}$$

where $\alpha_m$ is the mass fraction crystallinity and $M$ the sample mass. Setting $T_m = T$, substituting Eq. 7.4 in Eq. 7.5 and assuming $\Delta h_c$ to be temperature independent allow the size distribution function to be written as:

$$g(\lambda) = KP(T)(T_m^0 - T)^2. \tag{7.6}$$

The normalization constant $K$ can be considered as temperature independent and is therefore determined by numerical integration of $P(T)(T_m^0 - T)^2$ [74].

## 7.3. Experimental

Isotactic polypropylene BE50 by Borealis company, which is delivered with an $\alpha$ nucleation agent securing nucleation of a homogeneous spherulitic structure, was used. Bars with the dimensions $10\times10\times200$ mm$^3$ were cut from an extruded plate. A heat treatment consisting of melting and subsequently recrystallising near the crystallisation temperature $T_c = 165°$C for two hours ensured low preferential orientations and a uniform spherulitic size distribution. Cylindrical samples (diameter: 6 mm, height: 10 mm) were machined for X-ray experiments. Platelets with 1 mm thickness were cut with a diamond saw, from which discs of about 20 mg where punched out for differential scanning calorimetry (DSC). The experiments were carried out on a Netzsch DSC 204 calorimeter under argon atmosphere to avoid effects by oxidation or condensation. In order to minimise effects by lamellar thickening, a heating rate of 10 K/min was chosen. The shift of $T_m$ related to the rate sensitivity of the melting kinetics was accounted for by a correction factor determined by linear approximation of the rate dependence of the melting temperature $T_m(\beta)$ (Fig. 7.1).

WAXS measurements were performed in transmission setup at the SAXS-Beamline 5.2L of the synchrotron ELETTRA (Trieste, Italy). After recording the profile at the undeformed state the sample was deformed up to a true strain of $\epsilon_t = 0.5$ using a miniature compression machine allowing for in situ deformations, recording several profiles over the whole deformation range. Collecting the data under load makes it possible to minimise relaxation effects of the deformed sample.

The photon energy used was 8 keV, which corresponds to a wave length of $CuK_\alpha$ radiation of 0.154 nm. The incident beam had a spot size of 100 µm$\times$ 400 µm on the sample and the

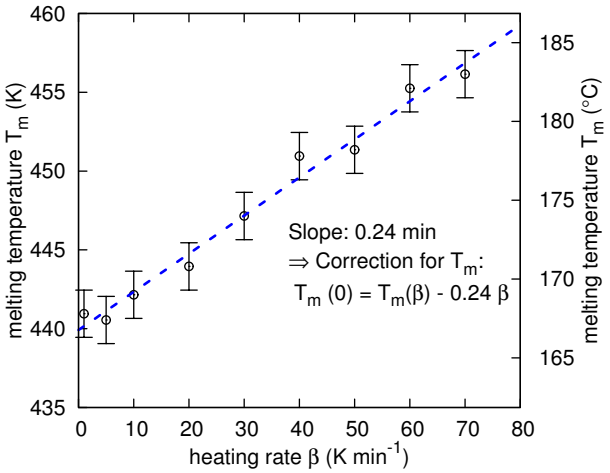


**Figure 7.1.:** Offset of the melting temperature $T_m$ as determined by DSC (∘) as a function of the heating rate. The slope of the fit (dashed line) amounting to 0.24 min is used to determine $T_m(0)$.

photon flux amounted to $5 \cdot 10^{11}$ photons mm$^{-2}$s$^{-1}$. The WAXS spectra were recorded with a linear position-sensitive detector (1024 channels, type PSD 50 of Braun, Munich, Germany) positioned at a distance of 370 mm from the specimen. To ensure sufficient statistics for a reliable evaluation of the Bragg profiles at least $10^4$ counts were collected in the maxima of the diffraction peaks.

For comparison further experiments were carried out on samples of the same polypropylene type but filled with a small amount of titanium dioxide ($TiO_2$) nanoparticles. To this end, 5 wt. % of $TiO_2$ (Degussa Aeroxide P25, particle size range 20 – 80 nm) were carefully distributed and dispersed in the iPP matrix by extrusion

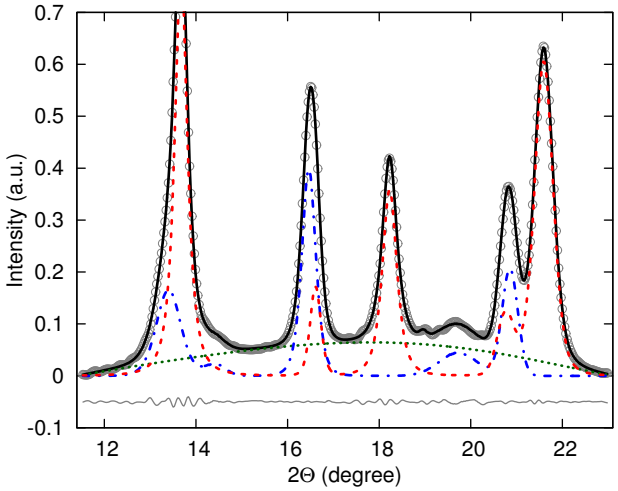


**Figure 7.2.:** WAXS pattern of undeformed iPP, measured data (∘), fit (full line), $\alpha$-phase (dashed line), $\gamma$-phase (dash-dotted line), amorphous phase (dotted line), residuals (gray line)

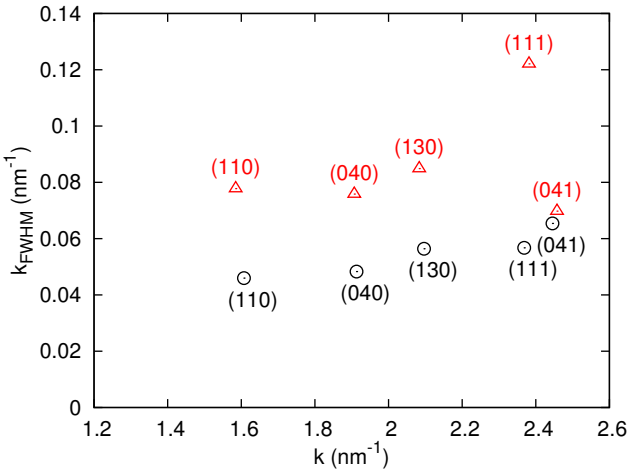


**Figure 7.3.:** Williamson-Hall plots of $\alpha$-iPP before deformation ($\circ$), and after deformation up to $\epsilon_t = 0.5$ ($\triangle$).

## 7.4. Results and Discussion

The recorded diffraction patterns were subjected to a pre-evaluation (using *GNU octave* [99] and *fityk* [100] software). In order to properly determine the background mainly arising from the scattering of the amorphous phase a $5^{\text{th}}$ order polynomial is used. A small amount of $\gamma$-crystallised iPP resulted in diffraction peaks at known positions. To determine peak positions and intensities of all known phases, the peaks were, in a first step, approximated using Pearson VII functions also giving reasonable widths for each peak. The number of fit parameters was reduced using known ratios of peak positions where possible, greatly improving the reliability. The excellent result of this separation procedure is shown in Fig. 7.2. For the CMWP procedure, the background and the additional phase were then subtracted in order to obtain exclusively the diffraction profile of the $\alpha$ phase. Furthermore the peak widths fitted in the pre-evaluation were used to determine appropriate parameters for the average contrast factor $\bar{C}$ by Williamson-Hall (W-H) analysis, to be used later on in the *CMWP-fit*. A detailed description of this procedure is given by Wilhelm et. al [3] and Spieckermann et al. [S3]. The Williamson-Hall plots of undeformed and deformed $\alpha$-iPP (Fig. 7.3) show that the deformation increases the anisotropy of the broadening as indicated by the scattering of the peak width of the deformed sample. The modified Williamson-Hall plot (Fig. 7.4) shows that by determination of the dislocation contrast factor $\bar{C}$ a linearisation as a function of $k\sqrt{\bar{C}}$ is possible. This is already a strong sign for the presence of dislocations as it was reported by Wilhelm et. al [3]. The slope of the fitted lines is proportional to the square root of the dislocation density [56] and it clearly increases with deformation.

The adapted profiles were consequently evaluated with *CMWP-fit*. The resultant fit parameters and their physical correspondence are given in Table 7.1 for the undeformed sample and in Table 7.2 for the sample deformed up to a true strain of $\epsilon_t = 0.5$.

While the diffraction experiments yield the size of the coherently scattering domains (CSD,

**Table 7.1.:** *CMWP-fit* Parameters for undeformed $\alpha$-iPP and related physical quantities.

| Param. | Value | Physical Quantity | Value |
|---|---|---|---|
| $\epsilon$ | 0.90 | size ellipticity $\epsilon$ | 0.90 |
| b | 2.79 | size median $\mu$ | 16.10 nm |
| c | 0.33 | size variance $\sigma$ | 0.24 |
| $a_1 \ldots a_5$ | fixed | average contrast factor $\bar{C}$ | from W-H |
| d | 61.5 | dislocation density $\rho$ | $7.6 \cdot 10^{14}\mathrm{m}^{-2}$ |
| e | 0.04 | dislocation cut-off radius $R_e^*$ | 9.6 nm |

**Table 7.2.:** *CMWP-fit* Parameters for $\alpha$-iPP deformed up to $\epsilon_t = 0.5$ and related physical quantities.

| Param. | Value | Physical Quantity | Value |
|---|---|---|---|
| $\epsilon$ | 1 | size ellipticity $\epsilon$ | 1 |
| b | 2.66 | size median $\mu$ | 14.30 nm |
| c | 0.25 | size variance $\sigma$ | 0.17 |
| $a_1 \ldots a_5$ | fixed | average contrast factor $\bar{C}$ | from W-H |
| d | 10.55 | dislocation density $\rho$ | $1.2 \cdot 10^{17}\mathrm{m}^{-2}$ |
| e | 0.04 | dislocation cut-off radius $R_e^*$ | 8.7 nm |

**Table 7.3.:** *CMWP-fit* Parameters for $\alpha$-iPP filled with 5 wt. % $TiO_2$ nanoparticles and related physical quantities.

| Param. | Value | Physical Quantity | Value |
|---|---|---|---|
| $\epsilon$ | 0.98 | size ellipticity $\epsilon$ | 0.98 |
| b | 2.73 | size median $\mu$ | 15.28 nm |
| c | 0.27 | size variance $\sigma$ | 0.19 |
| $a_1 \ldots a_5$ | fixed | average contrast factor $\bar{C}$ | from W-H |
| d | 12.9 | dislocation density $\rho$ | $8.2 \cdot 10^{16}\mathrm{m}^{-2}$ |
| e | 0.03 | dislocation cut-off radius $R_e^*$ | 12.9 nm |

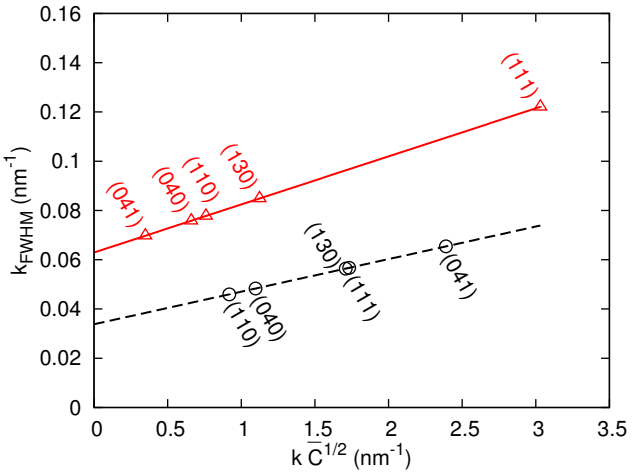


**Figure 7.4.:** Modified Williamson-Hall plots of $\alpha$-iPP before deformation ($\circ$), and after deformation up to $\epsilon_t = 0.5$ ($\triangle$).

i.e the smallest undistorted crystals) the DSC experiments should, according to the theory of Hoffmann and Miller [78], yield the stem length (i.e. the distance of two adjacent fold surfaces along the molecular chain). Hence, both methods provide quantities measured along the crystallographic axes and it is reasonable to attempt a comparison.

The size distribution as determined via DSC is very close to a log-normal distribution, which is common for size distributions resulting from nucleation controlled processes of nanocrystals [55, 71, 85]. It is therefore reasonable to approximate the distribution by fitting the corresponding distribution function. When comparing the DSC experiments to the results from the MXPA experiments one finds that both log-normal distributions coincide very well for the melt crystallised $\alpha$-polypropylene (Fig. 7.5 (a)) as well as for the deformed state (Fig. 7.5 (b)). The dislocation density, also determined via MXPA is increased considerably by the plastic deformation as it can be seen when comparing the results presented in Tables 7.1 and 7.2. A reasonable dislocation cut-off radius in the order of the lamella thickness is found and the $\epsilon$ parameter indicates only a slight deviation from the spherical shape.

To study the influence of the crystalline defects on the evaluated size distribution, it was assumed that the crystal is virtually dislocation free for the deformed as well as for the undeformed state. This assumption was modelled in the *CMWP-fit* by fixing the parameter $d$ at a value of $10^5$ corresponding to a dislocation density of only $\sim 10^9$ m$^{-2}$. The resultant size distributions for the deformed and the undeformed case are depicted in Fig. 7.5 as dotted curves. For the undeformed sample fixing the dislocation density has only marginal effect on the size distribution evaluated via MXPA, attributed to the relatively low dislocation density. This is in contrast to the deformed case where a strong difference to the DSC curve is seen when assuming no dislocations present in the material while including the dislocations in the *CMWP-fit* gives good agreement between DSC and X-ray results.

For the correct determination of the lamellar sizes it is therefore crucial to consider the in-

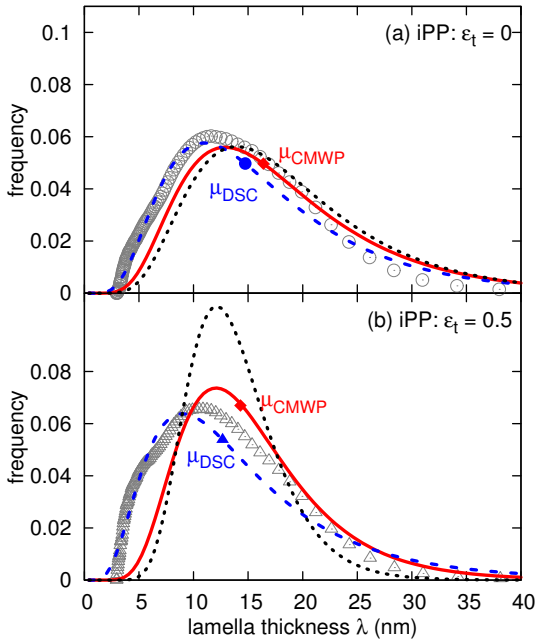


**Figure 7.5.:** Lamella thickness distribution determined for (a) undeformed iPP and (b) iPP deformed up to $\epsilon_t = 0.5$ by DSC (undeformed: ∘, deformed: △) and MXPA (full line). The dashed lines represent the corresponding log-normal fit of the respective DSC distribution. The respective results of MXPA with very low assumed dislocation densities are plotted as dotted lines.

fluence of crystalline defects, especially when their number is high as in case of the deformed sample. Apart from the fact that the quality of the model fit is better when assuming the presence of dislocations these observations are a strong indication that a considerable part of the broadening is caused by linear defects i.e. dislocations. On the other hand the results also show that the broadening in the undeformed state is highly governed by the crystallite size.

Repeating the procedure for the samples filled with 5 wt. % $TiO_2$ shows that a slight deviation from the monomodal log-normal distribution to a bimodal distribution is seen via DSC. Possibly a fraction of the introduced particles hinders crystallisation locally leading to regions that are only poorly crystallised and other regions where crystallisation is not hindered. Such a behaviour could result in the observed bimodal size distribution. Still as a first approximation and in order to compare with the CMWP results, a log-normal distribution is fitted to the DSC size distribution. A reasonable agreement is found and even the medians of the (monomodal) size distributions determined by DSC and MXPA are in fairly good agreement (Fig. 7.6). The relatively high dislocation density (Table 7.3) also suggests that the filler interferes in the crystallisation thus also inducing a lower degree of crystalline order.

## 7.5. Conclusions

MXPA proved to be effective to determine the size distribution of the crystalline lamellae in $\alpha$ crystallised polypropylene. The presence of crystalline defects has to be taken into account in

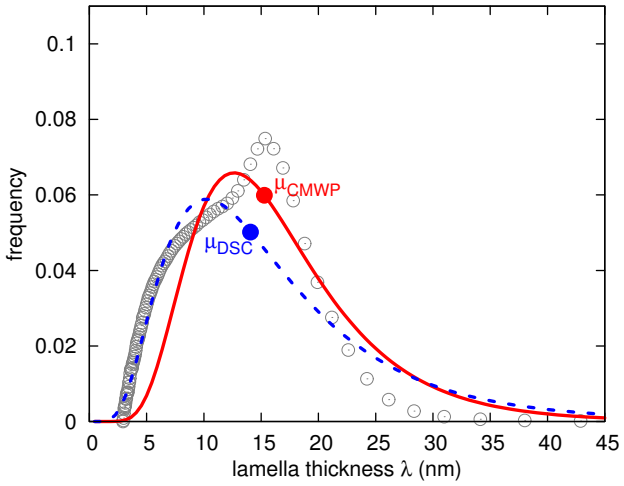


**Figure 7.6.:** Lamella thickness distribution determined for iPP-$TiO_2$ by DSC (∘) and MXPA (full line). The dashed line represents the corresponding log-normal fit of the DSC distribution.

order to achieve correct crystallite size distributions. In deformed samples the dislocation density turns out to be markedly higher than in the undeformed state and a correct determination of the size distribution from MXPA is only possible if these dislocations are considered. This supports findings from earlier experiments assuming the presence of dislocations in bulk polypropylene.

The good agreement between X-ray and DSC results opens the possibility to use DSC to determine reasonable starting parameters for MXPA. By direct numerical computation of $A^S(L)$ from $g(\lambda)$ one could even account completely for the size broadening in future X-ray investigations of semicrystalline polymers.

MXPA should also be applicable to other crystallisable polymers, provided that a sufficient number of reflections is detectable. This is necessary to make use of the ability of the method to fully characterise defect induced strains, and thus allow for the correct quantification of the size related part of the line broadening. Indeed first investigations in poly-3(hydroxbuthyrate) [S3] also gave reasonable results.

It was also shown that a pitfall in the application of MXPA as a tool for the determination of the crystallite size in semicrystalline polymers lies in the danger to use the wrong model distribution (log-normal, gamma, ... ) or have a multimodal distribution. This will especially be crucial when dealing with copolymers where monomodal distributions are rare.

## Acknowledgements

Funding by the University of Vienna within the PhD Program 'Experimental Materials Science – Nanostructured Materials' and the Focus Project 'Bulk Nanostructured Materials' is gratefully acknowledged. Daria Setman and Dr. Thomas Kratochvilla are thanked for advice concerning the DSC experiments and their evaluation.

# Part III.

# Results and Discussion: Unpublished Results

In this part of the thesis results that have so far not found their way into publications will be presented. Chapter 8 deals with the experimental investigations. These results include investigations on iPP but also on PHB and HDPE. The chapter contains result of mechanical experiments, DSC, X-ray diffraction, and electron microscopy. It also includes descriptions of the experimental procedures which exceed the short introduction of the publications. Chapter 9 presents calculations of the dislocation contrast of iPP and first applications to experimental data.

# 8. Experimental Investigations

## 8.1. Introduction

In order to better interpret the findings of the preceding part II further experimental investigations were carried out. The results are presented in this chapter.

First, to gain a deeper understanding of the the mechanical properties of semicrystalline polymers, a number of mechanical experiments were performed. As the focus of this thesis lies in the investigation of the mechanical response of the crystalline phase and on the role of dislocations, compression was chosen as the deformation mode. This deformation mode has the advantage that it suppresses voiding and crazing (see section 2.1.4). Additionally to the experiments concerned with iPP and PHB reported in the publications [S2, S3] included in Chapters 5 and 6 a detailed discussion of cyclic loading unloading of PHB and a HDPE-butene copolymer are included.

The second focus of this chapter presents differential scanning calorimetry, electron microscopy, and X-ray profile analysis mainly concerned with PHB and a few results from investigations of iPP. These investigations were particularly aimed at an understanding of the different mechanism of plasticity observed in PHB.

## 8.2. Methods

### Cycling Experiments

Uniaxial compression step cycle tests were carried out with HDPE (a HDPE-butene copolymer) and PHB. A Shimadzu AG50 deformation machine was used in combination with a Shimadzu TCL N220 thermostatic chamber and a video-extensometer Messphysik NG46 framing the diameter and the displacement of the compression cage. The samples were deformed with true strain rates of $\dot{\epsilon_t} = 4 \cdot 10^{-4}\, s^{-1}$ and for some cases $\dot{\epsilon_t} = 4 \cdot 10^{-3}\, s^{-1}$ which is still in the quasi static regime. Extensive investigations of this kind have also been carried out for polypropylene, presented in Chapter 5.

### Differential scanning calorimetry

Differential scanning calorimetry (DSC) is a versatile tool for the characterisation of polymers. The principle is rather simple. It is a thermoanalytical technique in which the difference in the amount of heat required to increase the temperature of a sample and a reference is measured as a function of temperature. By maintaining the sample and the reference at the same temperature

and by measuring the differences in the energies to achieve this equality one can determine the heat absorbed by the sample. In most cases a linear heat program with a well defined heating/cooling rate is chosen. The quantities determined by DSC in polymeric materials are mainly the glass transition temperature $T_g$, the melting point $T_m$, and the heat of fusion $\Delta H$. With the knowledge of the heat of fusion $\Delta H^0$of the ideally crystalline material one can derive the crystalline and the amorphous volume fractions

Using the Gibbs-Thompson Equation the lamella thickness and even the lamella thickness distribution can be derived as shown in Figure 8.10 for the case of iPP (see Chapter 7 for a detailed discussion of this procedure).

**In-situ Deformation Experiments using Synchrotron Radiation**

MXPA measurements need a high-resolution diffractometry. The use of the high intensity of Synchrotron radiation is benefical in this respect for the following reasons

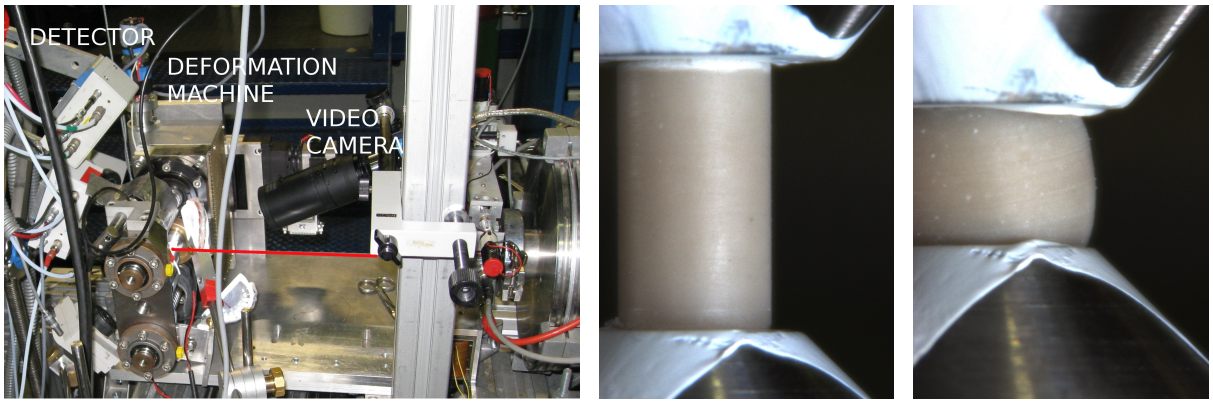


**(a)** Experimental Setup **(b)** PHB $\epsilon_t = 0$ **(c)** PHB $\epsilon_t = 0.65$

**Figure 8.1.:** (a) Experimental setup for in-situ deformation experiments at the beamline 5.2 L at ELETTRA in Trieste Italy. The red line indicates the path of the X-ray beam. Sample in the deformation machine (b) before and (c) after deformation.

- In cases of heavily deformed samples and/or inevitably large sample sizes, the intensities of laboratory X-ray generators are not sufficient in order to obtain the required high quality diffraction patterns.

- for the cases of in-situ experiments (i.e. MXPA, WAXS and SAXS measurements under load and during plastic deformation) which yield, in contrast to laboratory X-ray devices, data in much higher density with high resolution in space and time. Such experiments also allow for a direct correlation of microstructural changes under load with the in-situ monitored macroscopic hardening characteristics of the material and provide important input for the understanding and modelling of these characteristics. This is of special importance as relaxation in polymers is very fast due to the rubber-like properties of the material. In-situ experiments of other researchers during post yield deformation of

polymers have been mainly performed on PE so far [101, 102] but without any relation to the possible presence of dislocations.

In-situ deformation MXPA experiments were carried out at the SAXS-Beamline 5.2L of Sincrotrone ELETTRA Trieste. The usage of a specially designed miniature compression machine, in combination with high resolution linear detectors (1024 channels, type PSD 50 of Braun, Munich, Germany) and synchrotron radiation allowed for the accumulation of high quality diffraction patterns in exposure-times from 10 minutes to one hour. The experimental setup is depicted in Figure 8.1a. To ensure sufficient statistics for a reliable evaluation of the WAXS profiles, at least $10^4$ counts were collected in the maxima of the diffraction peaks. The X-ray beam was carefully positioned on the sample with a video camera and a movable stage on which the compression machine was mounted. Figures 8.1b and 8.1c show the sample before and after deformation in the compression machine as framed by the camera.

The results of in-situ deformation experiments are discussed in Chapters 6 (PHB and iPP) and 7 (iPP).

**Rolling of PHB**

As in-situ MXPA experiments in uniaxial compression delivered no increase in the dislocation density the question was raised whether this behaviour was related to the experimental setup. A different deformation mode was therefore required, and rolling was the method of choice.

For this purpose several discs of the purchased PHB were prepared with 15 mm diameter and a thickness of about 3 mm and subsequently deformed to different degrees by rolling. An overview of the samples can be found in Table 8.1. The experiments carried out on the rolled samples included DSC, SEM, and MXPA.

**Table 8.1.:** Overview of rolling samples of PHB with initial heights $h_0$ and heights after rolling $h$ as well as the calculated strains $\epsilon$.

| Sample No. | $h_0$ (mm) | $h$ (mm) | $\epsilon$ |
|---|---|---|---|
| PHBwb1 | 3.153 | 2.836 | 0.14 |
| PHBwb2 | 3.080 | 2.545 | 0.17 |
| PHBwb3 | 3.159 | 1.780 | 0.43 |
| PHBwb4 | 3.099 | 1.163 | 0.62 |
| PHBwb5 | 3.096 | 0.785 | 0.74 |

**Scanning Electron Microscopy**

The electron microscope used was the newly installed *Zeiss Supra 55 VP* at the *Faculty Center for Nanostructure Research* of the Faculty of Physics of the University of Vienna. The rolled samples presented in Section 8.2 were sputtered with a gold layer for 3 min before SEM investigation.

## 8.3. Results and Discussion

### 8.3.1. Cycling Experiments

As high density polyethylene (HDPE) can be considered as a model material for plasticity in semicrystalline polymers mechanical investigations were performed with a HDPE-butene copolymer. For this HDPE material the same sample preparation as for polypropylene (Chapter 5) was performed in order to assure a uniform spherulithic size distribution. Cyclic step cycle tests were carried out in compression with a strain rate of $\dot{\epsilon}_t = 4 \cdot 10^{-4}\, s^{-1}$ at room temperature.

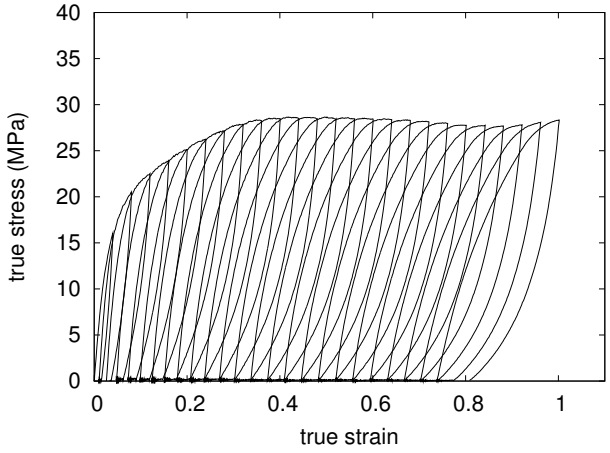


**Figure 8.2.:** True stress-true strain plot of the loading unloading experiment carried out on HDPE.

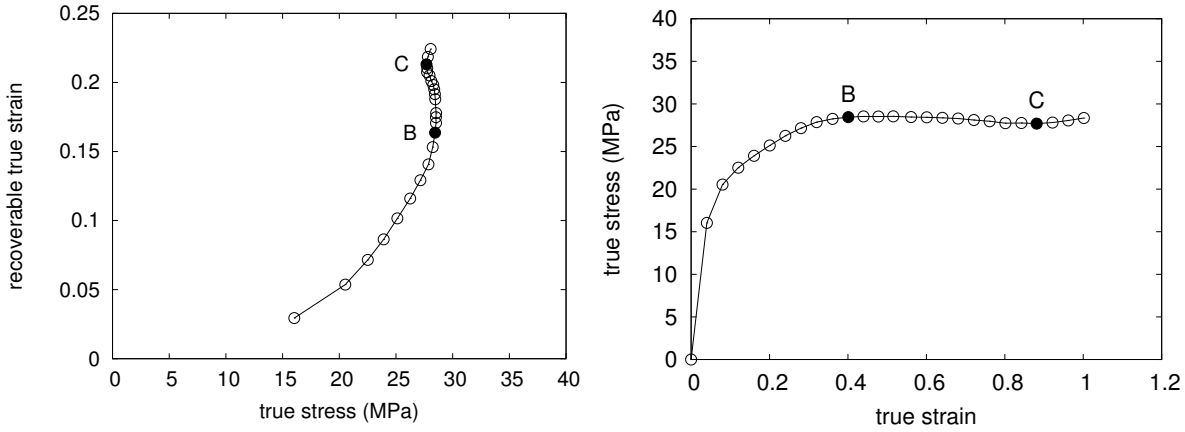


**(a)** Recoverable strains **(b)** Envelope of the stress strain curve

**Figure 8.3.:** (a) Recoverable strains as a function of the stress of HDPE for the determination of the critical strains B and C, and (b) the representation of points B and C in the context of the deformation curve.

In contrast to polypropylene for instance the stress-strain curve of HDPE shows two distinct yield points. In the nomenclature of Hiss et al. [10] the first one corresponds to transition point A while the second one corresponds to transition point B. This phenomenon of two yield points

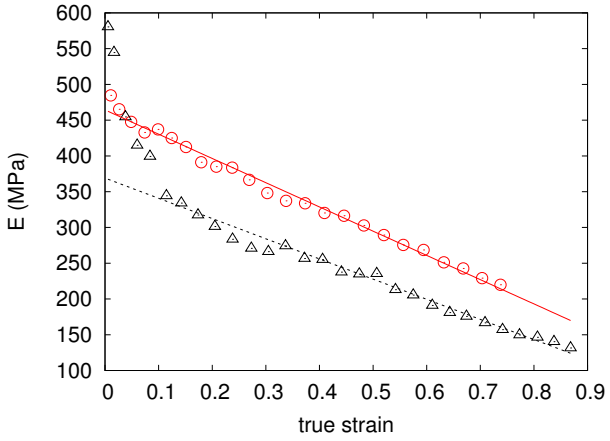


**Figure 8.4.:** Evolution of the Youngs modulus as a function of the applied true strain for HDPE (○) deformed at room temperature(21°C) and iPP (△) deformed at 50 °C[S2].

is not observed for iPP and PHB. Therefore only points B and C have been determined and discussed in this work in general.

The softening observed in the compression experiments is smaller in the case of HDPE as in iPP (Figure 8.2). The glass transition in polyethylene is much lower (-130°C to -70°C) than in polypropylene (0 °C). Therefore one can expect that the amorphous phase is softer in the case of room temperature experiments and that the stress-strain curve will on the one hand be governed by the stiffness of the crystalline phase and on the other hand the network properties of the amorphous phase. The latter can be studied by the procedure of the cyclic step cycle test allowing for the separation of the total applied strain into a residual and a recoverable part (Chapter 5). This separation is shown in Figure 8.3. The behaviour is similar to the behaviour of polypropylene.

Also the evolution of the elastic modulus as a function of the deformation depicted in Figure 8.4 shows a linear decrease similar to the drop in polypropylene. However, slight differences can be found in the evolution of the energy absorbed per deformation cycle determined from the strain energy. In Figure 8.5 the evolution in HDPE is compared to the energy absorbed by iPP at a deformation temperature of 50°C which corresponds better to the relative deformation temperature with respect to $T_m$ and $T_g$ than the room temperature experiment of iPP. While in polypropylene the absorbed energy saturates only for the case of deformation below the glass transition temperature, polyethylene seems to saturate already at room temperature and does even show a small reduction for true strains bigger than $\epsilon_t = 0.8$. Following the argumentation of Chapter 5 the saturation is related to the suppression of possible energy consuming processes.

Poly(3-hydroxbuthyrate) (PHB) was chosen as an additional model material within this thesis as it is suitable for the investigation with MXPA. It has a high phase purity and shows a sufficient number of Bragg reflections (Figure 8.16). In contrast to HDPE and iPP the material was not subjected to a heat treatment due to its thermal instability. From the extruded rods purchased from Goodfellow Inc. cylindrical samples with 10 mm height and a diameter of 6 mm were

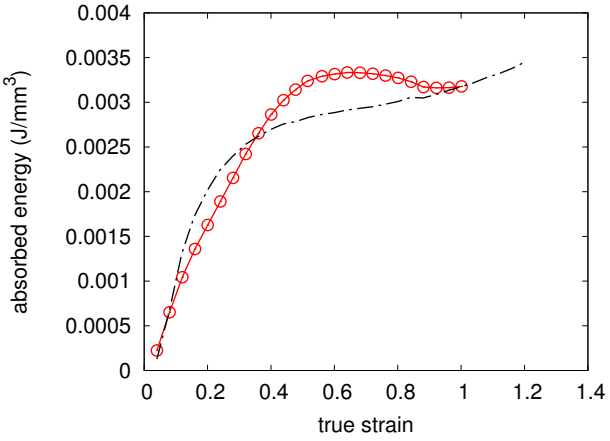


**Figure 8.5.:** Strain energy absorbed per cycle by HDPE (∘) deformed at room temperature (21°C) as a function of the true strain. The dash-dotted line indicates the energy absorbed by iPP at a deformation temperature of 50°C[S2].

machined and subjected to compressive step cycle tests.

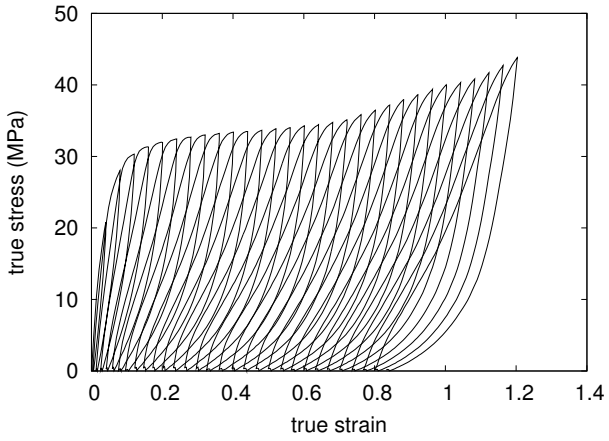


**Figure 8.6.:** True stress-true strain plot of the loading unloading experiment carried out on PHB.

In contrast to iPP and HDPE many samples show strong whitening on the sample surface with higher deformation, leading to large cracks and even complete failure for a considerable number of samples. Here we present data of a sample that did not fail, but deformed rather homogeneously. It is noted that this cannot be considered as the general case but as we are interested in the microstructural processes mainly, the macroscopic failure is not discussed in depth here. Interestingly no softening is found in PHB after the yield point which might be related to some degree to the closeness to the glass transition temperature of about 15°C(Figure 8.6).

From Figure 8.7 we get even stronger evidence that the micromechanical processes of PHB differ considerably from the other investigated polymers. The residual strain remains very small until transition point B is reached. Until this point most of the deformation is recoverable suggesting that deformation is mostly located in the amorphous network. The most striking

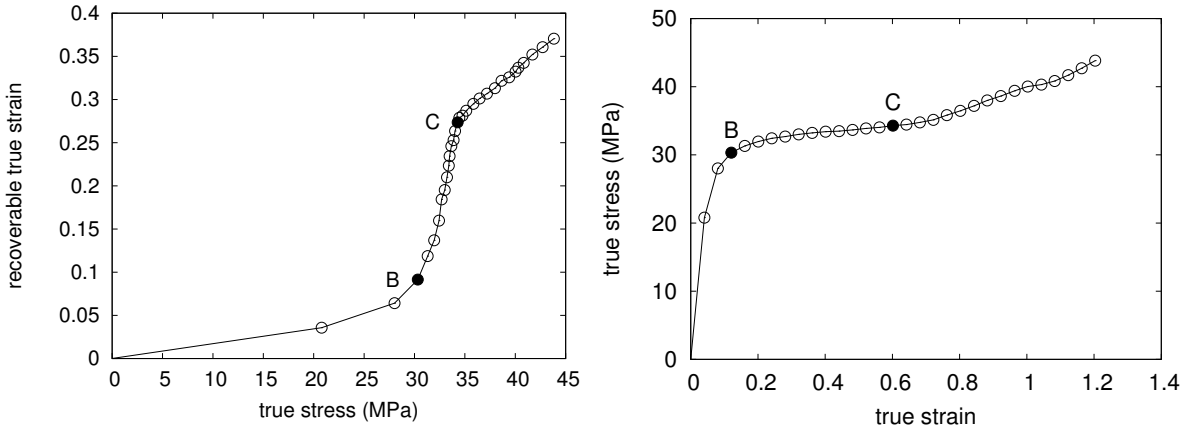


**(a)** Recoverable strains **(b)** Envelope of the stress strain curve

**Figure 8.7.:** (a) Recoverable strains as a function of the stress of PHB for the determination of the critical strains B and C, and (b) the representation of points B and C within the deformation curve.

difference lies in the way the elastic modulus evolves with each deformation cycle. In HDPE and iPP the elastic modulus is reduced in a linear manner probably related to the increase in the amorphous volume and due to texture effects. In PHB the elastic resistance breaks down after only a few cycles (Figure 8.8). In contrast to iPP where a monotonous decrease is found after the first lamellar reorientation in PHB the final value for $E$ is already reached around transition point B. This is a very strong indication that the stiffness of the crystalline phase is not properly submitted to the matrix and the whole composite. The continuous need for the formation of crazes or microcracks due to localised tensile stresses could be an explanation not only for the drop of the Young's modulus but also for the evolution of the absorbed energy as a function of the deformation shown in Figure 8.9.

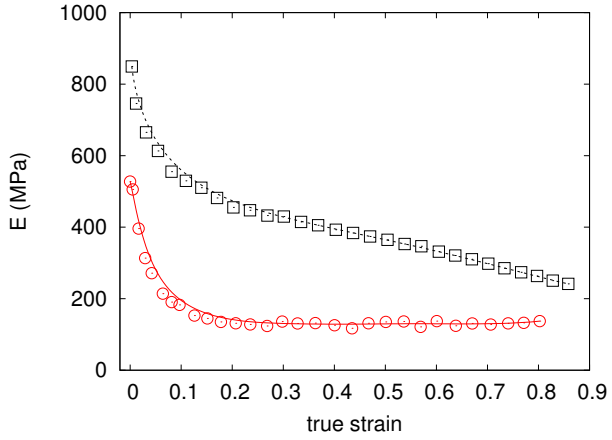


**Figure 8.8.:** Evolution of the Youngs modulus as a function of the applied true strain in PHB (○) and iPP (□) deformed at room temperature [S2].

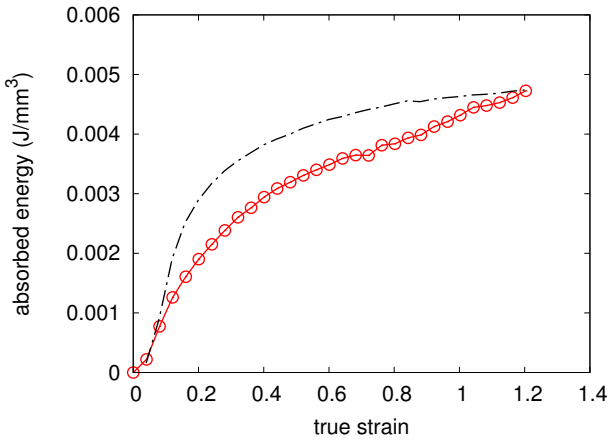


**Figure 8.9.:** Absorption of energy per cycle by the PHB sample as a function of the true strain in PHB (∘). The dash dotted line indicates the energy absorbed by iPP deformed at room temperature [S2].

### 8.3.2. Differential Scanning Calorimetry

Differential scanning calorimetry was used to determine the evolution of the lamella thickness distribution in iPP during deformation. The procedure used is described in Chapter 5. The observation that the lamella thickness is not much affected by the plastic deformation is in good agreement with the MXPA results ([3] and [S4], see also Chapter 9).

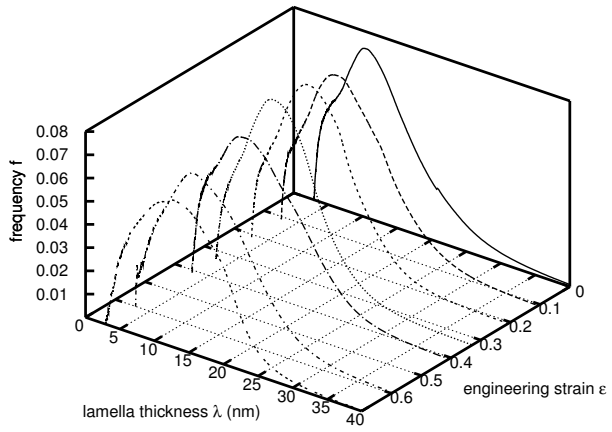


**Figure 8.10.:** Lamella size evolution in iPP upon plastic deformation (uniaxial compression) as determined by DSC

The DSC-curve of polyhydroxybuthyrate shows two distinct peaks (Figure 8.11). When calculating the corresponding lamella thicknesses these two peaks can be attributed to a primary thickness of about 7nm and a secondary thickness with only 1.4 nmcorresponding to primary and secondary crystallisation respectively [103].

Upon deformation the secondary peak corresponding to the small thickness gets smaller with respect to the primary one which broadens. The change of the lamella thickness distribution of PHB with plastic deformation is shown in Figure 8.12. Although some changes in the relative

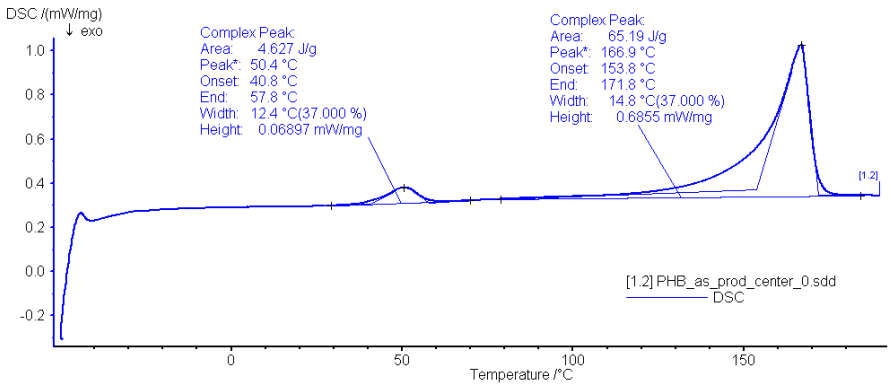


**Figure 8.11.:** DSC measurement of undeformed PHB showing two melting peaks.

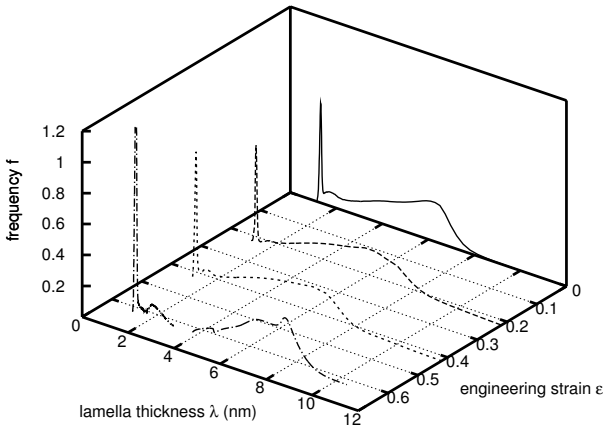


**Figure 8.12.:** Lamella size evolution in PHB upon plastic deformation (uniaxial compression) as determined by DSC

frequencies of the primary and the secondary thickness can be seen the effect can be considered as rather weak. The bimodal thickness distribution might be one of the parameters causing the brittleness of the material because interlamellar crystallisation could reduce chain mobility in the amorphous regions.

### 8.3.3. Electron Microscopy of Polyhydroxybutyrate

In order to gain more information on the processes occurring in the deformation of PHB scanning electron microscopy (SEM) was carried out. The open questions concerned mainly

(a) the reasons for the constant dislocation density as a function of the plastic deformation of PHB described in Chapter 6 and

(b) the reasons for the remarked brittleness although a considerable initial dislocation density is found.

Already the undeformed sample shows that the material is full of small cracks with only a few nanometres in size but no crazes are visible (Figure 8.13). The small cracks might to some

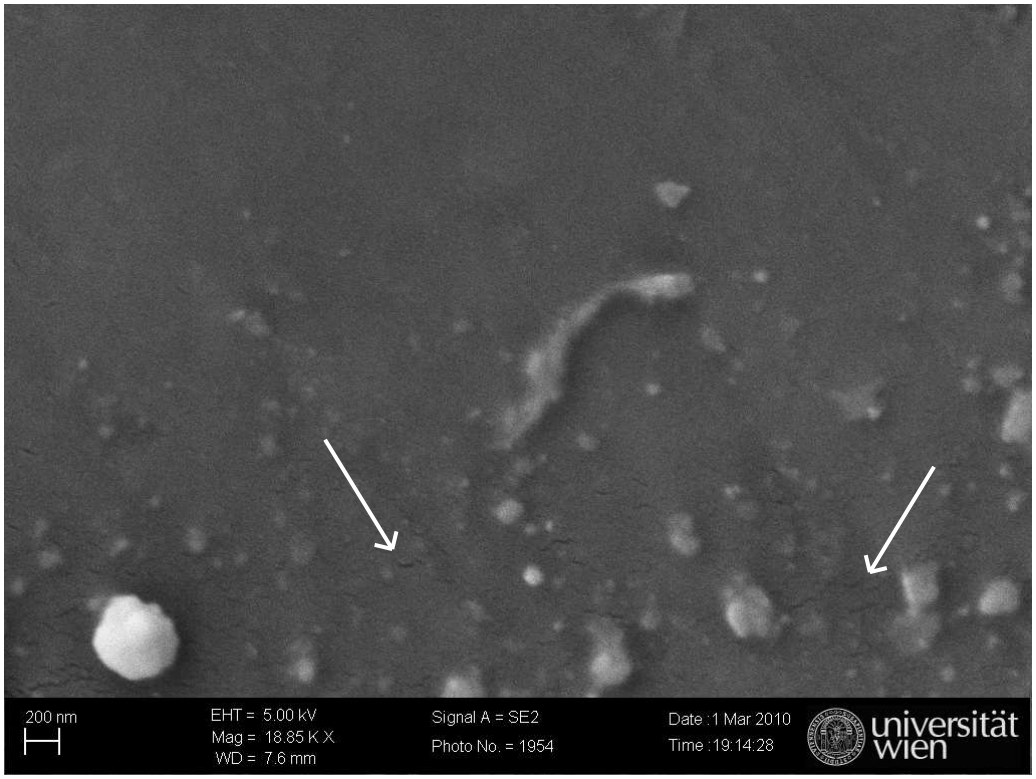


**Figure 8.13.:** SEM micrograph of undeformed PHB. Already here several micro- and nano-cracks are visible.

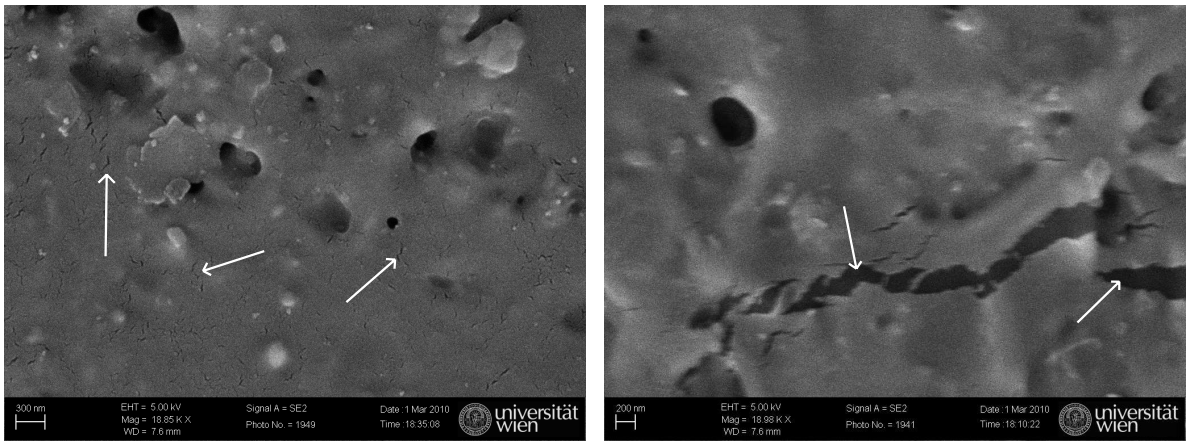


**(a)** PHBwb1 **(b)** PHBwb3

**Figure 8.14.:** (a) SEM micrograph of PHBwb1 with a strain of 0.14. The cracks seem to have grown slightly. (b) SEM micrograph of PHBwb3 deformed up to a strain of 0.43. This sample showed a number of singular but larger cracks.

part be related to cracks in the coating without any failure of the polymer matrix. Rolling as deformation mode with negative pressure should in a ductile material not cause a growth of these cracks. With increasing deformation, however, the size of the cracks increases as can be

seen in Figure 8.14a and even more strikingly in Figure 8.14b. In sample PHBb4, which has been deformed up to a nominal strain of 0.62, the number of cracks is considerably increased locally (Figure 8.15a) while other areas remain rather unaffected (Figure 8.15a).

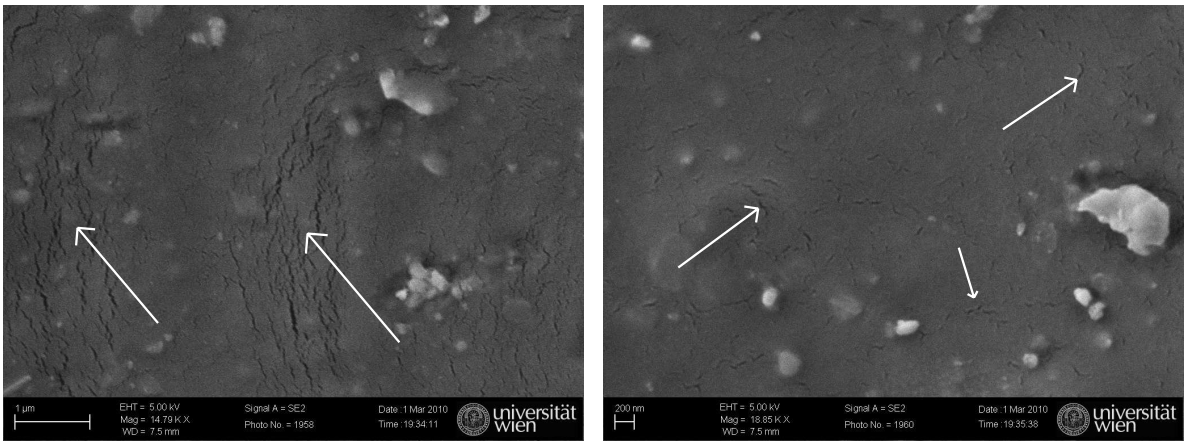


**(a)** PHBwb4 **(b)** PHBwb4

**Figure 8.15.:** SEM micrographs of PHBwb4 deformed up to a strain of 0.62. Regions with a large number of larger cracks (a) and regions with smaller singular cracks (b) are found.

In general the SEM investigations confirm the assumption that deformation occurs by interlamellar processes because of the high strength of the crystalline areas. The brittleness and the occurrence of micro- and nano-cracks additionally suggests that the ductility of the amorphous-crystalline composite is quickly exhausted due to the concentration of the deformation processes in the amorphous phase.

### 8.3.4. X-Ray Line Profile Analysis of Rolled PHB

X-ray line profile analysis was carried out on the samples of rolled PHB (Table 8.1). For these experiments the incident beam had a spot size of 100 µm× 200 µm on the sample and the photon flux amounted to $5 \cdot 10^{11}$ photons $\mathrm{mm}^{-2}\mathrm{s}^{-1}$.

Figure 8.16 reproduces the diffractogrammes recorded in situ during a uniaxial compression experiment. Similarly to the profile of the measured after rolling no relevant broadening was observed. The recorded profiles were subjected to an evaluation procedure similar to the ones described in Chapters 6 and 7. In accordance with the results presented in Chapter 6 no significant increase of the dislocation density is found in rolling as shown in Figure 8.17. Even for much larger deformations than the ones achieved in uniaxial compression no increase of dislocation density is found. This together with the SEM and DSC experiments of PHB presented in this chapter suggests that the formation of microcracks is an important deformation mechanism of the crystalline phase.

The values for the lamella sizes determined by MXPA scatter much more in the case of PHB than in the case of $\alpha$-iPP. They lie in the order of 5-12 nm also for the rolled case. The size distribution for an undeformed sample is represented in Figure 8.18 in comparison with the size

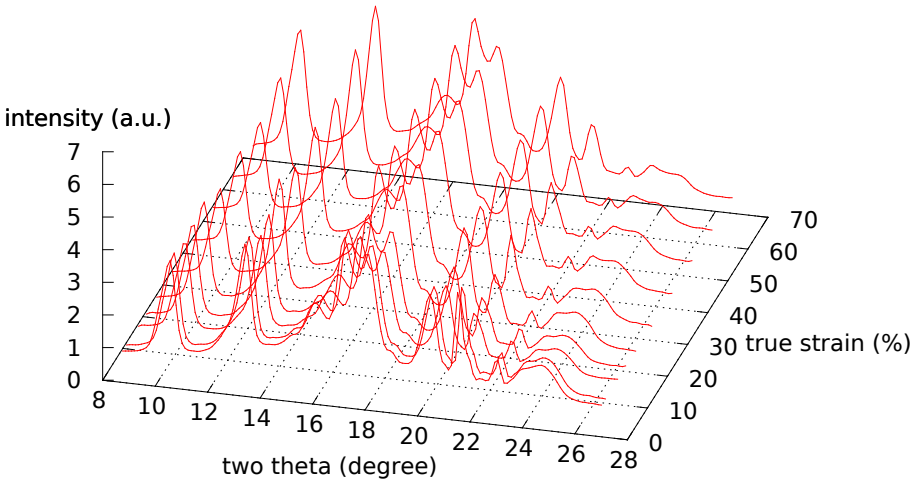


**Figure 8.16.:** Evolution of the diffraction pattern of PHB as a function of the plastic deformation (compression).

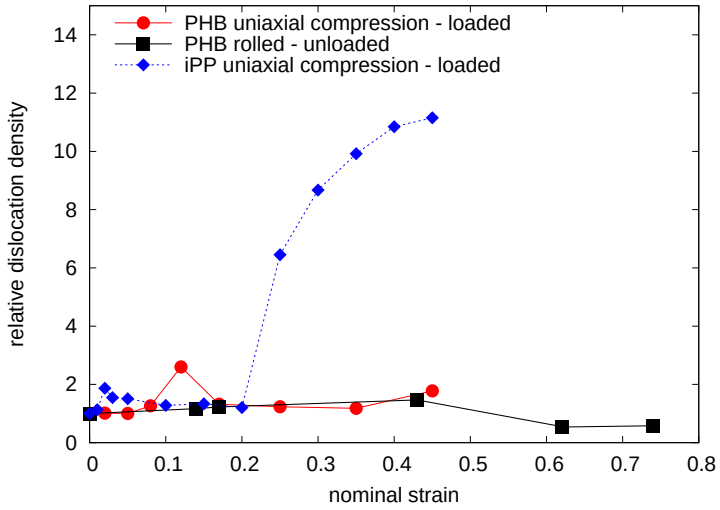


**Figure 8.17.:** Relative evolution of the dislocation density as a function of the strain for rolled and uniaxially compressed PHB compared to the evolution in $\alpha$-iPP.

determined by DSC. Considering the fact that the size distribution from the DSC experiment is far from monomodal the agreement is very satisfactory.

## 8.4. Conclusions

In this chapter a number of experiments were presented leading to a differentiated view of the plastic deformation of semicrystalline polymers. Indeed the results of the mechanical experiments carried out in iPP and HDPE are in accordance with the dislocation concept. On the other hand PHB does not fit into this picture. The marked brittleness seems to be related to the high stiffness of the crystalline phase resulting in a number of small cracks observed by SEM. The constant dislocation density as a function of the strain is thus a consequence of the inability

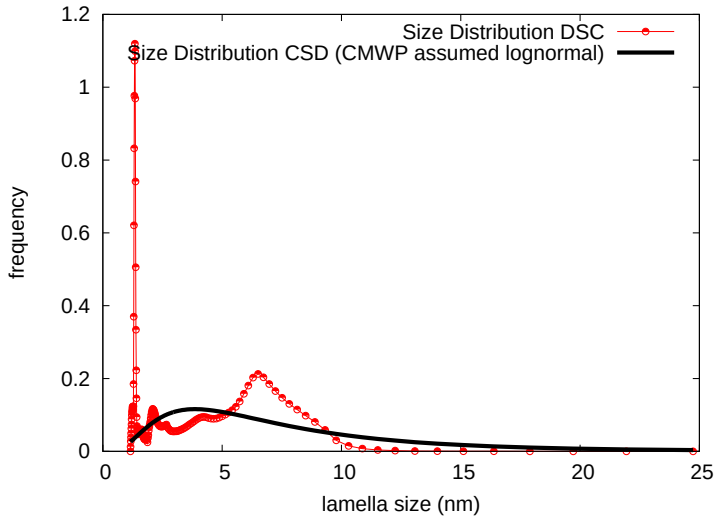


**Figure 8.18.:** Comparison of the size distribution as determined via DSC and via CMWP.

of the crystallites to deform plastically. A somewhat similar behaviour has been observed in $\gamma$-phase iPP [104, 105] with only one potential slip system. Here the stiffness of the crystallites leads to shear banding rather than microcracking.

Therefore we have to accept that the intrinsic deformation mechanisms in the crystalline phase differ quite strongly for different types of semicrystalline polymers and that a number of processes can occur, including dislocation motion as for the case of polyethylene and polypropylene. The size of the crystallite, the chemical bonding in the crystallites, the structure of the amorphous matrix and of course the chain segment mobility are only some of the parameters that could potentially favour one process among the others. The occurrence of dislocation governed crystalline slip, however, can be considered as an important reason for the good ductility in a number of crystallising polymers. Future XPA investigations could be a reasonable tool for a closer analysis and identification of such polymers.

# 9. Calculation of the Dislocation Contrast Factor of iPP

## 9.1. Dislocation Contrast Factor

The dislocation contrast factor is a parameter in the formulation of the mean square strain related to the effect of strain anisotropy of dislocations (Figure 9.1). Numerical calculations of the contrast factor have been carried out mainly for cubic and hexagonal materials [61, 106, 107]. Due to the different character of the present dislocations in terms of their strain field (represented by the contrast factor) their Burgers vector and their number, appropriate averaging has to be applied.

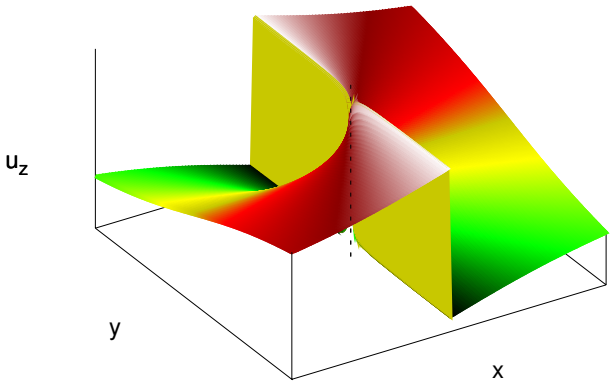


**Figure 9.1.:** Schematic representation of the component $u_z$ of the displacement field of a screw dislocation. The dislocation line is represented with dashes.

Martinez-Garcia et al. [66] suggested a general route for the calculation of the average dislocation contrast factor based on the Stroh [108] formalism. A very comprehensive discussion of Stroh's formalism is presented in the book "Anisotropic Elasticity" by Ting [48]. The approach of Martinez-Garcia not only allows for a general treatment of arbitrary crystal symmetries but also yields a path towards analytical solutions for the dislocation contrast factor for selected slip systems. This was demonstrated for several hexagonal and also monoclinic materials.

Therefore this approach was chosen in order to determine the contrast factor in $\alpha$-iPP for straight dislocations. An evaluation script has been developed for the high level language GNU Octave (`http://www.octave.org` [99]). The script can be found in Appendix A.1

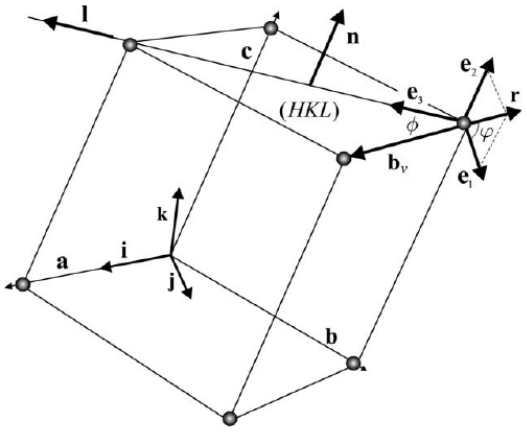


**Figure 9.2.:** Unit cell of a general crystal with a straight dislocation. The axes of the references $C\{\mathbf{a},\mathbf{b},\mathbf{c}\}$ and $S\{\mathbf{e}_1,\mathbf{e}_2,\mathbf{e}_3\}$ are represented as well as the axes of the orthogonal system $O\{\mathbf{i},\mathbf{j},\mathbf{k}\}$ (from [66]).

## 9.2. Mathematical Background

In order to draw a complete picture of the mathematical background and to assure a comprehensive mathematical nomenclature of the procedure the most important steps discussed by Martinez-Garcia et al. [66] will be reproduced in this section. The better informed reader may skip this section and directly proceed to the next section dealing with the numerical results of the contrast factor calculation in isotactic polypropylene.

The first step in the calculation requires the reduction of the problem from three dimensions to a state of two dimensional strain. This goal is achieved by transformation from the monoclinic crystal lattice coordinate system $C\{\mathbf{a},\mathbf{b},\mathbf{c}\}$ to a system related to the slip system of the dislocation $S\{\mathbf{e}_1,\mathbf{e}_2,\mathbf{e}_3\}$. The unit vectors of this system are chosen in such a way that $\mathbf{e}_2 = \mathbf{n}/n$ where $\mathbf{n}$ is the slip plane normal, $\mathbf{e}_3 = \mathbf{l}$ with the dislocation line vector $\mathbf{l}$, and $\mathbf{e}_1 = \mathbf{e}_2 \times \mathbf{e}_3$. The angle $\phi$ denotes the angle between the Burgers vector $\mathbf{b}_v$ of the dislocation and the dislocation line $\mathbf{l}$ and characterises the dislocation as edge ($\phi = 90°$) or screw ($\phi = 0°$) type.

A common orthonormal frame $O\{\mathbf{i},\mathbf{j},\mathbf{k}\}$ is chosen in such a manner that $\mathbf{i} = \mathbf{a}/a$, $\mathbf{j} = \mathbf{k}\times\mathbf{i}$ and $\mathbf{k} = \mathbf{c}^*/c^*$ where the * denotes reciprocal lattice quantities. A scheme of the three coordinate systems and other relevant quantities is represented in Fig. 9.2.

The dislocation which is the cause of the strain field is characterised by the slip plane normal $\mathbf{n} = H\mathbf{a}^* + K\mathbf{c}^* + L\mathbf{c}^*$ with the coordinates $[H,K,L]$ in the reciprocal basis $[\mathbf{a}^*,\mathbf{b}^*,\mathbf{c}^*]^T$ [1], the Burgers vector $\mathbf{b}_v$ with (real) lattice coordinates [U,V,W] and the dislocation character given by the angle $\phi$.

The representation of the unit vectors of the crystal lattice in terms of the orthonormal frame

[1] The corresponding slip plane has the Miller indices (HKL)

read as

$$\begin{bmatrix} \mathbf{i} \\ \mathbf{j} \\ \mathbf{k} \end{bmatrix} = M \begin{bmatrix} \mathbf{a} \\ \mathbf{b} \\ \mathbf{c} \end{bmatrix}. \tag{9.1}$$

with the matrix

$$M = \begin{bmatrix} \frac{1}{a} & 0 & 0 \\ \frac{-\cos\gamma}{a\sin\gamma} & \frac{1}{b\sin\gamma} & 0 \\ a^*\cos\beta^* & b^*\cos\alpha^* & c^* \end{bmatrix}. \tag{9.2}$$

M is related to the metric tensor of the crystal lattice $G_m$ by the relation $G_m = M^{-1}(M^{-1})^T$. $G_m$ is given by

$$G_m = \begin{bmatrix} a^2 & ab\cos\gamma & ac\cos\beta \\ ab\cos\gamma & b^2 & bc\cos\alpha \\ ac\cos\beta & bc\cos\alpha & c^2 \end{bmatrix}, \tag{9.3}$$

and $G_m^* = G_m^{-1}$ is the metric tensor of the reciprocal lattice.

The unit vectors of the slip system frame can be written in terms of the orthonormal frame as

$$\begin{bmatrix} \mathbf{e_1} \\ \mathbf{e_2} \\ \mathbf{e_3} \end{bmatrix} = P \begin{bmatrix} \mathbf{i} \\ \mathbf{j} \\ \mathbf{k} \end{bmatrix}, \tag{9.4}$$

and the transformation Matrix thus contains the coordinates of the unit vectors $e_1 \dots e_3$ in the orthonormal frame

$$P = \begin{bmatrix} \xi_1^1 & \xi_2^1 & \xi_3^1 \\ \xi_1^2 & \xi_2^2 & \xi_3^2 \\ \xi_1^3 & \xi_2^3 & \xi_3^3 \end{bmatrix}. \tag{9.5}$$

As $\mathbf{e}_2$ is chosen to be parallel with $\mathbf{n}$ the coordinates in $O$ are given by

$$\mathbf{e}_2 = \begin{bmatrix} \xi_1^2 \\ \xi_2^2 \\ \xi_3^2 \end{bmatrix} = \frac{1}{|\mathbf{n}|} M \begin{bmatrix} H \\ K \\ L \end{bmatrix}, \ |\mathbf{n}| = \sqrt{\mathbf{n} \cdot G_m^* \cdot \mathbf{n}^T} \tag{9.6}$$

For the determination of $\mathbf{e}_3$ the coordinates of the Burgers vector in O are determined by

$$\mathbf{b}_v = \begin{bmatrix} \xi_1^b \\ \xi_2^b \\ \xi_3^b \end{bmatrix} = \frac{1}{|\mathbf{b}_v|}(M^{-1})^T \begin{bmatrix} U \\ V \\ W \end{bmatrix}, \ |\mathbf{n}| = \sqrt{\mathbf{b}_v \cdot G_m \cdot \mathbf{b}_v^T} \tag{9.7}$$

and by subsequent rotation of $\mathbf{b}_v$ by the angle $\phi$ around $\mathbf{e}_2$, the orthonormal coordinates of $\mathbf{e}_3$ are found as

$$\mathbf{e}_3 = \begin{bmatrix} \xi_1^3 \\ \xi_2^3 \\ \xi_3^3 \end{bmatrix} = R(\phi, \mathbf{e}_2) \begin{bmatrix} \xi_1^b \\ \xi_2^b \\ \xi_3^b \end{bmatrix}. \tag{9.8}$$

Following the requirement that $\mathbf{e}_1$ is normal to the plane spanned by $\mathbf{e}_2$ and $\mathbf{e}_3$, it is given by the cross product of the two vectors

$$\mathbf{e}_1 = \mathbf{e}_2 \times \mathbf{e}_3. \tag{9.9}$$

### 9.2.1. Contrast Factor for the Given Slip System

The contrast factor $C_{hkl}$ of a reflection $(hkl)$ of a given slip system is derived by the product of the two fourth rank tensors $G_{ijmn}$ and $E_{ijmn}$ where $G_{ijmn}$ contains the geometric information and $E_{ijmn}$ the elastic information.

$$C_{hkl} = \sum_{i,m}^{3} \sum_{j,n}^{2} G_{ijmn} E_{ijmn}. \tag{9.10}$$

The tensor elements of $G_{ijmn}$ is given by the multiplication of the direction cosines $\tau_i = \mathbf{d}^*/d^* \cdot \mathbf{e}_i$ between the diffraction vector $d^*$ and the axes $\mathbf{e}_i$ of the coordinate system of the slip system S.

$$G_{ijmn} = \tau_i \tau_j \tau_m \tau_n \text{with} \qquad i, m = 1, 2, 3 \text{ and} \qquad j, n = 1, 2. \tag{9.11a}$$

$E_{ijmn}$ is related to the elastic properties of the crystal and is thus related to the displacement field of the dislocation. The components of $E_{ijmn}$ can be written as the integral

$$E_{ijmn} = \frac{1}{\pi} \int_0^{2\pi} \beta_{ij} \beta_{mn} \mathrm{d}\varphi \tag{9.12}$$

where the $\beta_{ij}$ are proportional to the partial derivatives $\partial u_i / \partial x_j$ of the displacement field of the dislocation, and $\varphi$ is the polar angle. Following the Stroh formalism [48] the displacement field $\mathbf{u}$ can be written in terms of the eigen solutions $p_\alpha$ and eigen vectors $(\mathbf{A}_\alpha, \mathbf{L}_\alpha)$ of the corresponding

eigenvalue problem related to the fundamental elasticity matrix $N^2$.

$$N \begin{bmatrix} \mathbf{A}_\alpha \\ \mathbf{L}_\alpha \end{bmatrix} = p_\alpha \begin{bmatrix} \mathbf{A}_\alpha \\ \mathbf{L}_\alpha \end{bmatrix} \tag{9.13}$$

The $m$th component of $\mathbf{u}$ in slip system coordinates is given by

$$u_m(x_1, x_2) = \frac{b_v}{2\pi} \mathrm{Im} \left[ \sum_{\alpha=1}^{3} A_{m\alpha} D_\alpha \ln\left(x_1 + p_\alpha x_2\right) \right], \tag{9.14}$$

with

$$D_\alpha = -\frac{\mathbf{A}_\alpha \cdot \mathbf{b_v}}{b_v(\mathbf{A}_\alpha \cdot \mathbf{L}_\alpha)} \tag{9.15}$$

In terms of the polar angle $\varphi$ and the eigensolutions $p_\alpha$ and the corresponding eigenvectors $(\mathbf{A}_\alpha, \mathbf{L}_\alpha)$ it is found that [66]

$$\beta_{mn}(\varphi) = \mathrm{Im} \sum_{\alpha=1}^{3} \left[ \frac{A_{m\alpha} D_\alpha p_\alpha^{(n-1)}}{\cos(\varphi) + p_\alpha \sin(\varphi)} \right] \tag{9.16}$$

Using equations 9.12 and 9.16 we can calculate the components of $E_{ijmn}$ and subsequently the contrastfactor $C_{hkl}$ by use of equation 9.10.

### 9.2.2. Average Contrast Factor

For the case of polycrystalline materials with random orientation of the grains and equal population of the $N$ crystallographically equivalent slip systems the average contrast factor is calculated by

$$\bar{C}_{hkl} = \frac{1}{N} \sum_{i}^{N} C_{hkl}^{i}. \tag{9.17}$$

For arbitrary populations of the slip systems, weights can be included in this formulation in order to account for the relative populations of the slip systems.

At this place it has to be noted that the dislocation contrast factor does not include possible influences of crystallographic texture, dislocation arrangements as e.g. dipoles and influences of the crystal size on the dislocation strain field.

## 9.3. Application to iPP

Using the algorithm described in the last section a numerical calculation of the contrast factor of the crystallographic $\alpha$ phase of polypropylene has been carried out using an octave script developed for this purpose (see Appendix A.1). The values were calculated for the four slip

[2] The $6 \times 6$ fundamental elasticity matrix $N$ basically contains the components of the elastic stiffness tensor $C_{pqrs}$. A derivation can be found in the book of Ting [48]

**Table 9.1.:** Numerical contrast factor of screw ($\odot$) dislocations in $\alpha$-iPP.

| Reflection | $2\Theta$ (°) | $C_{(010)[001]\odot}$ | $C_{(100)[001]\odot}$ | $C_{(110)[001]\odot}$ | $C_{(010)[100]\odot}$ |
|---|---|---|---|---|---|
| [110] | 14.1 | 0.0104 | 0.0104 | 0.0104 | 0.1020 |
| [040] | 16.9 | 0.0055 | 0.0055 | 0.0055 | 0.0006 |
| [130] | 18.6 | 0.0031 | 0.0031 | 0.0031 | 0.2556 |
| [111] | 21.3 | 0.2236 | 0.2236 | 0.2236 | 0.2385 |
| [13$\bar{1}$] | 21.8 | 0.2353 | 0.2353 | 0.2353 | 0.2287 |
| [041] | 21.9 | 0.2221 | 0.2221 | 0.2221 | 0.0004 |

systems of the monoclinic lattice stated in the literature [109, 110, 39, 111]. These slip systems can be separated into the three systems with chain slip (010)[001], (100)[001], (110)[001] and into one system with transverse slip (010)[100]. Edge and screw character of the dislocations was assumed to be present for all of the four dislocation types and the corresponding contrast factor values were calculated.

The monoclinic $\alpha$-phase of iPP has the space group $P2_1/c$ [112] with unit cell parameters $a = 6.65$ Å, $b = 20.96$ Å, $c = 6.50$ Å, and $\beta = 99.33°$. Theoretically determined values for the elastic stiffness of the $\alpha$-phase of iPP can be found in Tashiro et al. [112] The elastic stiffness matrix $C_\alpha$ (in the orthonormal frame) is given by

$$C_\alpha = \begin{bmatrix} 7.78 & 3.91 & 3.72 & 0 & 0.9 & 0 \\ 3.91 & 11.55 & 3.99 & 0 & -0.36 & 0 \\ 3.72 & 3.99 & 42.44 & 0 & -0.57 & 0 \\ 0 & 0 & 0 & 4.02 & 0 & -0.12 \\ 0.9 & -0.36 & -0.57 & 0 & 3.1 & 0 \\ 0 & 0 & 0 & -0.12 & 0 & 2.99 \end{bmatrix} \text{GPa} \tag{9.18}$$

with the $z$-direction perpendicular to the (001) plane and thus almost parallel to the crystallographic $c$-direction [3]. The value of 42.44 GPa in this direction is in good agreement with the high stiffness observed in X-ray experiments [113].

The results of the numerical calculation of the contrast factor are given in Tables 9.1 and 9.2 for the most important reflections of $\alpha$-iPP. It can be seen that the chain slip dislocations are equivalent for the screw case but have a different contrast factor for the edge dislocations. The (130) reflection shows considerable differences in the contrast for transverse and chain slip (both edge and screw case). These two observations are interesting as they indicate that it should be possible to quantify the relative content of each dislocation type – screw and edge on the one hand and chain and transverse on the other – by comparison with experimental X-ray line broadening data.

[3] Other reported symmetries include $C2/c$ and $Cc$ [112] related to the chirality of the helix of the molecular chain.

**Table 9.2.:** Numerical contrast factor of of edge ($\perp$) dislocations in $\alpha$-iPP.

| Reflection | $2\Theta$ (°) | $C_{(010)[001]\perp}$ | $C_{(100)[001]\perp}$ | $C_{(110)[001]\perp}$ | $C_{(010)[100]\perp}$ |
|---|---|---|---|---|---|
| [110] | 14.1 | 0.0027 | 0.1226 | 0.1435 | 0.5265 |
| [040] | 16.9 | 0.1300 | 0 | 0.0029 | 0.0997 |
| [130] | 18.6 | 0.0338 | 0.0417 | 0.0998 | 0.3210 |
| [111] | 21.3 | 0.0855 | 0.5201 | 0.5665 | 0.0984 |
| [13$\bar{1}$] | 21.8 | 0.2911 | 0.3995 | 0.5535 | 0.1605 |
| [041] | 21.9 | 0.5662 | 0.0408 | 0.1124 | 0.0372 |

### 9.3.1. Evaluation of Dislocation Types

For this purpose data previously evaluated [3, S3, S4, 89] for the Williamson and Hall method [94], were used to dreive the full width at half mean (FWHM) for each reflection.

WAXS measurements were performed in transmission setup at the SAXS-Beamline 5.2L of the synchrotron ELETTRA (Trieste, Italy). After recording the profile at the undeformed state, the sample was deformed in small steps up to a true strain of $\epsilon_t = 0.55$ using a miniature compression machine allowing for in-situ deformations. Several profiles were recorded over the whole deformation range. The data were collected after the sample was unloaded at the specified strain in accordance with the cyclic experiments described in Section 8.3.1. More experimental details concerning the X-ray diffraction can be found in chapter 7.

In the procedure used so far to determine an experimental contrast factor for $\alpha$-iPP, a linearisation in the modified Williamson-Hall plot was achieved by application of the fourth order invariants of the (hkl)-indices. As the number of contrast related fit parameters would be as high as eight for the monoclinic case, an orthorhombic structure was assumed as approximation [3] (only five parameters $a_1 \ldots a_5$ for the contrast factor). The more exact approach presented here allows to apply the fully monoclinic model while reducing the number of fit parameters by the low number of present slip systems. The total of 8 parameters, one for each slip system, is needed . As the screw dislocations with the Burgers vector in chain direction are equivalent in terms of the contrast factor, this number can be reduced to 6. This compares to 5 in the orthorhombic approximation.

For each profile the modified Williamson-Hall plot is linearised with a contrast factor calculated from weighted single slip system contrast factors, each of the weights being one fit parameter. With the dislocation density and the coherently scattering domain (CSD) size the total number of fitting parameters amounts to eight. In order to improve the quality of the fits, the CSD size is restricted to values smaller than 25 nm.

The resultant evolution of the CSD size and the dislocation density as a function of the strain are represented in Figure 9.3. In agreement with the earlier investigations [3, S4] the dislocation density is considerably increased while only small changes in the domain size are observed.

The other six fit parameters are the relative populations of the six slip systems. Figure 9.4 represents the evolution of the screw and edge dislocations as determined by the fitting of the FWHM data. Before deformation starts the overwhelming part of the dislocations present in

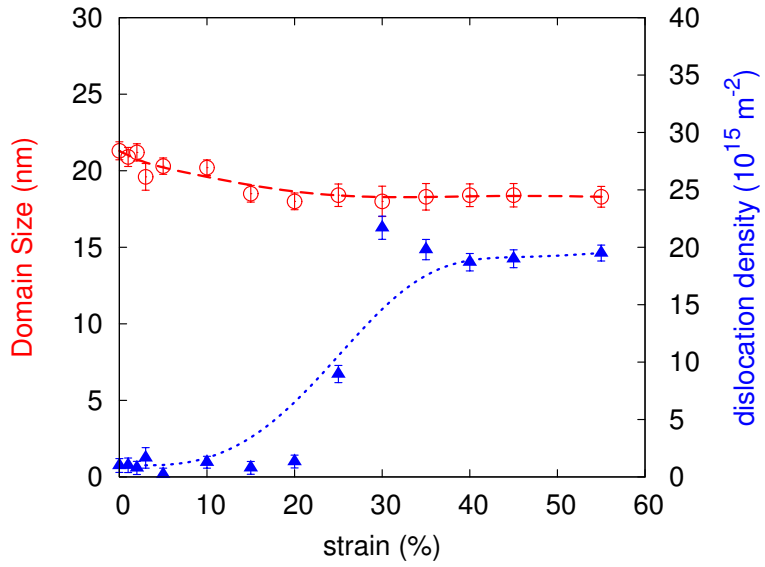


**Figure 9.3.:** Domain size (○) and dislocation density (▲) as a function of the applied strain.

the material have screw character. With increasing deformation a small reduction in the screw fraction is observed. From about 20 % true strain a significant number of edge dislocations is generated saturating at about 25 % of the total dislocations.

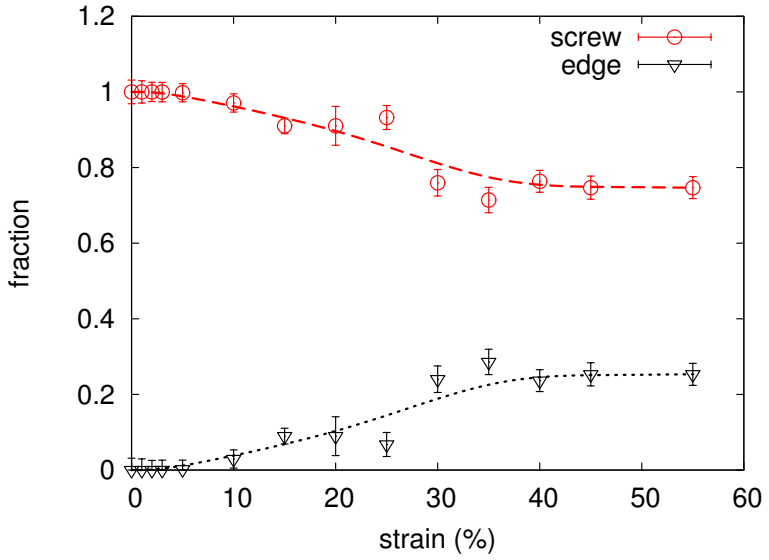


**Figure 9.4.:** Fraction of screw (○) and edge dislocations (▽) as a function of the applied strain.

The other important property of the slip systems is their orientation and slip direction with respect to the chain axis. The evaluation of the fraction of the chain-slip and transverse-slip type dislocations is represented in Figure 9.6. Here a very fast transition from pure chain-slip dislocations towards mostly transverse-slip dislocations is found. At about 45 % true strain more than a third the dislocations (of screw and edge type) found in the material have transverse character.

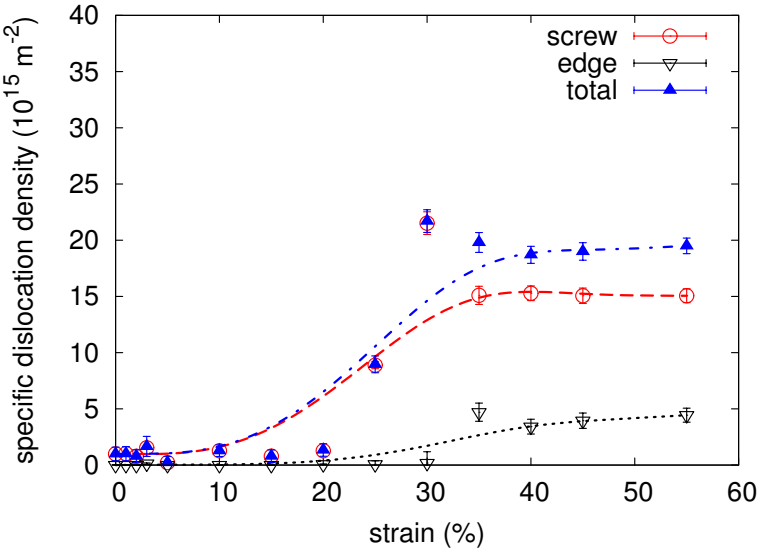


**Figure 9.5.:** Absolute densities of screw (○), edge (▽) and total dislocations (▲) as a function of the applied strain.

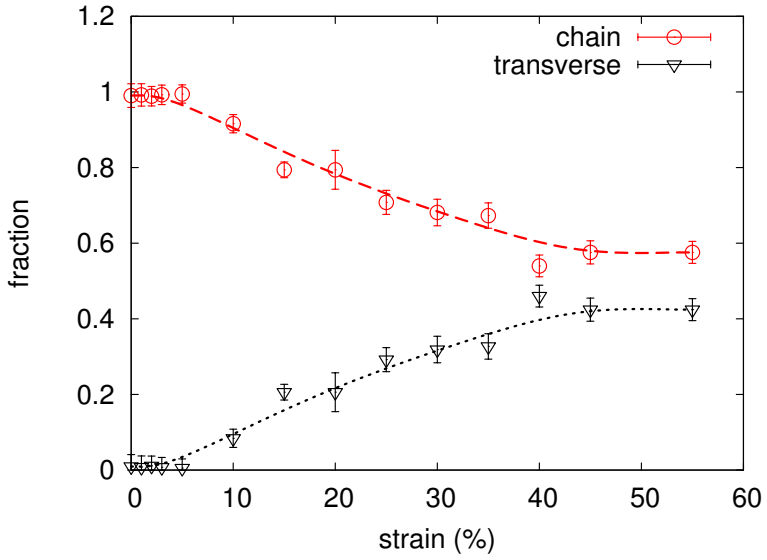


**Figure 9.6.:** Fraction of chain (○) and transverse dislocations (▽) as a function of the applied strain.

### 9.3.2. Discussion

In contrast to texture measurements where the activated slip systems can be determined with relatively high precision (e.g. [40, 114]) the present experiment provide information on the presence of possible strain carriers (the dislocations) in the material. The term *possible* is important as the density and relative population of dislocations in the different slip systems does not give any information on their mobility. What the present results do provide is information on their evolution upon changes in the physical environment which might eventually lead to a more concise understanding of the kinetics of the mentioned strain carriers.

The model of Peterson and Young (Section 2.3.2) assumes the thermally activated generation of screw dislocations on the lamella surfaces, mainly of the chain type. The present results show a high relative concentration of screw dislocations in the undeformed melt crystallised sample. Upon small deformation this type seems to be partly consumed indicating that some are indeed mobile. This is rather surprising because for other materials grown-in dislocations are mostly not mobile [115]. As the increase of the total dislocation density cannot be explained by pure generation of edges also a considerable amount of screws is generated indicating that in absolute terms for higher strains new mobile screw dislocations have to be generated (Figure 9.5).

The energetically less favoured dislocations of edge type, particularly the ones with transverse slip character do not seem to be consumed to the same extent as the screws and their relative number increases with increasing deformations. After deformation about 20 % of the present dislocations have edge character. The fact that almost about 50 % of dislocations are of transverse type after the deformation is in agreement with earlier investigations suggesting that most of the plastic deformation occurs by chain slip [40, 116, 109, 111].

## 9.4. Conclusions

In this chapter numerically calculated values for the dislocation contrast factors of $\alpha$-phase isotactic polypropylene have been presented for the first time. In a first application to experimental X-ray line width data of $\alpha$-iPP it was shown that dislocation types can be identified in semicrystalline polymers by methods of XPA and that the study of the kinetics of their evolution is also possible.

From Figures 9.4, and 9.6 it can be derived that the low energy dislocations of screw type with chain character in charge of deformation (due to their higher mobility) while the edges and the transverse dislocations remain immobile in the material, cannot annihilate and are thus accumulated. The considerable increase of the dislocation density at higher deformations is again an indication that the increasing back-stresses occurring at larger deformations (close to transition point $C$ [S2]) play an important role for the evolution of the micro-structure of the crystalline phase.

# Part IV.

# Summary and Outlook

In this last part of the thesis the results of the two preceding parts are reviewed and discussed in terms of the consequences for future work done in the field. Therefore the concluding chapter 11 will give an outlook on the possible paths to continue the research on the basis of the present work.

# 10. Summary

This thesis has presented investigations of the deformation induced changes of the microstructure of a number of semicrystalline polymers. The main focus was on iPP and PHB but mechanical investigations also involved PE.

By means of uniaxial loading-unloading experiments it was possible to characterise the the critical strains B and C in all investigated materials. These points are related to the characteristic properties of the deformation of semicrystalline polymers and reflect changes in the microstructure. Only slight differences were found for the investigated materials with respect to these points but a closer investigation of the loading unloading cycles revealed considerable changes in the evolution of the absorbed energy and the elastic modulus for PHB as compared to iPP and PE. As a consequence Point B, corresponding to the yield point, can be microstructurally attributed to the onset of macroscopic flow either by crystallographic slip (iPP,HDPE) or lamellar fragmentation in the case of PHB. Additionally the Point C could be related in all investigated materials to the locking of the flow in the entangled amorphous phase leading to a rubbery hardening that can be described by a Haward-Thackray Model.

An extensive part of this work is devoted to the application of Multiple X-ray Profile Analysis to iPP and PHB. MXPA experiments in PE are not practicable because of the low number of independent X-ray reflections. By comparison with DSC experiments it was not only possible to show that MXPA gives very good results for the lamella thickness distributions but it was demonstrated that crystalline defects have to be taken into account. The good agreement between X-ray and DSC results should allow to use DSC to determine reasonable starting parameters for MXPA. By direct numerical computation of $A^S(L)$ from $g(\lambda)$ one could even fully account for the size broadening in future investigations of similar polymers. Still a problematic point could lie in the investigation of multimodal size-distributions.

MXPA experiments reveal that in polypropylene the deformation processes involves the presence and production of dislocations. The calculation of the specific dislocation contrast factor even allowed for a characterisation of the types and orientations of the dislocations present in the bulk material. The deformation induced kinetics reveal that the less mobile edge dislocations are accumulated while mainly screw dislocations are consumed for deformation. Also the chain-slip dislocations, which seem to be the main slip carriers, are consumed for deformation, while transverse dislocations are accumulated. Especially for strains higher than the critical value of transition point C where the locking of the amorphous network becomes important, a

considerable change of the dislocation structure is observed involving a considerable increase in the number of transverse slip dislocations.

The MXPA investigations in PHB draw a completely different picture. The dislocation density does not change with plastic deformation, which suggest mechanisms as a balance of dislocation annihilation and generation, deformation-induced adiabatic melting, or brittle fragmentation of the lamellae. Based on SEM investigations, the evolution of the elastic modulus and the crystallinity as a function of plastic strain, brittle fragmentation was identified as the most probable mechanism active in PHB.

As a comparable behaviour as in PHB with respect to the stiffness of the crystallites has been observed in $\gamma$-iPP, an important conclusion of this work is the fact that a general deformation mechanism for the crystalline phase of semicrystalline polymers does not exist. Nonetheless, also in polymers, dislocation mediated plasticity assures good ductility if present – as could be shown with the experiments on $\alpha$-iPP.

# 11. Outlook

The existence of dislocations in melt crystallised polymers has been confirmed in this thesis. Furthermore MXPA has shown to be a powerful tool for the investigation of semicrystalline polymers. These two points suggest two red lines for future research.

The first red line concerns the role of dislocations for the mechanical properties of semicrystalline polymers. It leads to several questions that have to be answered separately for each semicrystalline polymer investigated.

(a) In how far do dislocations affect the mechanical properties?

(b) What are the mechanisms of dislocation generation and/or interaction and what are the specific consequences for the mechanical properties and the microstructure behind?

(c) In case dislocations do not play a role for the plasticity of the polymer, what are the alternative and competing mechanisms governing the strength, as e.g. microcracking, adiabatic melting and/or shear banding?

The second red line implies the development and application of MXPA as a standardised tool for the investigation of semicrystalline nano-materials in general and in polymers in particular. The limits in the application of MXPA in polymers is mainly situated in the strong overlapping of the diffraction peaks, the low symmetry, and the small crystallite sizes. Some of these problems could be resolved for the case of $\alpha$-iPP and PHB but it is still a very difficult task. Another problem lies in the low number of high intensity X-ray reflections for many semicrystalline polymers. An interesting route in this context may lie in the application of so called single peak methods such as the momentum method suggested by Groma [67].

# Acknowledgements

This thesis would not have been possible without the financial support of my employers of the last years, the Universities of Vienna and Thessaloniki. In this context the financial support of the funding projects the PhD initiative college I-022 "Experimental Materials Science–Nanostructured Materials" and within the focus project "Bulk Nanostructured Materials", both granted by the University of Vienna and the European Union project 'RTN-DEFINO' HPRN-CT-2002-00198 are gratefully acknowledged.

Without the strong support of the supervisor of this thesis *Prof. Dr. Michael Zehetbauer* who was deeply convinced of the experimental approach of this work it would never have reached this stage. His profound knowledge of materials physics in general and of the microstructural processes related to dislocation activity were extremely important for its success. I am very thankful for his support as supervisor and as an understanding superior who never ignored the importance of the human aspect in science.

I am very thankful for the support of *D.I. Harald Wilhelm* who recruited me and sparked my interest for polymer science. His creativity and his profound knowledge in polymer science allows him to unravel new aspects hidden in the experimental data at every glance, which is an excellent cure against all types of "déformation professionelle". *Gerald Polt* joined us in 2008 and turned out to be a very gifted experimentalist. I would like to thank him for his support in many experiments and evaluations.

I want to express my gratitude to *Mag. Michael Kerber*, *Dr. Erhard Schafler*, *Dr. Daria Setman*, *D.I. Bartek Bonarski*, *Roman Schuster*, *Christian Holzleithner*, *Prof. Dr. Viktor Gröger*, *Prof. Dr. Franz Sachslehner* , *Suzi Kahofer* and *Mag. Jelena Horky* and the research group Φnm (Physics of Nanostructured Materials) for their tireless effort whenever help and support was needed.

I am extremely thankful to *Prof. Dr. Gerhard Krexner* for his support in many aspects of this thesis and I hope that our cooperation can culminate in joint publications on tensoresistive polymers. I am very grateful for great scientific discussions and all kind of other support to *Prof. Dr. Said Ahzi*, *Prof. Dr. Elias Aifantis*, *Dr. Avraam Konstatinidis*, *Prof. Dr. Ali S. Argon*, *Dr. Sigrid Bernstorff*, *Dr. Frédéric Addiego*, *Dr. Olivier Guéguen*, and many others.

*Dr. Stephan Puchegger* is thanked for his help to obtain SEM data and *Dr. Johnnes Koppensteiner* is acknowledged for his support pertaining mechanical analysis. Mrs *Regina Pinter* who was the unfaltering navigator through the shallows of administration over the whole time is gratefully acknowledged.

I also have to thank my *parents* and *family* and last but not least my wonderful wife *Martina* who was understanding and supportive throughout the whole time I dedicated to this work.

# Part V.

# Appendix

# A. GnuOctave Code

## A.1. Contrastfactor.m

```
1
2
3  #Calculation of Contrast Factor for arbitrary symetry materials
4  #See Martinez-Garcia 2009,Acta Cryst A65 pp 109-119 and related
5  #Version 8.0.1
6  #
7  #Usage: Edit Material in the appropriate file 'material.m' and uncomment
       corresponding line
8  #
9  #scalars are in  lower case, vectors and tensors upper case
10
11
12 %%%%%%%%%%%%%%%%%%%%%%%%%%%%%%%%%%%
13 %Preamble
14 %%%%%%%%%%%%%%%%%%%%%%%%%%%%%%%%%%%
15 printf('\n-----------------------------------------\n');
16 printf('- Calculation of Contrast Factor -\n');
17 printf('-----------------------------------------\n\n');
18
19
20 %%%%%%%%%%%%%%%%%%%%%%%%%%%%%%%%%%%
21 % Load Material Constants
22 %%%%%%%%%%%%%%%%%%%%%%%%%%%%%%%%%%%
23 %[Stiffness,a,b,c,alpha,beta,gamma,hkl_matrix,uvw_matrix,disltype_matrix,
       diffr_vector_matrix]=Cu;
24 %[Stiffness,a,b,c,alpha,beta,gamma,hkl_matrix,uvw_matrix,disltype_matrix,
       diffr_vector_matrix]=alphaMg2SiO2
25 [Stiffness,a,b,c,alpha,beta,gamma,hkl_matrix,uvw_matrix,disltype_matrix,
       diffr_vector_matrix]=alphaiPP;
26 fflush(stdout);
27 %%%%%%%%%%%%%%%%%%%%%%%%%%%%%%%%%%%
28 %Calculate Relevant Parameters
29 %%%%%%%%%%%%%%%%%%%%%%%%%%%%%%%%%%%
30
31 %orthonormal system
32 I_orth=[1;0;0];
```

```
J_orth=[0;1;0];
K_orth=[0;0;1];

% Volume of Unit cell
V=a*b*c*sqrt(1-cosd(alpha)^2-cosd(beta)^2-cosd(gamma)^2+2*cosd(alpha)*cosd(beta)*cosd(gamma)); %V=det(inv(M));

%reciprocal parameters in ortho coords
a_star=b*c*sind(alpha)/V;
b_star=c*a*sind(beta)/V;
c_star=a*b*sind(gamma)/V;
alpha_star=asin(V/(a*b*c*sind(beta)*sind(gamma)))/pi*180;
beta_star=asin(V/(a*b*c*sind(alpha)*sind(gamma)))/pi*180;
gamma_star=asin(V/(a*b*c*sind(alpha)*sind(beta)))/pi*180;
fflush(stdout);

%definition of M
M=[1/a,0,0;
    -cosd(gamma)/(a*sind(gamma)),1/(b*sind(gamma)),0;
     a_star*cosd(beta_star),b_star*cosd(alpha_star),c_star];


%Vector formulation of unit cell in orthonormal variables
A=inv(M)'*I_orth;
B=inv(M)'*J_orth;
C=inv(M)'*K_orth;

A_star=cross(B,C)/V;
B_star=cross(C,A)/V;
C_star=cross(A,B)/V;

%calculation of G_m from M
G_m=inv(M)*inv(M');

%Calculate Twotheta for plot (monoclinic)
lambda=1.542; %wavelength (Angstrom)
hd=diffr_vector_matrix(:,1);
kd=diffr_vector_matrix(:,2);
ld=diffr_vector_matrix(:,3);
twotheta=2*asind(lambda/2*sqrt(hd.^2/(a^2*sind(beta)^2)+kd.^2/b^2+ld.^2/(c^2*sind(beta)^2)-2*(hd.*ld)*cosd(beta)/(a*c*sind(beta)^2))); %we should put the general formulation here

%%%%%%%%%%%%%%%%%%%%%%%%%%%%%%%%%%%
%cycle over slip systems
%%%%%%%%%%%%%%%%%%%%%%%%%%%%%%%%%%%
%initialise
CF=[];
```

```
78  Delta=[];
79
80  for hklnr=1:rows(hkl_matrix)
81  printf('\n***********************************************************************\n')
        ;
82  printf('* Evaluate Slip System: slip plane: (%g %g %g) burgers vector:[%g %g %g], 
        phi= %g.\n',hkl_matrix(hklnr,:),uvw_matrix(hklnr,:),disltype_matrix(hklnr));
83  printf('***********************************************************************\n');
84
85  %slip plane (reciprocal coordinates)
86  HKL=[hkl_matrix(hklnr,1);hkl_matrix(hklnr,2);hkl_matrix(hklnr,3)];
87  h=HKL(1);
88  k=HKL(2);
89  l=HKL(3);
90
91  %burgersvector (lattice coordinates)
92  UVW=[uvw_matrix(hklnr,1);uvw_matrix(hklnr,2);uvw_matrix(hklnr,3)];
93  u=UVW(1);
94  v=UVW(2);
95  w=UVW(3);
96  fflush(stdout);
97
98  %dislocation character (0 screw, 90 edge)
99  phi=disltype_matrix(hklnr);
100
101 %%%%%%%%%%%%%%%%%%%%%%
102 %Calculation of transformation matrix P=[C_1,C_2,C_3]
103 %%%%%%%%%%%%%%%%%%%%%%
104
105 %C_2
106 %slip plane normal N (orto coords)
107 N=h*A_star+k*B_star+l*C_star;
108 %absolute length of N
109 n=norm(N);
110 %coordinates of C_2
111 C_2=1/n*M*HKL;
112
113 %C_3
114 % Burgers Vector Burg (ortho coords)
115 Burg=u*A+v*B+w*C;
116 %absolute length burgers vector
117 burg=sqrt(UVW'*G_m*UVW);
118 % normalized burgers vector in ortho coords
119 Cb_3=Burg/burg;
120 %define rotation matrix Rot(phi,C_2)
121 c21=C_2(1);
122 c22=C_2(2);
123 c23=C_2(3);
```

```
Rot=[c21^2*(1-cosd(phi))+cosd(phi),c21*c22*(1-cosd(phi))+c23*sind(phi),c21*c23*(1-cosd(phi))-c22*sind(phi);
c21*c22*(1-cosd(phi))-c23*sind(phi),c22^2*(1-cosd(phi))+cosd(phi),c22*c23*(1-cosd(phi))+c21*sind(phi);
c21*c23*(1-cosd(phi))+c22*sind(phi),c22*c23*(1-cosd(phi))-c21*sind(phi),c23^2*(1-cosd(phi))+cosd(phi)]
C_3=Rot*Cb_3;

%C_1
C_1=cross(C_2,C_3);

%Definition of transformation matrix P
P=[C_1';C_2';C_3']

%%%%%%%%%%%%%%%%%%%%%%%%%%%%%%%%%%%%
% Calculate E_ijmn through eigenvalue problem
%%%%%%%%%%%%%%%%%%%%%%%%%%%%%%%%%%%%

%transform Stiffness to slip system coords
 TStiffness=voigt2tensor(Stiffness);      %voigt 2 tensor notation
TCturn=transform(TStiffness,(inv(P))'); %transformation ortho to slip coordinate system Stiffness  (P transforms from ortho to slip)
Cturn=tensor2voigt(TCturn);              %transform back to voigt

% define Q, R ,T see Ting aniostropic elasticity
Q=reshape(TCturn(:,1,:,1),3,3);
R=reshape(TCturn(:,1,:,2),3,3);
T=reshape(TCturn(:,2,:,2),3,3);

%Define Nfund fundamental Elasticity matrix (see Ting)
N1=-inv(T)*R';
N2=inv(T);
N3=R*inv(T)*R'-Q;
N4=N1';
Nfund=[N1,N2;N3,N4];
% check if eigenvalue problem is ill posed
conditionnumber=cond(Nfund)

% solve eigenvalue problem with eig
[EVECT,EVAL]=eig(Nfund);
psol=eig(Nfund)
A_alpha=EVECT(1:3,:);
L_alpha=EVECT(4:6,:);
fflush(stdout);

Burgnorm=((inv(M)*inv(P))'*UVW/burg)


```

```
168 %calculate E_ijmn
169 phi_polar=vec(0:0.001:2*pi);
170 %initialize Etensor
171 Etensor=ones(3,2,3,2);
172 countere=1;
173 for eindi=1:3
174         for eindj=1:2
175                 for eindm=1:3
176                         for eindn=1:2
177                                 countere++; %setting all 36 values of matrix?
178                                 %normalized burgersvector in slip system
                                        coordinates : (inv((P*M)')*UVW)/burg #check!!!
179                                 beta_ij = dstrain(A_alpha,L_alpha,psol,((inv(M)*
                                        inv(P))'*UVW/burg),phi_polar,eindi,eindj);
180                                 beta_mn = dstrain(A_alpha,L_alpha,psol,((inv(M)*
                                        inv(P))'*UVW/burg),phi_polar,eindm,eindn);
181                                 %plot(phi_polar,cumtrapz(phi_polar,beta_ij.*
                                        beta_mn))
182                                 %pause(0.1)
183                                 Evalu=1/pi(1,"double")*trapz(phi_polar,beta_ij.*
                                        beta_mn);
184                                 Etensor(eindi,eindj,eindm,eindn)=Evalu;
185                         endfor
186                 endfor
187         endfor
188 endfor
189
190 % transform E_ijmn to 6*6 matrix E_hat
191 E_hat=ones(6,6);
192 countereh=1;
193 for tri=1:3
194         for trj=1:2
195                 for trm=1:3
196                         for trn=1:2
197                                 countereh++;
198                                 if trj==1
199                                         rk=tri;
200                                 endif
201                                 if trj==2
202                                         rk=tri+3;
203                                 endif
204                                 if trn==1
205                                         rl=trm;
206                                 endif
207
208                                 if trn==2
209                                 rl=trm+3;
210                                 endif
```

```
211                                     E_hat(rk,rl)=Etensor(tri,trj,trm,trn);
212                                     endfor
213                             endfor
214                     endfor
215             endfor
216             printf('E_hat=\n');
217             printf('| %8.4f %8.4f %8.4f %8.4f %8.4f %8.4f |\n',E_hat)
218             fflush(stdout);
219
220             %%%%%%%%%%%%%%%%%%%%%%%%%%%%%%%%%%%%
221             %Start CF Calculation for the different reflexes in the slipsystem
222             %(cycle over diffr_vector matrix)
223             %%%%%%%%%%%%%%%%%%%%%%%%%%%%%%%%%%%%
224             CF_sys=[];
225             Delta_sys=[];
226             for diffnr=1:rows(diffr_vector_matrix)
227
228             % calculate diffraction vector in different coordinate systems
229             Diffr=[diffr_vector_matrix(diffnr,1);diffr_vector_matrix(diffnr,2);
                    diffr_vector_matrix(diffnr,3)];  %in the reciprocal frame
230             DIFFR=Diffr(1)*A_star+Diffr(2)*B_star+Diffr(3)*C_star; %in orthonormal coordinates
231             %define absloute length of diffracrion vector
232             diffr=norm(DIFFR);
233
234             %%%%%%%%%%%%%%%%%%%%%%%%%%%%%%%%%%%%%%%%%%%%
235             %calculate Geo_ijmn
236             %%%%%%%%%%%%%%%%%%%%%%%%%%%%%%%%%%%%%%%%%%%%
237             tau1=DIFFR'*C_1/(diffr*norm(C_1));
238             tau2=DIFFR'*C_2/(diffr*norm(C_2));
239             tau3=DIFFR'*C_3/(diffr*norm(C_3));
240             tau=[tau1;tau2;tau3];
241
242             %calculate Geo_ijmn
243             %initialize Geo
244             Geo=ones(3,2,3,2);
245             counterg=1;
246             for gindi=1:3
247                     for gindj=1:2
248                             for gindm=1:3
249                                     for gindn=1:2
250                                             counterg++; %setting all 36 values of matrix?
251                                             gval=tau(gindi)*tau(gindj)*tau(gindm)*tau(gindn);
252                                             Geo(gindi,gindj,gindm,gindn)=gval;
253                                             fflush (stdout);
254                                     endfor
255                             endfor
256                     endfor
257             endfor
```

```

% transform Geo_ijmn to 6*6 matrix Geo_hat
Geo_hat=ones(6,6);
countergh=1;
for tri=1:3
	for trj=1:2
		for trm=1:3
			for trn=1:2
				countergh++;
				if trj==1
					rk=tri;
				endif
				if trj==2
					rk=tri+3;
				endif
				if trn==1
					rl=trm;
				endif

				if trn==2
				rl=trm+3;
				endif
				Geo_hat(rk,rl)=Geo(tri,trj,trm,trn);
				endfor
		endfor
	endfor
endfor
%printf('Geo_hat=\n');
%printf('| %8.4f %8.4f %8.4f %8.4f %8.4f %8.4f |\n',Geo_hat)

%%%%%%%%%%%%%%%%%%%%%%%%%%%%%%%%%%%%
%Calculate Contrastfactor(hkl) from G_ijmn E_ijmn and (see e.g. martinez-garcia2009)
%%%%%%%%%%%%%%%%%%%%%%%%%%%%%%%%%%%%

%initailize
cfactor=0;
counterc=1;
for conti=1:3
	for contj=1:2
		for contm=1:3
			for contn=1:2
			counterc++;
			etval=Etensor(conti,contj,contm,contn);
			gtval=Geo(conti,contj,contm,contn);
			contrval=Etensor(conti,contj,contm,contn)*Geo(conti,contj,contm,contn);
			cfactor=cfactor+contrval;
```

```
304                             fflush(stdout);
305                             endfor
306                     endfor
307             endfor
308     endfor
309     CF_sys=[CF_sys;cfactor];
310
311     %Calculate relevant angles delta,chi, eta
312
313     %%direction cosines between Diffr and C-Axis
314     delta=acosd(dot(M*Diffr,C)/(norm(M*Diffr)*norm(C)));
315     %%direction cosines between Diffr and B-Axis
316     %delta=acosd(dot(M*Diffr,B)/(norm(M*Diffr)*norm(B)));
317     %%direction cosines between Diffr and A-Axis
318     %delta=acosd(dot(M*Diffr,A)/(norm(M*Diffr)*norm(A)));
319
320     Delta_sys=[Delta_sys;delta];
321
322
323     %%direction cosines between Diffr and Line(chi) Burgers Vector (eta)
324     chi=atan2(norm(cross(DIFFR,C_3)),dot(DIFFR,C_3))*180/pi();
325     %eta=atan2(norm(cross(DIFFR,Burg)),dot(DIFFR,Burg))*180/pi();
326     eta=acosd(dot(M*Diffr,Burg)/(norm(M*Diffr)*burg));
327
328     % Print Result
329     printf('The Contrastfactor of the (%g %g %g) Reflex is: %8.4f (chi=%4.1f, eta=%4.1
        f) \n', Diffr, cfactor, chi,eta);
330     %end diffr_vector cycling
331     endfor
332
333     % store CF as matrix for later usage
334     CF=[CF,CF_sys];
335     Delta=[Delta,Delta_sys];
336
337     %end slip system cycling
338     endfor
339
340     printf('\n');
341     fflush(stdout);
342
343     %%%%%%%%%%%%%%%%%%%%%%%%%%%%%%%%%%%%%%%%%%%%%%%%%%%%
344     % Evaluate results for all slip systems
345     %%%%%%%%%%%%%%%%%%%%%%%%%%%%%%%%%%%%%%%%%%%%%%%%%%%%
346
347     system("mkdir results");
348
349     %Save CF
350     %octave format
```

```
351 save ("-text","./results/CF_octave.dat","CF","diffr_vector_matrix","twotheta","
    hkl_matrix","uvw_matrix","disltype_matrix")
352 % nice table for gnumeric or excel
353 [status, username]=system("echo -n $(whoami)");
354 [status, hostname]=system("echo -n $(hostname)");
355 extime=strftime ('%r (%Z) %A %e %B %Y', localtime (time ()));
356 savefile='./results/CF_table.dat';
357 printf('Saving Results to %s.\n',savefile);
358 fd = fopen(savefile,'w');
359 fprintf(fd,'# %s for polypropylene produced by %s@%s %s\n',savefile,username,
    hostname,extime);
360 fprintf(fd,'#Peakindex\t2theta(degree)\t');
361 for ind=1:rows(hkl_matrix)
362 fprintf(fd,'C_[%g%g%g](%g%g%g) %g\t',hkl_matrix(ind,:),uvw_matrix(ind,:),
    disltype_matrix(ind));
363 endfor
364 fprintf(fd,'\n');
365 for ind=1:rows(CF)
366         fprintf(fd,'[%2g %2g %2g]\t%7.3g\t', diffr_vector_matrix(ind,:), twotheta(
            ind));
367         for ind2=1:columns(CF)
368         fprintf(fd,'%10.8g\t',CF(ind,ind2));
369         endfor
370         fprintf(fd,'\n');
371 endfor
372 fclose(fd);
373
374 %plot CF(delta)
375 for ind=1:columns(CF)
376         subplot(columns(CF),1,ind)
377         [dsort_sys,idsort_sys]=sort(Delta(:,ind));
378         plot(dsort_sys,CF(:,ind)(idsort_sys),"-o")
379         titlestring=sprintf('Slip System (%g %g %g) [%g %g %g], phi= %g',
            hkl_matrix(ind,:),uvw_matrix(ind,:),disltype_matrix(ind));
380         title(titlestring);
381         xlabel("{/Symbol d} (degree)");
382         ylabel("CF")
383 endfor
384 print("./results/Delta.eps","-depsc2","-F24")
385 pause
386 subplot(1,1,1)
```

# B. Curriculum Vitae

### Florian Spieckermann (Mag. rer. nat.)

| | |
|---|---|
| born | July 7, 1979 |
| in | Göttingen, Germany |

### Professional Experience

| | |
|---|---|
| since 08/2010 | Researcher at the University of Vienna, Austria, research group Physics of Nanostructured Materials |
| 10/2009-06/2010 | Freelancer at the University of Vienna, Austria, research group Physics of Nanostructured Materials |
| 10/2006-09/2009 | Initiative College Assistant at the Department of Materials Physics, University of Vienna, Austria in the framework of the Initiative College (PhD. Program) "Experimental Materials Science - Nanostructured Materials" of the University of Vienna |
| 04/2006-09/2006 | Researcher within RTN-DEFINO (EU-FP 5&6 project) "Deformation and fracture instabilities in novel materials and processes" at Laboratory for Mechanics and Materials (Head: E.C. Aifantis), Aristotele University Thessaloniki, Greece |

### Education

| | |
|---|---|
| since 04/2006 | Phd thesis *"Investigation of Deformation Induced Changes of the Microstructure in Composite Polymer Systems and their Impact on Macroscopic Physical Properties"* supervised by Ao. Univ. Prof. Dr. Michael Zehetbauer, Researchgroup Physics of Nanostructured Materials, University of Vienna, Austria |
| 1999 - 2006 | Physics, University of Vienna, Austria, graduation with "Magister der Naturwissenschaften"; supervised by Ao. Univ. Prof. Dr. Michael Zehetbauer, Institute of Materials Physics, University of Vienna, Austria |

| | |
|---|---|
| 1997 - 1999 | Architecture, Federal Institute of Technology Lausanne (EPFL), Switzerland |
| 1992/93 | Cours de Français at Collège de Champittet, Lausanne, Switzerland (year abroad), graduation with Diplôme de Langue of the Alliance Française |
| 1990 - 1997 | Gymnasium St.Ursula (high school), Vienna, Austria, graduation with Austrian Matura (A-levels) |
| 1988/89 | Janusz-Korzcak-Schule (primary school), Göttingen, Germany |
| 1985 - 1988 | Volksschule Bendagasse (primary school), Vienna, Austria |

November 28, 2010

**List of Publications**

**Peer Reviewed Articles**

8. *Generation of dislocations in isotactic polypropylene studied by X-ray line profile analysis*, H. Wilhelm, F. Spieckermann, E. Schafler, S. Bernstorff and M.J. Zehetbauer, in preparation.

7. *X-ray Line Profile Analysis – An Ideal Tool to Quantify Structural Parameters of Nanomaterials* , M.B. Kerber, M.J. Zehetbauer, E. Schafler, F.C. Spieckermann, S. Bernstorff and T. Ungar, JOM, (2010), in press.

6. *"Nano"-effects in your coffee maker?*, F. Spieckermann, Atomium Culture, (2010) in press.

5. *Determination of lamella thickness distributions in isotactic polypropylene by X-ray line profile analysis*, F. Spieckermann, H. Wilhelm, M. Kerber, E. Schafler, S. Bernstorff and M.J. Zehetbauer, Polymer, (2010), 51, 4195-4199

4. *Plasticity and X-ray Line Profile Analysis of Poly(3-hydroxybutyrate)*, F. Spieckermann, H. Wilhelm, M. Kerber, E. Schafler, S. Bernstorff and M.J. Zehetbauer, Journal of Physics: Conference Series, 15th International Conference on the Strength of Materials (ICSMA 15), (2010), 240, 012146.

3. *Mechanical properties of filled antimonide skutterudites*, L. Zhang, G. Rogl, A. Grytsiv, S. Puchegger, J. Koppensteiner, F. Spieckermann, H. Kabelka, M. Reinecker, P. Rogl, W. Schranz, M. Zehetbauer, M.A. Carpenter, Materials Science and Engineering B, (2010), 170, 26-31.

2. *Determination of critical strains in isotactic polypropylene by cyclic loading - unloading*, F. Spieckermann, H. Wilhelm, E. Schafler, E.C. Aifantis and M.J. Zehetbauer, Journal of Engineering Materials and Technology, (2009), 131, 011109-5.

1. *Application of composite models to isotactic polypropylene for the determination of phase specific stress-strain curves*, F. Spieckermann, H. Wilhelm, E. Schafler, S. Ahzi and M. Zehetbauer, Materials Science and Engineering A, (2008), 483-484, 76–78.

**Other Publications**

2. *Investigation of the existence and of the kinetics of dislocation generation in biodegradable semicrystalline poly(3-hydroxybutyrate) (PHB) by in-situ WAXS deformation*, F. Spieckermann, H. Wilhelm, E. Schafler, M. Kerber, E. Schafler, S. Bernstorff and M.J. Zehetbauer, Annual Report of the Austrian SAXS Beamline at Elettra 2008, Trieste.

1. *Untersuchung der mechanischen Eigenschaften und Anwendung von Verbundmodellen zur Bestimmung phasenspezifischer Spannungs - Dehnungs - Kurven an isotaktischem*

*Polypropylen*, F. Spieckermann, Diploma thesis supervised by Ao. Univ. Prof. Dr. M. Zehetbauer, Nanocrystalline Materials Group, Institute of Materials Physics, University of Vienna, March 2006.

## Talks and Conference Contributions

08/2009 *Plasticity and X-ray Profile Analysis of Poly(3-hydroxybutyrate)*, ICSMA 15 - International Conference on the Strength of Materials, oral, Dresden, Germany.

08/2009 *Mechanical behaviour of glasses and non-crystalline solids*, ICSMA 15 - International Conference on the Strength of Materials, E. Schafler et al. (co- and presenting-author F.S.), poster, Dresden, Germany.

08/2009 *Phase-Specific Mechanisms of Plasticity in Polymorphic Polypropylene*, ICSMA 15 - International Conference on the Strength of Materials, H. Wilhelm et al. (co-author F.S.), oral, Dresden, Germany.

11/2008 *On the Role of Dislocations for the Mechanical Properties of Semicrystalline Polymers*, ICPB 3 - International Conference on Polymer Behaviour, oral, Marrakesh, Morocco.

10/2008 *Nano-Effects of Mechanical Properties in Semicrystalline Polymers?*, Nanoplasticity Workshop, poster, Lake Bostal, Germany.

09/2008 *In-situ SANS Investigation of Strained Conductive Polymer-Carbon Co-mposites*, Jahrestagung der Österreichischen Physikalischen Gesellschaft, poster, Leoben, Austria.

09/2008 *In-situ SANS Investigation of Strained Conductive Polymer-Carbon Composites*, Deutsche Neutronenstreutagung, poster, Garching, Germany.

09/2007 *Determination of critical strains in isotactic polypropylene by cyclic loading - unloading*, SHEAR07 Symposium, oral, Nancy, France.

05/2007 *Investigation of the mechanical properties of isotactic polypropylene by cyclic compression and application of simple rheological composite models*, Final meeting of RTN-DEFINO, oral, Thessaloniki, Greece.

10/2006 *Investigation of the mechanical properties of isotactic polypropylene by cyclic compression and comparison to rheological composite models*, EUROMECH Colloquium 487 "Structure Sensitive Mechanics of Polymer Materials: Physical and Mechanical Aspects", oral, Strassbourg, France.

07/2006 *Composite models for nonlinear stress strain curves in semicrystalline polymers* 19th Panhellenic Conference and Summerschool on Nonlinear Science and Complexity, oral, Thessaloniki, Greece.

06/2006 *Application of composite models to isotactic polypropylene for the determination of phase specific stress-strain curves* ICSMA 14 - International Conference on the Strength of Materials, oral, Xian, China.

07/2004 *Structural and micromechanical alterations of isotactic polypropylene due to compression*, Austrian SPD Meeting, Erich Schmid Institute of Materials Science, Austrian Academy of Sciences, oral, Leoben, Austria.

# List of Abbreviations

| | |
|---|---|
| CRSS | critical resolved shear stress |
| CSD | coherently scattering domain |
| DSC | differential scanning calorimetry |
| FWHM | full width at half mean. |
| HDPE | high density polyethylene |
| iPP | isotactic polypropylene |
| MXPA | multireflection X-ray line profile analysis |
| P3HB | poly(3-hydroxybuthyrate) |
| PA | polyamide (tradename Dupont: nylon) |
| PE | polyethylene |
| PHB | polyhydroxybutyrate |
| SAXS | small angle X-ray scattering |
| SEM | scanning electron microscope |
| UV | ultraviolet |
| WAXS | wide angle X-ray scattering |
| XPA | X-ray line profile analysis |

# List of Figures

# List of Tables

# List of Included Articles

[S1] F. Spieckermann. "Nano"-effects in your coffee maker? *Atomium Culture*, accepted, 2010.

[S2] F. Spieckermann, H. Wilhelm, E. Schafler, E. Aifantis, and M. Zehetbauer. Determination of critical strains in isotactic polypropylene by cyclic loading-unloading. *J. Eng. Mater. Technol.*, 131(1):011109–5, January 2009.

[S3] F. Spieckermann, H. Wilhelm, E. Schafler, M. Kerber, S. Bernstorff, and M.J. Zehetbauer. Plasticity and x-ray line profile analysis of the semicrystalline polymer poly(3-hydroxybutyrate). *Journal of Physics: Conference Series*, 240(1):012146, 2010.

[S4] F. Spieckermann, H. Wilhelm, M. Kerber, E. Schafler, G. Polt, S. Bernstorff, F. Addiego, and M. Zehetbauer. Determination of lamella thickness distributions in isotactic polypropylene by X-ray line profile analysis. *Polymer*, 51(18):4195–4199, August 2010.

# Bibliography


[1] Atomium culture. URL: http://atomiumculture.eu, 2010. Revision as of Sep 14 10:16:30 CEST 2010.

[2] P. J. Flory and D. Y. Yoon. Molecular morphology in semicrystalline polymers. *Nature*, 272(5650):226–229, March 1978.

[3] H. Wilhelm, A. Paris, E. Schafler, S. Bernstorff, J. Bonarski, T. Ungar, and M.J. Zehetbauer. Evidence of dislocations in melt-crystallised and plastically deformed polypropylene. *Materials Science and Engineering A*, 387-389:1018–1022, 2004.

[4] A. Paris. Anwendung der BraggProfilanalyse zur Bestimmung von verformungsinduzierten Versetzungen in Polypropylen. Master's thesis, University of Vienna, 2003.

[5] L. Lin and A. S. Argon. Structure and plastic deformation of polyethylene. *J. Mater. Sci.*, 29(2):294–323, January 1994.

[6] A. Galeski and G. Regnier. Nano and micromechanics of crystalline polymers. In Jozsef Karger-Kocsis and Stoyko Fakirov, editors, *Nano- and micro-mechanics of polymer blends and composites*, pages 3–58. Hanser, Munich;Cincinnati Ohio, 2009.

[7] G. Strobl. *The Physics of Polymers*. Springer-Verlag Berlin Heidelberg, 1997.

[8] Dissemination of IT for the promotion of materials science (DoITPoMS), University of Cambridge. URL: http://www.doitpoms.ac.uk, 2010. Revision as of 14:26 UTC, 16 Nov 2010, images licensed under Attribution-Non-Commercial-Share Alike 2.0 UK: England & Wales.

[9] B. Crist. Plastic deformation of polymers. In R.W. Cahn, P. Haasen, and E.J. Kramer, editors, *Material Science and Technology*, volume 12. Structure and Properties of Polymers (Volume Editor: E.L. Thomas), pages 427–469. VCH Verlagsgesellschaft mbH, Weinheim, 1993.

[10] R. Hiss, S. Hobeika, C. Lynn, and G. Strobl. Network stretching, slip processes and fragmentation of crystallites during uniaxial drawing of polyethylene and related copolymers. *Macromolecules*, 32:4390–4403, 1999.

[11] Z. Bartczak. Influence of molecular parameters on high-strain deformation of polyethylene in the plane-strain compression. part ii. strain recovery. *Polymer*, 46:10339–10354, 2005.

[12] M.C. Boyce and E. Arruda. Constitutive models of rubber elasticity: A review. *Rubber Chem. Technol.*, 73:504–523, Jul/Aug 2000.

[13] L.R.G Treloar. *The physics of rubber elasticity.* Clarendon Press, Oxford, 1975.

[14] F. Spieckermann. Untersuchung der mechanischen Eigenschaften und Anwendung von Verbundmodellen zur Bestimmung phasenspezifischer Spannungs-Dehnungs-Kurven an isotaktischem Polypropylen. Master's thesis, University of Vienna, April 2006.

[15] A.N. Gent. A new constitutive relation for rubber. *Rubber Chemistry and Technology*, 69:59–61, 1996.

[16] W. Kuhn and F. Grün. Beziehungen zwischen elastischen Konstanten und Dehnungsdoppelbrechung hochelastischer Stoffe. *Colloid & Polymer Science*, V101(3):248–271, December 1942.

[17] A. Cohen. A pade approximation to the inverse langevin function. *Rheol. Acta*, 30:270–273, 1991.

[18] C. Horgan and G. Saccomandi. A molecular-statistical basis for the gent constitutive model of rubber elasticity. *Journal of Elasticity*, 68(1):167–176, July 2002.

[19] R.N. Haward and G. Thackray. The use of a mathematical model to describe isothermal stress-strain curves in glassy thermoplastics. *Proceedings of the Royal Society A*, 302:453–472, 1968.

[20] C. Bauwens-Crowet, J. C. Bauwens, and G. Homès. Tensile yield-stress behavior of glassy polymers. *Journal of Polymer Science Part A-2: Polymer Physics*, 7(4):735–742, 1969.

[21] H. Eyring. Viscosity, plasticity, and diffusion as examples of absolute reaction rates. *J. Chem. Phys.*, 4(4):283–291, April 1936.

[22] J. Richeton, S. Ahzi, K.S. Vecchio, F.C. Jiang, and A. Makradi. Modeling and validation of the large deformation inelastic response of amorphous polymers over a wide range of temperatures and strain rates. *International Journal of Solids and Structures*, 44(24):7938–7954, December 2007.

[23] J. Richeton. *Modeling and validation of the finite strain response of amorphous polymers for a wide range of temperature and strain rate.* PhD thesis, Université Louis Pasteur Strasbourg I, 2005.

[24] D. Fotheringham, B. W. Cherry, and C. Bauwens-Crowet. Comment on on the compression yield behaviour of polymethyl methacrylate over a wide range of temperatures and strain-rates. *Journal of Materials Science*, 11(7):1368–1371, July 1976.

[25] L. Lin and A. S . Argon. Rate mechanism of plasticity in the crystalline component of semicrystalline nylon 6. *Macromolecules*, 27:6903 – 6914, 1994.

[26] A.S. Argon, A. Galeski, and T. Kazmierczak. Rate mechanisms of plasticity in semicrystalline polyethylene. *Polymer*, 46(25):11798–11805, November 2005.

[27] O. Gueguen, J. Richeton, S. Ahzi, and A. Makradi. Micromechanically based formulation of the cooperative model for the yield behavior of semi-crystalline polymers. *Acta Mater.*, 56(7):1650–1655, April 2008.

[28] R. C. Scogna and R. A. Register. Rate-dependence of yielding in ethylene-methacrylic acid copolymers. *Polymer*, 49(4):992–998, February 2008.

[29] A. Galeski. Strength and toughness of crystalline polymer systems. *Prog. Polym. Sci.*, 28(12):1643–1699, December 2003.

[30] P. B. Bowden and R. J. Young. Deformation mechanisms in crystalline polymers. *Journal of Materials Science*, 9(12):2034–2051, December 1974.

[31] R. V. Mises. Mechanik der plastischen Formänderung von Kristallen. *ZAMM - Zeitschrift für Angewandte Mathematik und Mechanik*, 8(3):161–185, 1928.

[32] T. Kazmierczak, A. Galeski, and A.S. Argon. Plastic deformation of polyethylene crystals as a function of crystal thickness and compression rate. *Polymer*, 46(21):8926–8936, October 2005.

[33] Z. Bartczak, A. S.Argon, and R. E Cohen. Deformation mechanisms and plastic resistance in single-crystal-textured high-density polyethylene. *Macromolecules*, 25:5036–5053, 1992.

[34] A. Peterlin. Molecular model of drawing polyethylene and polypropylene. *Journal of Materials Science*, 6(6):490–508, June 1971.

[35] F.J. Balta-Calleja and C. Santa Cruz. Novel aspects of the microstructure of poly(ethylene oxide) as revealed by microhardness: Influence of chain ends. *Acta Polymerica*, 47(6-7):303–309, 1996.

[36] R.J. Young. A dislocation model for the yield in polyethylene. *Phil. Mag.*, 30:85–94, 1974.

[37] J.M. Peterson. Peierls stress for screw dislocations in polyethylene. *J. Appl. Phys.*, 39:4920–4928, 1968.

[38] N. Brown and S. Rabinowitz. Internal friction and microstrain in polyethylene at 77 k. *Macromolecules*, 37(3):872–876, 2004.

[39] Z. Bartczak and E. Martuscelli. Orientation and properties of sequentially drawn films of an isotactic polypropylene/ hydrogenated oligocyclopentadiene blend. *Polymer*, 38(16):4139–4149, August 1997.

[40] Z. Bartczak and A. Galeski. Yield and plastic resistance of [alpha]-crystals of isotactic polypropylene. *Polymer*, 40(13):3677–3684, June 1999.

[41] L. G. Shadrake and F. Guiu. Dislocations in polyethylene crystals: line energies and deformation modes. *Philos. Mag.*, 34(4):565–581, 1976.

[42] W.J. O'Kane and R.J. Young. The role of dislocations in the yield of polypropylene. *Journal of Materials Science Letters*, 14:433–435, 1995.

[43] 0. Darras and R. Séguéla. Tensile yield of polyethylene in relation to crystal thickness. *Journal of Polymer Science: Part B: Polymer Physics*, 31:759–766, 1993.

[44] L. Manevich. *Solitons in macromolecular systems.* Nova Biomedical Books, New York, 2008.

[45] S. Nikolov and D. Raabe. Yielding of polyethylene through propagation of chain twist defects: Temperature, stem length and strain-rate dependence. *Polymer*, 47(5):1696–1703, February 2006.

[46] D. Hull and D. J. Bacon. *Introduction to Dislocations.* Pergamon, third edition, 1984.

[47] G. Gottstein. *Physical Foundations of Material Science.* Springer-Verlag Berlin Heidelberg, 2004.

[48] T Ting. *Anisotropic elasticity : theory and applications.* Oxford University Press, New York, 1996.

[49] J. M. Peterson. Thermal initiation of screw dislocations in polymer crystal platelets. *J. Appl. Phys.*, 37(11):4047–4050, October 1966.

[50] B. Crist, C. J. Fisher, and P. R. Howard. Mechanical properties of model polyethylenes: tensile elastic modulus and yield stress buckley crist, christopher j. fisher, paul r. howard. *Macromolecules*, 22:1709–1718, 1989.

[51] R. Séguéla. Dislocation approach of the plastic deformation of semicrystalline polymers: Kinetic aspects for polyethylene and polypropylene. *Journal of Polymer Science:Part B: Polymer Physics*, 40:593–601, 2002.

[52] J. Hirth and J. Lothe. *Theory of dislocations.* Krieger Pub. Co., Malabar FL, 1992.

[53] B.J. Lee, A.S. Argon, D.M. Parks, S. Ahzi, and Z. Bartczak. Simulation of large strain plastic deformation and texture evolution in high density polyethylene. *Polymer*, 34:3555–3575, 1993.

[54] T. Ungár. *Defect and microstructure analysis by diffraction*, chapter A dislocation based model for strain broadening in X-ray line profile analysis, page 165. Oxford University Press, Oxford ;;New York, 1999.

[55] P. Scardi and M. Leoni. Whole powder pattern modelling. *Acta Crystallographica Section A: Foundations of Crystallography*, 58(2):190–200, 2002.

[56] T. Ungár and A. Borbély. The effect of dislocation contrast on x-ray line broadening: A new approach to line profile analysis. *Appl. Phys. Lett.*, 69(21):3173–3175, 1996.

[57] B. E. Warren and B. L. Averbach. The effect of cold-work distortion on x-ray patterns. *J. Appl. Phys.*, 21(6):595–599, June 1950.

[58] B. E. Warren and B. L. Averbach. The separation of cold-work distortion and particle size broadening in x-ray patterns. *J. Appl. Phys.*, 23(4):497–497, April 1952.

[59] M. A. Krivoglaz. *Theory of X-Ray and Thermal Neutron Scattering by Real Crystals.* Plenum Press, 1969.

[60] M. Wilkens. The determination of density and distribution of dislocations in deformed single crystals from broadened x-ray diffraction profiles. *Physica Status Solidi (a)*, 2(2):359–370, 1970.

[61] M. Wilkens. X-ray line broadening and mean square strains of straight dislocations in elastically anisotropic crystals of cubic symmetry. *phys. stat. sol. (a)*, 104(1):K1–K6, 1987.

[62] G. Ribárik, T. Ungár, and J. Gubicza. *MWP-fit*: a program for multiple whole-profile fitting of diffraction peak profiles by *ab initio* theoretical functions. *J. Appl. Crystallogr.*, 34(5):669–676, Oct 2001.

[63] T. Ungár, E. Schafler, and J. Gubicza. *Bulk nanostructured materials*, chapter Microstructure of bulk nanomaterials determined by X-ray line profile analysis, page 361. Wiley-VCH ;;John Wiley [distributor], Weinheim ;Chichester, 2009.

[64] T. Ungar and G. Tichy. The effect of dislocation contrast on x-ray line profiles in untextured polycrystals. *physica status solidi (a)*, 171(2):425–434, 1999.

[65] P. Cordier, T. Ungar, L. Zsoldos, and G. Tichy. Dislocation creep in MgSiO3 perovskite at conditions of the earth's uppermost lower mantle. *Nature*, 428(6985):837–840, April 2004.

[66] J. Martinez-Garcia, M. Leoni, and P. Scardi. A general approach for determining the diffraction contrast factor of straight-line dislocations. *Acta Crystallographica Section A*, 65(2):109–119, 2009.

[67] I. Groma. X-ray line broadening due to an inhomogeneous dislocation distribution. *Phys. Rev. B*, 57(13):7535–, April 1998.

[68] A. J. C. Wilson. On variance as a measure of line broadening in diffractometry general theory and small particle size. *Proceedings of the Physical Society*, 80(1):286–, 1962.

[69] M. Kerber, E. Schafler, and M. Zehetbauer. Processing and evaluation of x-ray line profiles measured from nanostructured material s produced by severe plastic deformation. *Rev. Adv. Mater. Sci*, 10:427–433, 2005.

[70] T. Ungar. The meaning of size obtained from broadened x-ray diffraction peaks. *Advanced Engineering Materials*, 5(5):323–329, 2003.

[71] M. Leoni and P. Scardi. Nanocrystalline domain size distributions from powder diffraction data. *J. Appl. Crystallogr.*, 37(4):629–634, 2004.

[72] F. Spieckermann, H. Wilhelm, E. Schafler, S. Ahzi, and M.J. Zehetbauer. Application of composite models to isotactic polypropylene for the determination of phase specific stress-strain curves. *Materials Science and Engineering: A*, 483-484:76–78, June 2008.

[73] Z. Bartczak and M. Kozanecki. Influence of molecular parameters on high-strain deformation of polyethylene in the plane-strain compression. part i. stress-strain behavior. *Polymer*, 46(19):8210–8221, September 2005.

[74] B. Crist and F. M. Mirabella. Crystal thickness distributions from melting homopolymers or random copolymers. *Journal of Polymer Science Part B: Polymer Physics*, 37(21):3131–3140, 1999.

[75] R. N. Haward. The application of a simplified model for the stress-strain curve of polymers. *Polymer*, 28:1485–1488, 1987.

[76] Q. Fu, Y. Men, and G. Strobl. Understanding of the tensile deformation in HDPE/LDPE blends based on their crystal structure and phase morphology. *Polymer*, 44(6):1927–1933, March 2003.

[77] E. P. Moore. *Polypropylene Handbook*. Hanser Publishers Munich Vienna New York, 1996.

[78] J. D. Hoffman and R. L. Miller. Kinetic of crystallization from the melt and chain folding in polyethylene fractions revisited: theory and experiment. *Polymer*, 38(13):3151–3212, 1997.

[79] E. J. Clark and J. D. Hoffman. Regime III crystallization in polypropylene. *Macromolecules*, 17:878–885, 1984.

[80] R. N. Haward. Strain hardening of high density polyethylene. *Journal of Polymer Science Part B: Polymer Physics*, 45(9):1090–1099, 2007.

[81] Y. Men, J. Rieger, and G. Strobl. Role of the entangled amorphous network in tensile deformation of semicrystalline polymers. *Phys. Rev. Lett.*, 91(9):095502–1–095502–4, August 2003.

[82] I. Sakurada, T. Ito, and K Nakamae. Elastic moduli of the crystal lattices of polymers. *Journal of Poylmer Science: Part C*, 15:75–91, 1966.

[83] Y. Men, J. Rieger, and K. Hong. Critical strains in tensile deformed polyamide 6 and 6/66 copolymer. *Journal of Polymer Science Part B: Polymer Physics*, 43(1):87–96, 2005.

[84] Y. Men and G. Strobl. Critical strains determining the yield behavior of syndiotactic polypropylene. *J. Macromol. Sci.-Physics*, B40:775, 2001.

[85] T. Ungár, J. Gubicza, G. Ribárik, and A. Borbély. Crystallite size distribution and dislocation structure determined by diffraction profile analysis: principles and practical application to cubic and hexagonal crystals. *J. Appl. Crystallogr.*, 34(3):298–310, Jun 2001.

[86] S. Bruckner, S. V. Meille, L. Malpezzi, A. Cesaro, L. Navarini, and R. Tombolini. The structure of poly(d-(-)-$\beta$-hydroxybutyrate). a refinement based on the rietveld method. *Macromolecules*, 21(4):967–972, July 1988.

[87] G. Ribárik, J. Gubicza, and T. Ungár. Correlation between strength and microstructure of ball-milled al-mg alloys determined by x-ray diffraction. *Materials Science and Engineering A*, 387-389:343–347, December 2004.

[88] M. B. Kerber, E. Schafler, A.K. Wieczorek, G. Ribarik, S. Bernstorff, T. Ungar, and M. J. Zehetbauer. Synchrotron x-ray line-profile analysis experiments for the in-situ microstructural characterisation of spd nanometals during tensile deformation. *Int. J. Mater. Res.*, 100:770, 2009.

[89] H. Wilhelm, F. Spieckermann, E. Schafler, M. Kerber, and M. Zehetbauer. *to be published*, 2009.

[90] D. R. Buchanan and Robert L. Miller. X-ray line broadening in isotactic polystyrene. *J. Appl. Phys.*, 37(11):4003–4012, October 1966.

[91] R. Hosemann, W. Wilke, and F. J. B. Calleja. Twist-Korngrenzen und andere parakristalline Gitterstörungen in Polyäthylen-Einkristallen. *Acta Crystallographica*, 21(1):118–123, Jul 1966.

[92] R. Hosemann, A. Lange, and M. P. Hentschel. Mechanische Spannungen in Mikroparakristallen. *Acta Crystallographica Section A*, 41(5):434–440, 1985.

[93] W. Hinds. *Aerosol technology : properties, behavior, and measurement of airborne particles.* Wiley, New York, 2nd ed. edition, 1999.

[94] G. K. Williamson and W. H. Hall. X-ray line broadening from filed aluminium and wolfram. *Acta Metallurgica*, 1(1):22–31, January 1953.

[95] K. Yamada, M. Hikosaka, A. Toda, S. Yamazaki, and K. Tagashira. Equilibrium melting temperature of isotactic polypropylene with high tacticity: 1. determination by differential scanning calorimetry. *Macromolecules*, 36(13):4790–4801, July 2003.

[96] K. Yamada, M. Hikosaka, A. Toda, S. Yamazaki, and K. Tagashira. Equilibrium melting temperature of isotactic polypropylene with high tacticity. 2. determination by optical microscopy. *Macromolecules*, 36(13):4802–4812, July 2003.

[97] R.A. Phillips and M.D. Wolkowicz. *Polypropylene Handbook*, chapter Structure and Morphology, pages 113–176. Hanser Publishers, Munich, 1996.

[98] N. Alberola, J. Y. Cavaille, and J. Perez. Mechanical spectrometry of alpha relaxations of high-density polyethylene. *Journal of Polymer Science Part B: Polymer Physics*, 28(4):569–586, 1990.

[99] J.W. Eaton. *GNU Octave Manual*. Network Theory Limited, 2002.

[100] M. Wojdyr. *Fityk*: a general-purpose peak fitting program. *Journal of Applied Crystallography*, 43(5 Part 1):1126–1128, Oct 2010.

[101] N. Stribeck. Deformation behaviour of nanocomposites studied by x-ray scattering: Instrumentation and methodology. In Jozsef Karger-Kocsis and Stoyko Fakirov, editors, *Nano- and micro-mechanics of polymer blends and composites*, page 269. Hanser, Munich;Cincinnati Ohio, 2009.

[102] Z. Bartczak, R. E. Cohen, and A. S. Argon. Evolution of the crystalline texture of high-density polyethylene during uniaxial compression. *Macromolecules*, 25:4692–4704, 1992.

[103] L. M. W. K. Gunaratne, R. A. Shanks, and G. Amarasinghe. Thermal history effects on crystallisation and melting of poly(3-hydroxybutyrate). *Thermochim. Acta*, 423(1-2):127–135, December 2004.

[104] E. Lezak, Z. Bartczak, and A. Galeski. Plastic deformation of the $\gamma$ phase in isotactic polypropylene in plane-strain compression. *Macromolecules*, 39(14):4811–4819, July 2006.

[105] E. Lezak and Z. Bartczak. Plastic deformation of the $\gamma$ phase isotactic polypropylene in plane-strain compression at elevated temperatures. *Macromolecules*, xx:xxxx, 2007.

[106] P. Klimanek and R. Kuzel Jnr. X-ray diffraction line broadening due to dislocations in non-cubic materials. i. general considerations and the case of elastic isotropy applied to hexagonal crystals. *Journal of Applied Crystallography*, 21(1):59–66, 1988.

[107] A. Borbely, J. Dragomir-Cernatescu, G. Ribarik, and T. Ungar. Computer program anizc for the calculation of diffraction contrast factors of dislocations in elastically anisotropic cubic, hexagonal and trigonal crystals. *Journal of Applied Crystallography*, 36(1):160–162, 2003.

[108] A. N. Stroh. Dislocations and cracks in anisotropic elasticity. *Philosophical Magazine*, 3(30):625–646, 1958.

[109] J. R. Hirsch and P. T. Wang. Texture and strength evolution in deformed polypropylene. *Texture, Stress, and Microstructure*, 13(2-3):101–122, 1991.

[110] S. Ahzi, B. J. Lee, and R. J. Asaro. Plasticity and anisotropy evolution in crystalline polymers. *Materials Science and Engineering A*, 189(1-2):35–44, December 1994.

[111] J. Jia and D. Raabe. Evolution of crystallinity and of crystallographic orientation in isotactic polypropylene during rolling and heat treatment. *European Polymer Journal*, 42(8):1755–1766, August 2006.

[112] K. Tashiro, M. Kobayashi, and H. Tadokoro. Vibrational spectra of theoretical three-dimensional elastic constants of isotactic polypropylene crystal: An important role of anharmonic vibrations. *Polymer Journal*, 24(9):899–916, 1992.

[113] C. Sawatari and M. Matsuo. Elastic modulus of isotactic polypropylene in the crystal chain direction an mesured by x-ray diffraction. *Macromolecules*, 19:2653–2656, 1986.

[114] A. Galeski, Z. Bartczak, A. S. Argon, and R. E. Cohen. Morphological alterations during texture-producing plastic plane strain compression of high-density polyethylene. *Macromolecules*, 25(21):5705–5718, October 1992.

[115] H.P. Karnthaler. private communication, Nov. 2009.

[116] M. Aboulfaraj, C. G'Sell, B. Ulrich, and A. Dahoun. In situ observation of the plastic deformation of polypropylene spherulites under uniaxial tension and simple shear in the scanning electron microscope. *Polymer*, 36(4):731–742, 1995.